ABSTRACT

The Impact of Conventional and Wide Bandgap Semiconductor PWM Inverter EDM Bearing Currents on Motor Bearings

Ryan Collin, Ph.D.

Advisor: Annette von Jouanne, Ph.D.

The pulse width modulated (PWM) ac motor drive has revolutionized the industrial sector by drastically reducing energy consumption and improving the efficiency of industrial processes. To continue the transition towards an electrified society, power density in electric motor drives must continue to increase. To this end, motor drives of the future will contain wide bandgap (WBG) semiconductor devices such as silicon carbide (SiC) and gallium nitride (GaN). The introduction of these WBG devices into motor drives comes with exacerbated application issues due to faster dv/dt device turn on/off times and relatively higher switching frequencies for the same device cooling requirements as conventional silicon (Si) devices. A key issue produced by these PWM motor drives is premature bearing failure due to an increase in vibration from the damage caused by electric discharge machining (EDM) bearing currents. This dissertation presents detailed discharge circuit modeling of motor bearing currents, investigates the impact of discharge energy on the damage produced on the bearing race and ball surfaces through the use of a finite element (FE) model, presents a novel

technique to statistically characterize EDM amplitudes over various motor operating conditions, and uses this statistical approach along with experimental evidence to predict a bearing's lifetime. The work presented here is a key contribution to developing intricate predictive maintenance models for motor bearings, which are of great value to industrial operators because of the enormous costs associated with motor down time.

The Impact of Conventional and Wide Bandgap Semiconductor PWM Inverter EDM Bearing Currents on Motor Bearings

by

Ryan Collin, B.S., M.S.

A Dissertation

Approved by the Department of Electrical and Computer Engineering

_____

Kwang Y. Lee, Ph.D., Chairperson

Submitted to the Graduate Faculty of
Baylor University in Partial Fulfillment of the
Requirements for the Degree
of

Doctor of Philosophy

Approved by the Dissertation Committee

_____

Annette von Jouanne, Ph.D., Chairperson

_____

Alex Yokochi, Ph.D.

_____

Emmanuel Agamloh, Ph.D.

_____

Mack Grady, Ph.D.

Accepted by the Graduate School

May 2022

_____

J. Larry Lyon, Ph.D., Dean

Page bearing signatures is kept on file in the Graduate School.

TABLE OF CONTENTS

LIST OF FIGURES

LIST OF TABLES

ACKNOWLEDGMENTS

I would like to thank my Ph.D. advisor Dr. Annette von Jouanne for her valuable input, mentorship, and guidance throughout my time as a graduate student and for the opportunity to pursue the Ph.D. degree and conduct research in her lab. I will always be thankful for the tremendous impact you have had on me and my family's life during my time at Baylor University; it has been a gift that will impact me for the rest of my life.

A special thanks as well to Dr. Alex Yokochi, who has played an integral role in this research project, and whose ideas have been instrumental in the development of this dissertation. I have very much enjoyed our many conversations on technical topics and ideas.

To Dr. Emmanuel Agamloh and Dr. Mack Grady, I would like to express my appreciation for your service on my dissertation committee and for the roles you have played in my intellectual formation during my engineering education.

To my friends in the Baylor Energy and Renewable Systems Lab, thank you for your friendship, collaboration, and support. I would especially like to acknowledge Caleb Li for the assistance he provided in the development of the hardware testbeds, and to Ben Phillips for the time and effort he put into the FE model. Credit must also be given to Dr. Bernd Zechmann from Baylor University's Center for Microscopy and Imaging for the imaging assistance he provided. Additionally, a special thanks to Mr. Ashley Orr for his assistance in modifying motors for bearing current measurement.

Finally, I express my utmost gratitude to my beloved wife, who has gladly denied her own will and sacrificed far more than many realize for me to complete this degree. Your dedication and devotion to our marriage above all else has merited many graces for me, and to share in this sacrament with you makes me a better man, and a happy one.

DEDICATION

To my mother, who has instilled within me a love for academic education.

To my father, who taught me how to work and has given me a love for electrical engineering.

To my brother, a best friend who has challenged and pushed me in all areas of my life and given me a love for intellectual inquiry.

And to my wife, who never ceases to give of herself, and whose virtuous and upstanding life is largely responsible for my own increases in holiness and sanctity.

"Ora et Labora"

CHAPTER ONE

Introduction

Background

The electric machine is one of the fundamental energy conversion tools available to human civilization, with modern machines allowing for highly efficient electrical to mechanical energy conversion, and vice versa. To power and control these machines, power electronic motor drives are employed in many applications such as electric vehicles, pumps, fans, HVAC, conveyor belts, propulsion, and household appliances, to name just a few. For AC machines, the variable frequency drive (VFD) is the fundamental power electronic motor drive unit, with the two-level six-switch (TLSS) PWM inverter being the most common topology for low voltage three-phase systems, as it effectively controls machines while minimizing the number of electronic components. The TLSS inverter generates high frequency voltage pulses that result in the required sinusoidal phase currents, due to the motor impedance being dominated by the winding inductance. In an ideal balanced three-phase motor drive system, the phase voltages and currents sum to zero. Due to the high frequency PWM voltage pulses in the TLSS inverter and the allowable switching states, the phase voltages do not sum to zero, and thus a net voltage potential is present between the motor neutral point and the system ground, which is known as the common-mode (CM) voltage. The TLSS inverter with low-frequency machine equivalent circuit components connected is shown in Fig. 1.1, where the motor neutral point to ground voltage V_n is the CM voltage. There are 8

possible switching states that can be employed by the TLSS inverter, which produces a net voltage vector that rotates in space, allowing the machine to spin, as can be seen in Fig. 1.2.

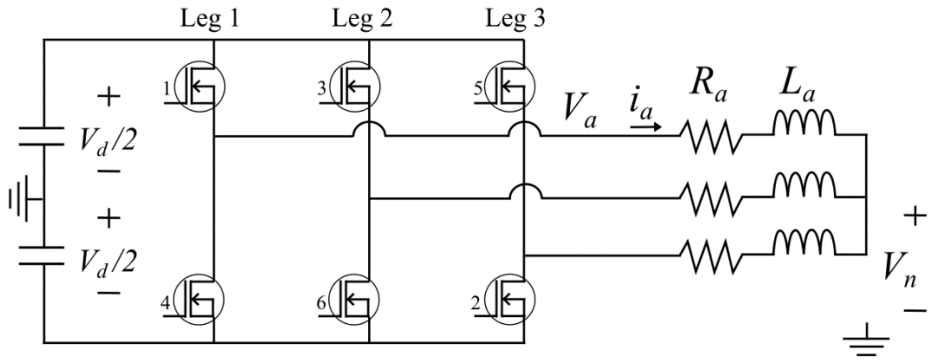

Figure 1.1. A two-level six switch three phase PWM inverter. The common mode voltage is the voltage measured between the motor neutral point and the system ground.

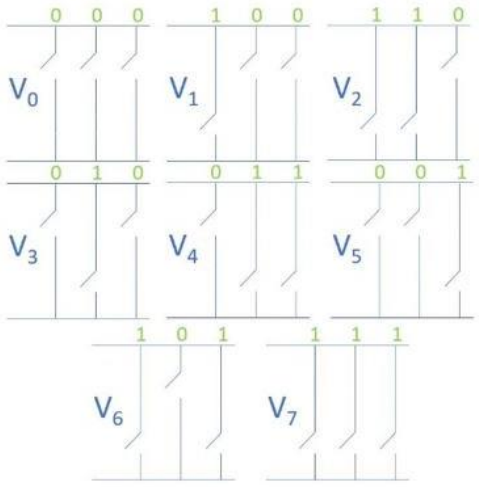

Figure 1.2. The TLSS inverter has $2^3 = 8$ allowable switching states that produce the necessary sinusoidal phase current to drive the machine.

Performing Kirchhoff's voltage law for each phase of Fig. 1.1 produces the following system of equations:

$$V_a = V_{an} + V_n \tag{1.1}$$

$$V_b = V_{bn} + V_n \tag{1.2}$$

$$V_c = V_{cn} + V_n \tag{1.3}$$

where the phase voltages in terms of the phase resistance and inductance are:

$$V_{an} = R_a i_a + L_a \frac{di_a}{dt} \tag{1.4}$$

$$V_{bn} = R_b i_b + L_b \frac{di_b}{dt} \tag{1.5}$$

$$V_{cn} = R_c i_c + L_c \frac{di_c}{dt} \tag{1.6}$$

Assuming each phase resistance and inductance to be equal and summing together the motor to ground terminal voltages V_a, V_b, and V_c yields:

$$V_a + V_b + V_c = V_{an} + V_{bn} + V_{cn} + 3V_n$$

$$= R(i_a + i_b + i_c) + L\left(\frac{di_a}{dt} + \frac{di_b}{dt} + \frac{di_c}{dt}\right) + 3V_n \tag{1.7}$$

Since the neutral point of the machine is inaccessible (i.e., no electrical connection other than the three phase windings), the summation of the three phase currents is zero. For a TLSS inverter, the PWM switching frequency is generally much larger than the motor fundamental frequency (i.e., current ripple is assumed negligible), therefore the derivative components of Eq. 1.7. are assumed to be zero, and the equation can be simplified.

$$V_n = V_{CM} = \frac{V_a + V_b + V_c}{3} \tag{1.6}$$

Therefore, the CM voltage is equal to the summation of the motor terminal voltages divided by 3. For a sinusoidal voltage line driven machine, balanced operation permits the phase voltages to sum to zero. On the other hand, the TLSS inverter motor terminal voltages are connected to either $+V_d/2$ or $-V_d/2$. As has been demonstrated, this results in a nonzero CMV, which has high frequency components that can be seen in Fig. 1.3.

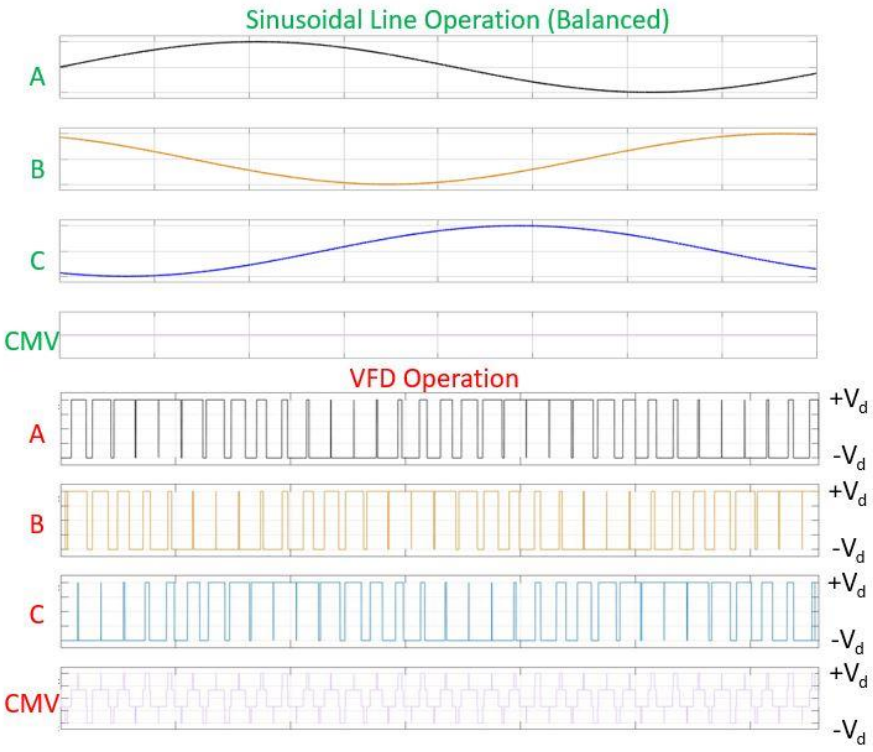

Figure 1.3. The phase voltages of a sinusoidal line driven machine sum to zero, resulting in zero common mode voltage, while the high frequency PWM phase voltages generate a CMV within the electric machine.

Although these TLSS power electronic variable frequency drives (VFD) allow for speed control and exceptional torque response, the high frequency nature of the phase voltages and CM voltage create adverse effects on the motor drive system. The high frequency components of the CM voltage excite a CM current through the parasitic capacitances that are present in the system. This CM phenomenon along with the sharp *dv/dt* of inverter output voltages leads to increased electromagnetic interference (EMI), bearing failure from electric discharge machining (EDM) bearing currents, and motor insulation failure due to overvoltage at the machine terminals, which is a result of high frequency PWM transmission line reflection. Of particular interest in this dissertation is the EDM

phenomenon due to bearing currents and the subsequent premature failure that occurs due to increased vibration.

Literature Review

The primary cause of motor failure is due to failure of the bearings, which accounts for 40-50% of all motor failures [1-3]. The cost associated with motor down time can be extremely high [4].

Conventional Bearing Currents

Conventional bearing currents, as discovered by Alger and Samson in 1924 [5], are due to an asymmetric distribution of flux throughout the stator, which is inherent in practical motors. This flux asymmetry results in currents being electromagnetically induced into the shaft of the machine, leading to low energy currents through the machine bearings. Conventional bearing currents are more typical in large machines and have large magnitudes (negligible at 2 hp, up to 30 A pk-to-pk at 600 hp [6]), although flow through the bearings at low voltages (typically < ~1V [7]), and therefore do not cause significant damage. With advanced manufacturing of electric machines in modern times, this mode of bearing current has become less significant, especially in smaller machines. These conventional bearing currents are most often observed during non-PWM sinusoidal line voltage operation, especially during the transients of motor acceleration and deceleration [8].

Bearing Currents due to Common-Mode Emissions

With the advancement of semiconductor devices and the introduction of PWM motor drives like the TLSS inverter, a new mode of bearing currents became evident:

bearing currents due to the presence of CM voltage and current. The high frequency nature of the PWM voltages sent to the machine terminals make otherwise irrelevant parasitic capacitive paths relevant. A schematic diagram of the high frequency parasitic capacitive paths within a machine is shown in Fig. 1.4. The parasitic capacitances include the stator winding to frame capacitance C_{sf}, stator to rotor capacitance C_{sr}, rotor to frame capacitance C_{rf}, and the bearing capacitances C_{b1} and C_{b2}. These parasitic capacitances are distributed throughout the machine but can be lumped together into equivalent circuit model components for modeling and simulation. The bearing capacitances C_{b1} and C_{b2} are often lumped into a single inner to outer bearing race capacitance, although separate capacitances do exist between the inner race and bearing balls and the bearing balls and outer race. The outer race of each bearing is grounded to the frame of the machine. When a high frequency CM voltage is applied to the windings of the machine, these parasitics provide a path for the high frequency CM current to return to the source along the motor-inverter ground line, whose frequency components can be in the 100's of kHz to several MHz range [9].

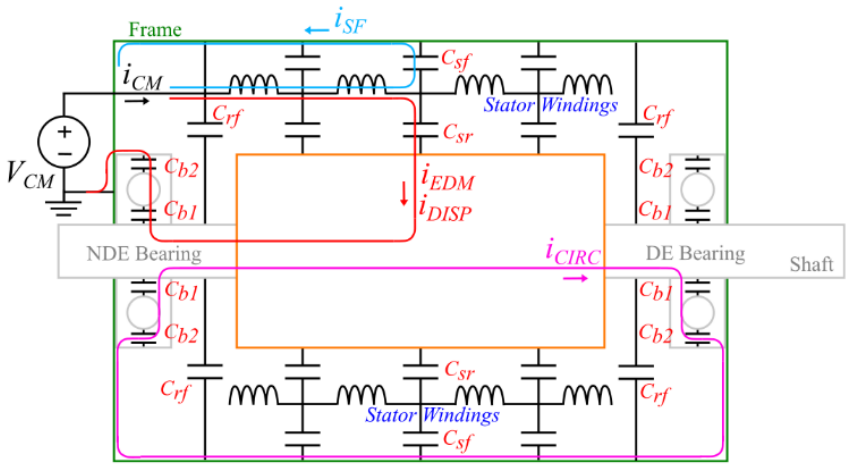

Figure 1.4. Distributed high frequency parasitic capacitive current paths in an electric machine.

From Fig. 1.4, a capacitive voltage divider is produced on the rotor and shaft assembly of the machine. The shaft voltage is a fraction of the CM voltage, according to the bearing voltage ratio (BVR) [6, 10, 11]:

$$\text{BVR} = \frac{V_{Shaft}}{V_{CM}} = \frac{C_{sr}}{C_{sr}+C_{rf}+2C_b} \tag{1.7}$$

Clearly, the magnitude of the shaft voltage electrostatic accumulation depends on the parasitic capacitive coupling paths. Motor parasitic capacitances are calculated in [10] using machine parameters.

The CM current produced by PWM inverters has three components that interact with the machine bearings: displacement current, stator-to-frame current, and EDM bearing currents. Various papers in the literature have detailed these high frequency current paths using finite element modeling, simulation, and experimental measurements [6, 7, 12-15]. A flow diagram demonstrating the origin of bearing currents is provided in Fig. 1.5.

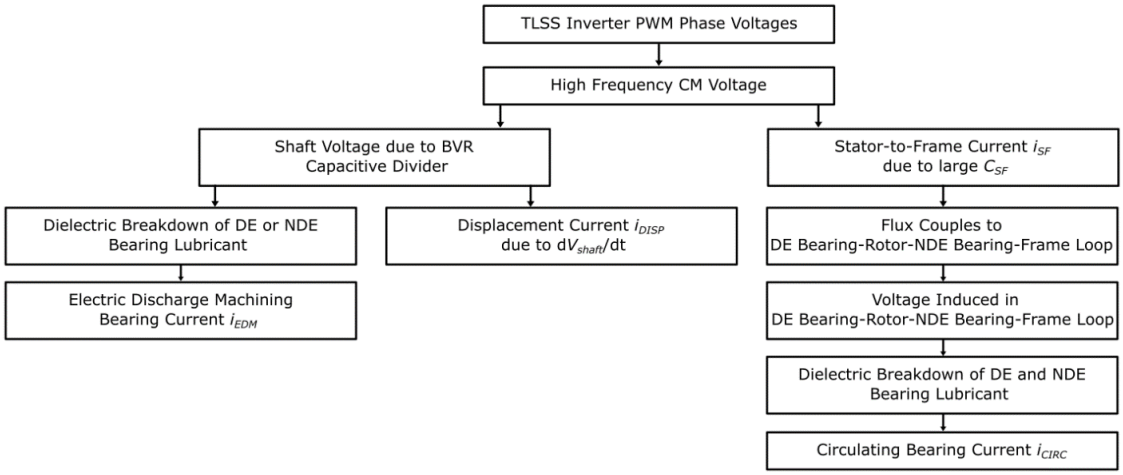

Figure 1.5. Flow diagram of bearing current process in machines driven by TLSS inverters.

Displacement current. The bearing displacement current i_{DISP} (see Fig. 1.4) is due to the time rate of change of the shaft voltage, which acts across the inner and outer race of both the drive end (DE) and non-drive end (NDE) bearings. This mode of bearing current is small in amplitude, and researchers agree that bearing displacement current has negligible effects on bearing operation and lifetime [6, 15].

Stator-to-frame current. The stator-to-frame current i_{SF} (see Fig. 1.4) is the largest component of the CM current, due to the large capacitive coupling C_{SF} between the stator windings and stator core, where the core is electrically connected to the frame of the machine, which is at system ground potential. The flux generated from this mode of CM current magnetically couples to the loop that comprises the rotor, DE bearing, frame, and NDE bearing. When the high frequency induced voltage exceeds the dielectric strength of the bearing lubricant, a circulating bearing current i_{CIRC} is produced on this path, as shown in Fig. 1.4 [14, 16]. Today it is common to isolate one of the machine's bearings to prevent circulating bearing currents, for example by using a ceramic bearing [17]. At the time of writing, a survey of the 5 hp bearing market concluded that ceramic bearings are typically 2-4x more expensive than standard steel bearings, depending on the requirement of the application. Electric motors above 25 hp are more susceptible to high frequency circulating bearing currents [18].

Electric discharge machining bearing current. During a rising or falling edge of the CM voltage, a voltage is produced on the shaft of the machine via electrostatic coupling, according to Eq. (1.7), which is a fraction of the CM voltage. As the machine spins, the bearing lubricant forms a thin film on which bearing rolling elements ride,

achieving hydrodynamic lubrication. An electric field is formed across the thin bearing lubricant film due to the shaft voltage, producing a charged bearing capacitance C_b. When the shaft voltage produces an electric field that exceeds the dielectric strength of the lubricant film, the dielectric breaks down forming an electric discharge machining (EDM) bearing current i_{EDM} (see Fig. 1.4), where all the electrostatic energy stored in the rotor assembly capacitances is dissipated into the discharge channel. Since the ratio of energy dissipated to bearing ball/race discharge surface area is large, the local temperature increases significantly, and local melting may occur on the bearing ball and race surfaces. Damage on the race and ball surface of the bearing appears microscopically as micropits and pillars and macroscopically as frosting and fluting [19], as shown in Figs. 1.6 and 1.7.

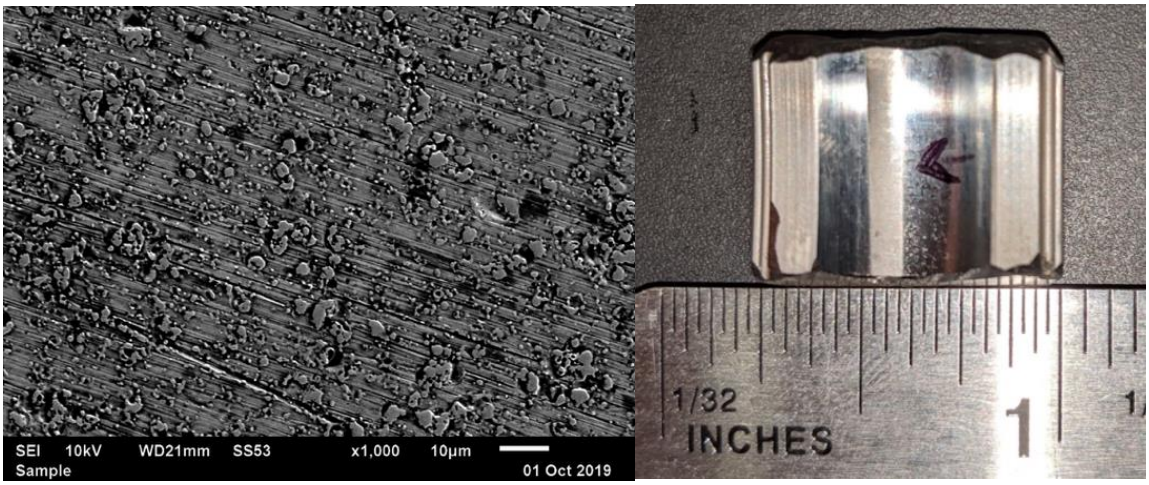

(a) (b)

Figure 1.6. (a) EDM currents produce micro- pits and pillars on the race surface (b) that appears as frosting on a macroscopic level.

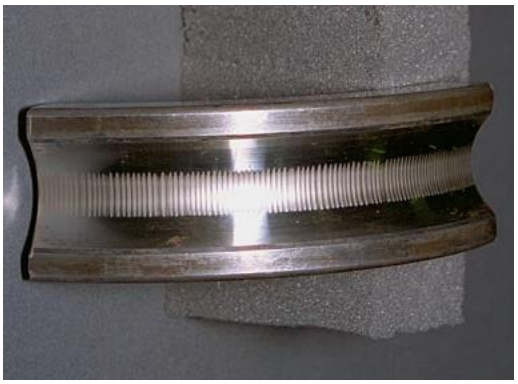

Figure 1.7 Fluting on the inner race of a bearing [19].

For 6209 C3 bearings, EDM discharge micropitting diameters have been reported between 0.5-1 μm [20], but will depend on the specific motor design because the size of the pits and pillars is proportional to the energy buildup on the shaft, which in turn depends on Eq. (1.7). Oliver et. al have reported micropitting diameters in the range of 5-8 μm [17]. Electric motors less than 25 hp in size are especially susceptible to bearing damage from EDM bearing currents [18]. In the past researchers have proposed a bearing current density specification as a benchmark for evaluating if a specific bearing discharge will cause EDM damage to the ball and race surface, a measurement which is independent of bearing size [6]:

$$J_b = \frac{i_b}{A_H} \tag{1.8}$$

Here, J_b is the apparent bearing current density, i_b is the apparent peak bearing current, and A_H is the Hertzian contact area between the race and ball surface. The current density J_b is named "apparent" for two reasons: the peak bearing current i_b is impossible to measure without causing some interference to the measurement and the Hertzian contact area A_H calculated is an estimation of the area of the EDM discharge. This explains the discrepancy in the literature for the differing bearing current density threshold levels that

cause EDM damage [6, 11, 20-22]. For this reason, researchers have moved away from characterizing EDM discharges in this manner in recent times.

Fluting of the race surfaces is the other mode of damage that can be observed on bearing race surfaces from EDM discharges. These flutes are larger damage areas that occur on the race surfaces that are similar in appearance to washboarding on a gravel road, as can be seen in Fig. 1.7. It is a secondary effect of damage on the race surfaces that develops with time, as frosting and micropitting is the first indication of EDM damage. Researchers are still unsure of the exact mechanism that causes fluting on the race surface [20], although it has been proposed that as the rolling elements pass over the micropits on the race mechanical resonance vibrations occur, which over time slowly forge the fluting pattern into the race material [17]. Despite this hypothesis, various aspects of race fluting remain unclear: where they will appear on the race surface, how many will appear, what size they will be, and how long they take to form after frosting has occurred.

In addition to micropitting and fluting on the bearing ball and race surfaces, lubricant degradation occurs. During each discharge a microarc conducts through the bearing lubricant, burning the lubricant and accelerating its degradation [17]. Over time, the lubricant begins to work improperly, and once it has failed, it no longer provides a film for the rolling elements to ride on. Lubrication degradation may be another key factor for the development of flutes on the race surface because the interaction of the rolling elements with the race surfaces will increase with a degraded, ineffective lubricant. Indeed, it is well known that improper lubrication is one of the primary causes

of bearing failure. The degraded lubricant is black due to burning from microarc discharges, as shown in Fig. 1.8.

Figure 1.8. EDM discharges burn and degrade the bearing lubricant (right) as can be seen here compared to a bearing with new lubricant (left).

Experimental Measurement Technique

To further understand the discrepancy in the literature for an acceptable bearing current density, an understanding of the experimental bearing current measurement is required. To obtain an experimental measurement, researchers isolate both the drive end (DE) and non-drive end (NDE) bearing outer races from the frame of the machine by inserting a thin insulating sleeve into the bearing seat. Then a jumper wire is attached to the outer races and connected to the frame of the machine, which makes a current measurement possible by forcing the bearing current to flow through the wire [6, 20, 23-26]. Although a measurement is now available, it is only an "apparent measurement" because the insulating sleeve introduces an isolation capacitance and the measurement wire introduces a parasitic inductance L_w. This modification of the motor system is non-negligible at bearing current discharge frequencies. The equivalent circuit model of EDM

bearing current paths is shown in Fig. 1.9, where a parallel RC circuit with a switch models the discharge at the time of the discharge event [27].

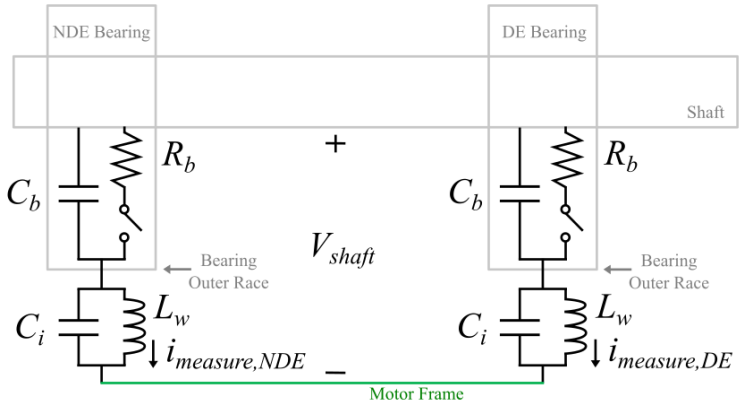

Figure 1.9. Circuit model of EDM bearing current paths in electric machine with the effects of motor modification for bearing current measurement included.

Here C_i is the isolation capacitance due to the bearing insulating sleeve, L_w is the measurement jumper wire inductance, C_b is the capacitance of the bearing, and R_b is the bearing discharge resistance. From the circuit model of Fig. 1.9, the measured bearing current is not the same as the actual current discharging within the bearing, thus the name "apparent bearing current". Although the measurement is not direct, it has been shown that the apparent bearing current measurement is proportional to the actual bearing current [6]. Precise values for the isolation capacitance and the measurement wire inductance may be obtained to find the proportion between the two. It is the variance in proportion between the apparent and actual bearing current that leads to the discrepancy of what magnitude of bearing current density causes EDM damage to bearings.

Variables That Influence Bearing Currents

This section highlights the key variables that effect EDM bearing currents, both the intensity of the discharge and the frequency of their occurrence.

Lubricant thickness. The dielectric strength of the bearing lubricating grease determines the voltage level at which the discharge will occur and in turn the energy of the discharge and magnitude of the discharge current, where the thickness of the grease lubricating film determines the dielectric strength. There are two main parameters that influence the lubricant film thickness: bearing temperature and shaft speed [25, 28, 29]. As the bearing temperature increases, the lubricant film thins and the dielectric strength weakens causing the discharge to occur at lower voltages, which in turn creates relatively smaller magnitudes of bearing currents. As the shaft speed increases, the lubricant thickness increases due to hydrodynamic lubrication being achieved [28] and the dielectric strength increases, leading to larger shaft voltages and bearing current discharges.

Bearing voltage ratio. The BVR is the key determining factor for the amplitude of bearing currents for a given machine, due to the parasitic capacitances producing a voltage divider on the shaft. Researchers have shown that it is possible to alter and reduce the BVR by use of electrostatic shields on the stator windings [30, 31].

PWM switching frequency. Due to the dv/dt of the PWM phase voltages being the main cause of shaft electrostatic coupling and EDM bearing currents, an increase in the occurrence of PWM dv/dt events will lead to more EDM bearing current discharge

events. Therefore, the occurrence of bearing current discharges is linearly proportional to the PWM switching frequency of the inverter [13, 20, 32].

Device rise time. PWM voltage rise times also have a significant effect on the threshold level for shaft voltage breakdown. Dielectric breakdown theory for pulsed voltages shows that the dielectric strength of a medium is inversely proportional to the time duration of the applied pulse [7, 33-38]. Faster rise times produce an "ionization shock" on the dielectric, which allows the voltage to build up to a larger value before breakdown than it otherwise would if the rise time were slower. Therefore, semiconductor devices with faster rise times should give rise to larger shaft voltage amplitudes before breakdown. Additionally, it has been demonstrated that wide bandgap devices produce larger common mode emissions [39] (i.e., larger common mode currents), which can lead to larger magnitude shaft voltages and bearing currents.

Bearing Degradation Due to EDM Bearing Currents

The EDM phenomenon within bearings leads to increased vibration and premature failure. Several techniques can be used to detect a bearing failure such as machine vibration monitoring [40-42], shock pulse measurement [43, 44], acoustic emissions [45, 46], stator current monitoring [47-50], and monitoring the stray stator flux [51]. However, many of these techniques are only effective when the bearing has reached extreme degradation or has a large defect, such as in [51] where the authors artificially punched a hole in the outer race to validate their condition monitoring technique. Although the field of bearing condition monitoring is well studied, there is little work on tying EDM currents to vibration degradation patterns in bearings. Of the work that does

exist [29, 52-54], researchers often apply a pulse source to the bearing, which is sometimes coupled with a capacitor to increase the energy dissipated in the discharge. Although vibration does accumulate in this work, only preliminary experiments have been performed, and there have been no definitive predictions for when a bearing will fail because there is no characterization method to understand shaft voltages and bearing currents for specific operating conditions. As bearing damage accumulates, the vibration increases at an exponential rate, as can be seen by the SKF diagnostics plot of Fig. 1.10.

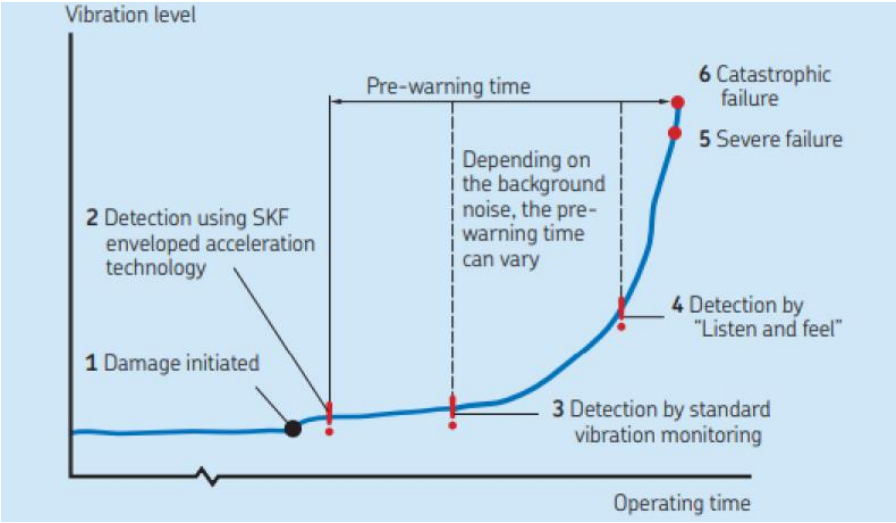

Figure 1.10. Bearing vibration increases exponentially over time [55].

Vibration builds within the bearing due to a summation of local damage due to EDM discharges. This leads to the micropits, pillars and frosting of Fig. 1.6, or the fluting and washboard appearance of Fig. 1.7.

Conclusions from Literature Review and Motivation for Research Program

Although much research has accrued in the EDM bearing current literature in the past twenty years, there is still much to understand about the phenomenon, and many

questions to be answered. It is evident from the various differing publications that the bearing current density is not a precise means to determine harmful bearing currents due to variations in the isolation capacitance and measurement wire inductance for each experimental setup across labs, which produces differing claims. As a result, experimental results that require motor modification for measurement only produce results that are proportional to the actual value, which is not as helpful for determining how a specific discharge energy produces damage within a bearing, since this will also vary between labs. Therefore, what is most important for connecting an EDM event to bearing damage is the energy of the discharge and the time it takes for that energy to dissipate within the bearing (power), which to this point has been a challenge for researchers to acquire. This dissertation will precisely model bearing EDM events, which will reveal the precise energy of discharges that are dissipated within a bearing and a thorough investigation of the effect of the measurement wire inductance will be conducted. The root cause of the discrepancy between acceptable bearing current density threshold levels in the literature will be revealed.

There appears to be a slight gap between two theories that have been presented in the literature, namely the BVR theory and the pulsed dielectric theory, which is based on the device slew rate. The BVR theory holds that the machine parasitic capacitances are intrinsic to the machine dimensions, and do not change, although the bearing capacitances do slightly change with temperature [52, 56, 57]. Given this, one would expect the same shaft voltage across motor operating points because it is set by the BVR. However, as will be seen in this work, this is only valid for when the lubricant remains intact at low motor operational temperatures. On the other hand, the device rise time

theory holds that the voltage across a pulsed dielectric can build up to a larger value before breakdown with a decrease in device rise time (increase in slew rate). Since the CM voltage amplitude is fixed, this would imply that the BVR would increase for devices with faster turn on/off times, such as WBG devices (although this shouldn't happen according to BVR theory, which maintains that the BVR is fixed). At the very least, given that each theory is valid, the two need to be synthesized with one another for further understanding. To do this, a TLSS inverter with SiC WBG devices is employed in this work to investigate the differences in shaft voltage and EDM bearing current amplitudes between Si and SiC devices across various motor operational points.

To the author's knowledge there has yet to be any research presented on tying the characterization of motor drive bearing currents with the damage accumulated over time to enable lifespan predictions. To predict a bearing's lifetime, several factors would need to be known: First, knowing how a particular discharge energy damages the bearing ball and races and contributes to vibration accumulation would be of utmost importance. Second, the frequency of discharge events. As mentioned previously, the EDM rate is linearly proportional to the inverter switching frequency [13, 20, 32]. The final piece to understand is the amplitude of the potential discharge energies that occur for a given motor operational point. With this information, predictions about bearing lifetime can be made based off various motor conditions. To investigate how various discharge energy amplitudes play a role in damaging the ball and race, a finite element (FE) model is developed, the results of which are validated experimentally. The effect of the motor modification for experimental bearing current measurement will also be considered in the FE model. To understand the possible discharge energies that can occur, a novel

approach is taken to characterize shaft voltages and EDM bearing currents using probability density functions. Various tests are performed to understand how the density functions are affected by motor operating conditions such as lubricant thickness, temperature, and load. All this work will contribute to the development of lifetime prediction models for bearings that are damaged by EDM bearing currents. Finally, experimental vibration degradation evidence will be used to develop a bearing SOH metric that can be used to predict the lifetime of a bearing given particular motor operating conditions.

This dissertation is organized as follows: Chapter Two discusses the equipment, experiments, and testbeds designed to conduct the research, where the engineering design will be highlighted. Chapter Three explores the discharge transients and parasitics that contribute to the EDM phenomenon through detailed circuit modeling. Discharges are modeled for normally operating motors and for motors that have been modified for EDM bearing current measurement. A discussion is then conducted comparing the two. Chapter Four then investigates the impact that these discharges have on the bearing ball and race surfaces. To do this, an FE model is developed and is used to investigate the threshold energy that produces damage on the ball and race surfaces. The model is validated with experimental evidence. Chapter Five presents a novel technique for characterizing EDM shaft voltages and bearing currents for both conventional and WBG semiconductor-based motor drives which are driving an IM. Differences between the two types of motor drives are made, and the BVR and pulsed dielectric theories are synthesized and nuanced. Chapter Six uses experimental evidence to correlate specific discharge energies with bearing lifetime in an accelerated manner. Correlations are then drawn to the lower

energy discharges that are found on the motor drive of Chapter Five to predict the lifetime of a bearing driven by conventional and WBG device motor drives. Conclusions are then provided in Chapter Seven.

CHAPTER TWO

Testbed Development and Experimental Design

The research plan was implemented through the development of two experimental testbeds, which were used to study bearing degradation and the EDM phenomenon. The first testbed, the machine testbed, consisted of electric machines and power electronic VFD inverters. This testbed was used to study, characterize, and compare shaft voltages and EDM bearing currents for various operational conditions including load, temperature, and speed. The second testbed, the bearing testbed, was used to study EDM discharge characteristics and the degradation of bearings. This chapter highlights the design of the two testbeds.

Machine Testbed

The machine testbed is shown in Fig. 2.1. The testbed is comprised of two 460 V motor drive systems, one Si-based and the other SiC-based. An additional machine and regenerative VFD are used to apply mechanical load to the machine under test, while a separate machine is also used for no load testing. Shaft voltage, EDM bearing current, and bearing temperature data are acquired through an oscilloscope connected to a data acquisition PC. This section will describe the design and features of the machine testbed.

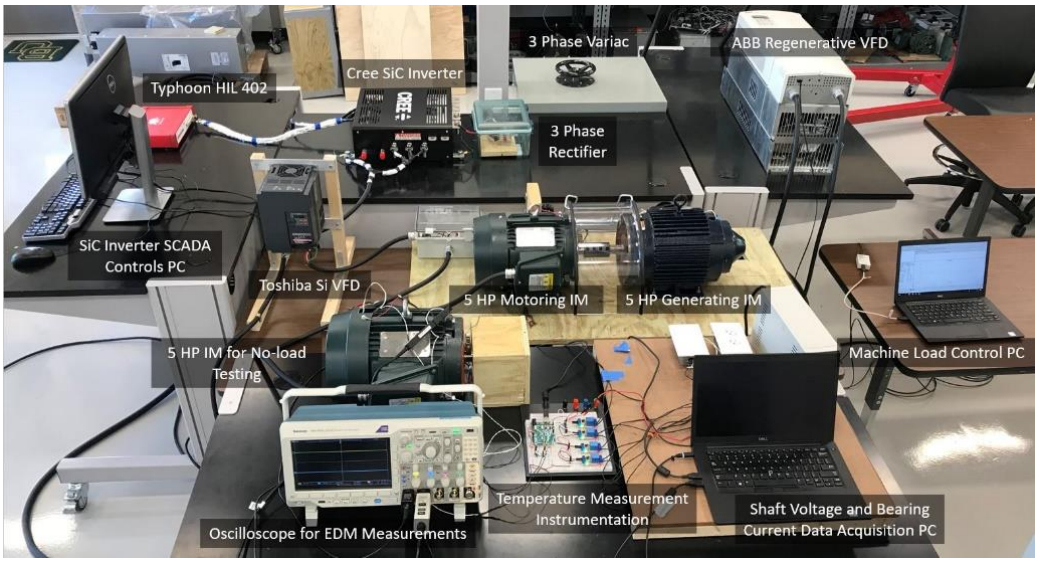

Figure 2.1. Machine testbed used for the characterization of CM voltages, shaft voltages, and EDM bearing currents due to Si and SiC PWM inverters.

Inverters

To drive the machines in the testbed, two TLSS power electronic inverters were employed: a Si-based and commercially available Toshiba VF-S15 VFD and a non-commercially available SiC-based Cree CRD200DA09E high performance three phase inverter evaluation unit.

Toshiba VF-S15. The Toshiba VF-S15-4075PL-W VFD is a Si-based TLSS power electronic inverter for motor drive applications up to 10 hp (7.5 kW). The unit contains six Si IGBTs that comprise the TLSS inverter. The Toshiba VF-S15 VFD is shown in Fig. 2.2, along with an experimental oscilloscope measurement of the on/off switching time for one of the IGBT devices, which were measured according to IEEE STD-181-2011 [58]. The Si IGBT devices have a turn on/off time of 190 ns, which is a slew rate of 2,821 V/μs.

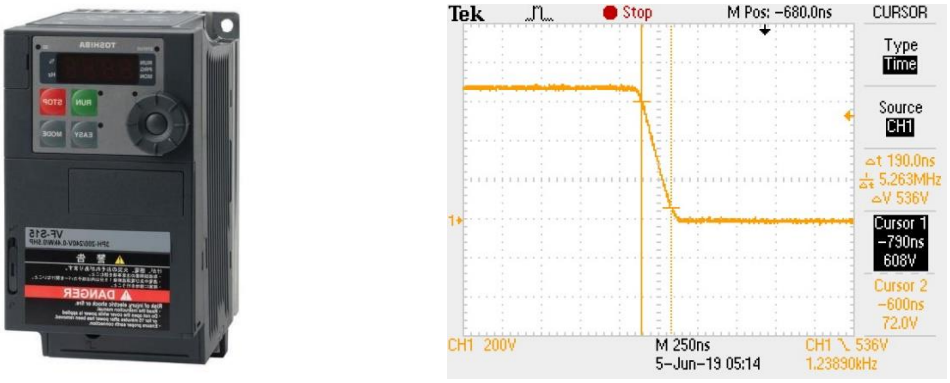

(a) (b)

Figure 2.2. (a) Toshiba VF-S15 VFD's (b) IGBT devices have turn on/off times of 190 ns.

Cree CRD200DA09E three-phase evaluation unit. The CRD200DA09E SiC three-phase evaluation unit [59] is a 250 kW TLSS inverter. The unit contains three Cree HT-3291-R-VB [60] high performance SiC half-bridge modules. The modules have a 900 V drain-source breakdown voltage, a 2.5 mΩ drain-source on resistance, and a maximum junction temperature of 175 °C. The evaluation unit is capable of an AC output phase current (RMS) of 300 A. The unit employs liquid cooling when operating at rated load. The evaluation unit can be seen in Fig. 2.3, along with an experimental oscilloscope measurement of the on/off switching time for one of the SiC MOSFET devices. The SiC MOSFETs have a turn on/off time of 48 ns, which corresponds to a slew rate of 11,500 V/μs.

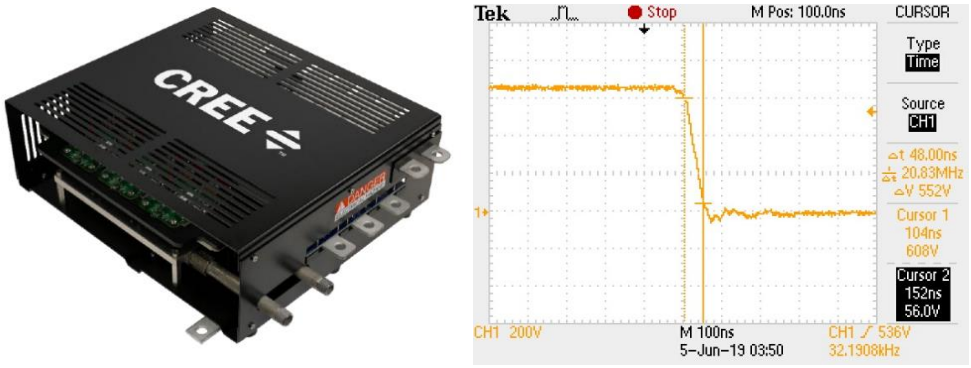

Figure 2.3. (a) Cree CRD200DA09E three-phase evaluation unit's (b) SiC MOSFET devices have turn on/off times of 48 ns.

Table 2.1. Summary of power electronic inverter platforms employed in machine testbed.

Manufacturer	Model No.	Device	Slew Rate
Toshiba	VFS15-4075PL-W	Si IGBT	2,821 V/μs
Cree	CRD200DA09E	SiC MOSFET	11,500 V/μs

SiC motor drive development. The Cree CRD200DA09E three-phase evaluation unit only includes the TLSS inverter and DC link capacitors, therefore a controller was developed, and hardware was added to the system for motor drive capabilities. The design and hardware implementation of the SiC motor drive system was presented in [61].

Typhoon HIL 402. The Typhoon HIL 402 in Fig. 2.4 [62] is a hardware-in-the-loop (HIL) system that allows for safe, reliable, and cost-effective emulation of power stages and verification of controller design for a wide range of applications. While the HIL 402 is effective for controller development, it can also be used as a system level controller for rapid control prototyping (RCP) of system plants. In this application for the machine testbed, the HIL 402 is used for RCP of the SiC inverter to drive a 5 hp induction motor. Through Typhoon HIL's schematic editor, PWM switching schemes are generated and

interfaced to the SiC inverter via the HIL 402's 96 digital and analog I/O pins. Using Typhoon HIL's SCADA panel, the 402 can monitor and control a machine in real time.

Figure 2.4. Typhoon HIL 402.

Sinusoidal pulse width modulation. The sinusoidal PWM (SPWM) switching scheme compares three 120º displaced sinusoidal reference waveforms with a triangular carrier waveform, which produces a switching signal for each leg of the TLSS inverter. When the resulting leg switching signal is high, the top switch of the inverter leg is on, while the bottom is off. When the switching signal is low, the top switch is off while the bottom is on. A constant V/Hz algorithm can be implemented by varying the magnitude and frequency of the sinusoidal reference waveforms, which gives control of the phase voltage and current of the motor drive. By keeping the V/Hz ratio constant, the magnetizing flux of the machine is kept constant up to the rated machine speed. The SPWM switching waveforms can be seen in Fig. 2.5, where the frequency of the triangular carrier waveform is the switching frequency f_s of the drive. The modulation index m_i is defined as the ratio between the amplitude sinusoidal reference waveforms and the triangular waveform. The motor fundamental frequency m_f is the frequency of the sinusoidal reference waveforms and controls the speed of the motor.

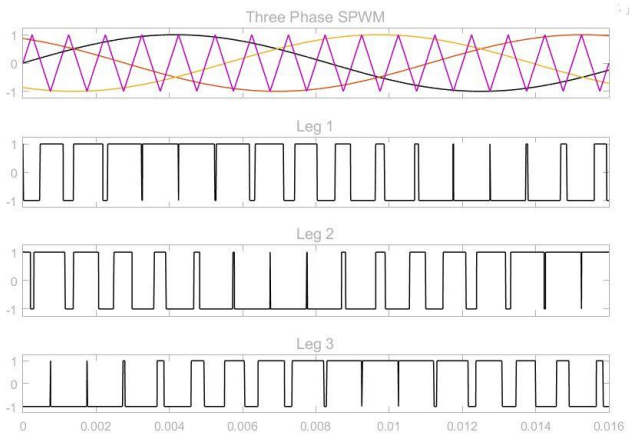

Figure. 2.5. SPWM switching scheme with resulting leg gating signals, m_i = 1, m_f = 60 Hz, f_s = 1 kHz.

A dead time t_d is also specified for PWM inverters as the minimum amount of time a switch from a leg of the inverter must wait to turn on after the other switch in the leg has turned off, which prevents the dangerous condition of shorting the DC link capacitors. The peak output phase voltage for SPWM is ½ of the dc bus voltage:

$$V_{AN,peak} = \frac{V_d}{2} \tag{2.1}$$

Converting the peak phase voltage to an RMS line-to-line voltage produces:

$$V_{LL,rms} = \sqrt{3}\frac{V_{AN,peak}}{\sqrt{2}} = \sqrt{3}\frac{V_{dc}}{2\sqrt{2}} = 0.612V_{dc} \tag{2.2}$$

By considering the modulation index, the output rms line-to-line voltage to the motor is:

$$V_{LL,rms} = m_i 0.612V_{dc} \tag{2.3}$$

Space vector pulse width modulation. The space vector PWM (SVPWM) switching scheme synthesizes an equivalent space vector that rotates in time at m_f by using the eight allowable switching states and minimizes the number of switching events for a given f_s. The SVPWM algorithm continuously calculates the appropriate duty cycle

to place the space vector in the proper location of the α-β plane, where the current V_k and next V_{k+1} switching states are used and T_s is the switching frequency period.

$$V = \frac{T_k}{T_s} V_k + \frac{T_{k+1}}{T_s} V_{k+1} \tag{2.4}$$

By properly employing the V_0 and V_7 zero state vectors, transitions between switching states can be achieved by switching just one leg of the inverter, which helps to minimize switching losses. The eight SVPWM vectors are shown in Fig. 2.6, while the corresponding switching states are shown in Fig. 1.2. Each switching frequency period is comprised of time in the current state, next state, as well as the zero state vectors:

$$T_s = T_k + T_{k+1} + T_0 + T_7 \tag{2.5}$$

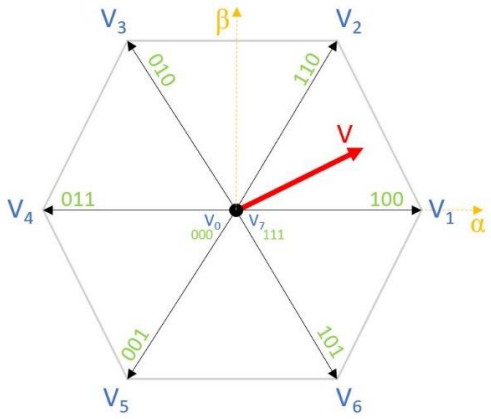

Figure 2.6. A space vector is synthesized in the α-β plane by modulating the eight permissible switching states of the TLSS inverter onto the motor windings.

Following a similar approach to SPWM, for SVPWM the peak output line-to-line voltage is equal to the DC bus voltage, which produces the line-to-line rms voltage:

$$V_{LL,rms} = \frac{V_{dc}}{\sqrt{2}} \rightarrow m_i 0.707 V_{dc} \tag{2.6}$$

From this analysis, the SVPWM switching scheme is superior to the SPWM switching scheme due to improved utilization of the DC bus. SPWM must go into overmodulation

to achieve the same output voltage that is possible with SVPWM. Therefore, SVPWM is the switching scheme of choice in this design.

Typhoon HIL schematic editor model. Open loop switching models for SVPWM were developed in the Typhoon HIL Schematic Editor, as shown in Fig. 2.7.

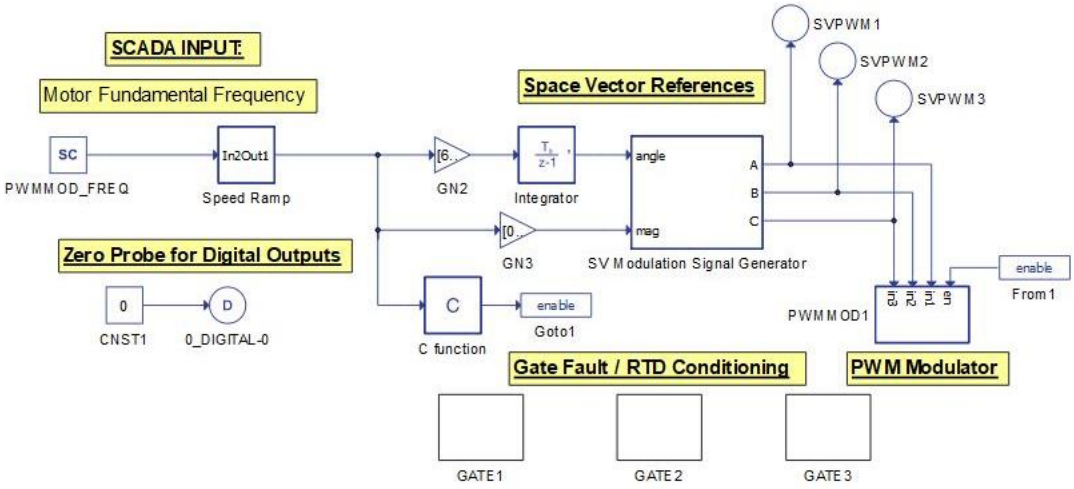

Figure 2.7. Schematic Editor Model for SVPWM switching scheme.

The model begins with a SCADA input block that receives the m_f speed command from the HIL SCADA Panel, which can be updated in real time from a PC. Next, a speed ramp rate limiter is implemented that allows the motor to accelerate smoothly to full speed in a specified time (10 seconds is used in this work as acceleration isn't important for the application). This allows for smooth speed transitions to avoid a sudden change in the net flux vector of the motor, which would produce undesirable speed pops as the rotating inertia of the motor attempts to change instantaneously. Next, the rotating angle is created by scaling m_f by 2π and integrating. A parallel branch is used to maintain a constant V/Hz ratio for the induction motor being driven. A "C" function block enables the PWM switching of the inverter when there is an m_f command greater than zero. For the

SVPWM scheme, the Clarke Transformation is applied to the sinusoidal reference waveforms. The α-β components are then used to locate the proper sector where the space vector is located. The duty cycles are calculated for the zero (V_0, V_7) and nonzero vectors (V_1-V_6). The result at the output of the subsystem is a SVPWM reference waveform. The SVPWM references are then compared to a PWM Modulator. Here the modulator compares the reference waveforms to a triangular waveform. The resulting PWM signals can be assigned to digital output pins on the HIL 402. The gate subsystem blocks are used to initialize digital inputs to measure the temperature of each of the SiC half-bridge modules in HIL SCADA.

Typhoon HIL SCADA panel. The HIL SCADA panel for real time monitoring and speed control is shown in Fig. 2.8, along with a plot of the SVPWM reference waveforms and the associated PWM gating signals for each leg of the inverter. Gate driver digital pins can be controlled in real time and each module's temperature is displayed in real time. In the SCADA panel, the motor speed command m_f is sent to the Schematic Editor in real time. The SCADA scope displays relevant control signals, such as the SVPWM reference waveforms and gating signals, as shown in Fig. 2.8 (b).

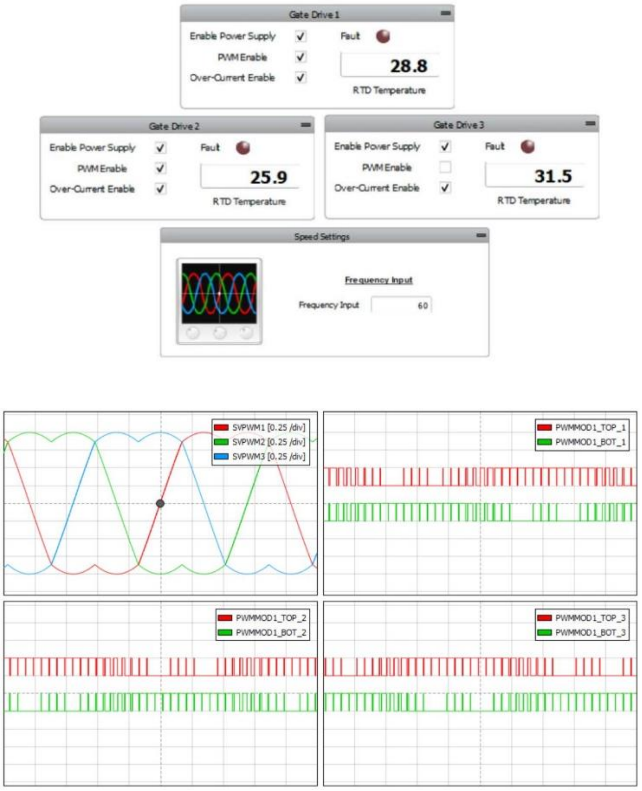

Figure 2.8. (a) HIL SCADA Panel and (b) SVPWM (m_f = 60 Hz, m_i = 1) reference waveforms and generated gating signals. The labeled PWM waveforms correspond to the respective leg, where TOP refers to switches 1, 3, and 5 while BOT refers to switches 2, 4, and 6.

Motor drive hardware. As previously mentioned, the Cree SiC evaluation unit does not come with a rectifier on the front end, thus a three-phase rectifier was installed to rectify the 480 V AC input to the dc bus of the CRD200DA09E SiC inverter, and a variac was used to slowly ramp up the voltage of the DC bus capacitors, which prevented large inrush currents during the initial energization. During operation, the nominal DC bus voltage was ~680 VDC. The inverter uses the gating signals generated by the Typhoon HIL 402 to produce the three-phase PWM waveforms for the induction motor. The HIL 402 is also connected to a PC for real time motor drive monitoring. Through the HIL SCADA panel on the PC, motor speed commands are sent to the testbed for real

time motor speed adjustments. A switch dead time of t_d = 2 µs was used for all test runs in this research. An increase in EMI resulting from high switching frequencies and fast dV/dt turn on/off times caused initial interference between the controller and the SiC inverter. To mitigate these effects, in house shielding was developed to protect the gating signals from noise induced by the inverter EMI. A diagram of the complete SiC motor drive is shown in Fig. 2.9.

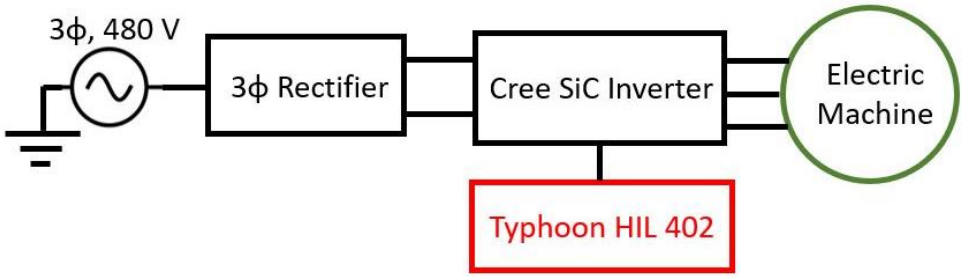

Figure 2.9. SiC motor drive testbed diagram.

Motors and Modification Design

As mentioned in the literature review, it is not possible to directly measure the EDM bearing currents without modifying the machine. To do this, a 5 hp, 4 pole, 460 V, three phase Toshiba squirrel cage IM was disassembled and modified. The bearing seats in the frame end housing were widened slightly with a mill, and polyoxymethylene sleeves were inserted on both the DE and NDE, which isolated the outer race of the bearing from the grounded machine frame. A wire was attached to the outer race of the bearings with silver epoxy and grounded to the frame of the machine. The modified induction machine can be seen in Fig. 2.10.

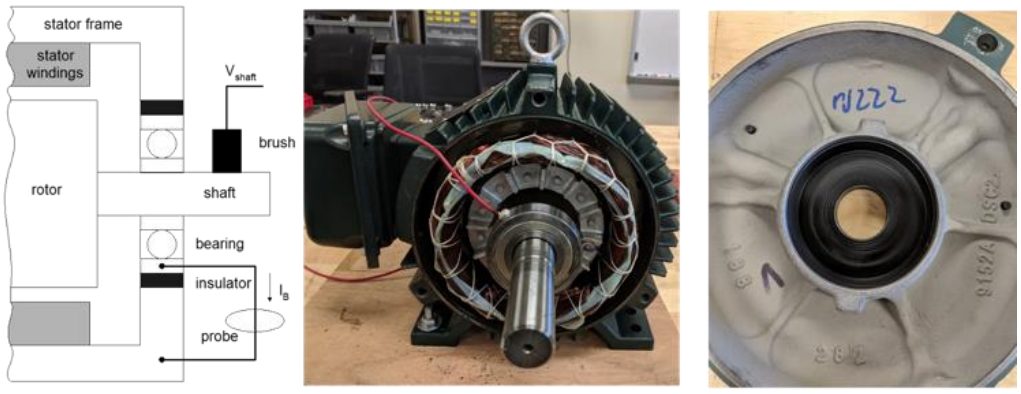

(a) (b) (c)

Figure 2.10. (a) Diagram of motor modification for bearing current measurement, (b) jumper wire is attached to outer bearing race with silver epoxy, and (c) a polyoxymethylene sleeve is installed in the bearing seat to isolate the bearing outer race from the frame of the machine.

The same modification process was performed on the machine used for no load testing, as shown in Fig. 2.1.

A loading machine is also used to apply torque to the machine under test. The machine used is a 5 hp, 4 pole, 460 V, three phase Leeson squirrel cage IM. A summary of the machines used in the machine testbed is highlighted in Table 2.2. The motor's 6306 bearings have an L_{10} lifetime of 200,000 hours (~23 years) for an equivalent dynamic bearing load of 240 lbs and a rotational speed of 1800 RPM.

Table 2.2. Summary of induction machines employed in the machine testbed.

Manufacturer	Model No.	Voltage	Rated Speed	HP	Bearings
Toshiba	0054SDSR41A-P	460	1755	5	SKF 6306-2Z/C3GJN
Toshiba	0054SDSR41A-P	460	1755	5	SKF 6306-2Z/C3GJN
Marathon	VVB184THTS8028ESL	460	1750	5	N/A

Experimental Parameter Control

Extensive engineering work and design was performed on the experimental testbed to control several of the testbed's parameters.

Machine loading. For motor load control, an ABB ACS800-U11-0020-5 regenerative VFD was used to send torque commands to the generating machine in Fig. 2.1. This also acted as a means for controlling the bearing temperatures, as bearing temperature is dependent on machine load. Using the ABB DriveWindow 2.40 software, torque commands are sent via PC to the ABB drive, which then applies the proper current to the load machine, which in turn supplies the desired torque to the machine under test. An insulated shaft coupling was used to mechanically connect the loading machine to the motoring machine. This prevented bearing currents from occurring in one machine due to the shaft voltages produced by the other machine. The specifications of the ABB regenerative VFD are shown in Table 2.3, and an electrical schematic of the regenerative drive is provided in Fig. 2.11.

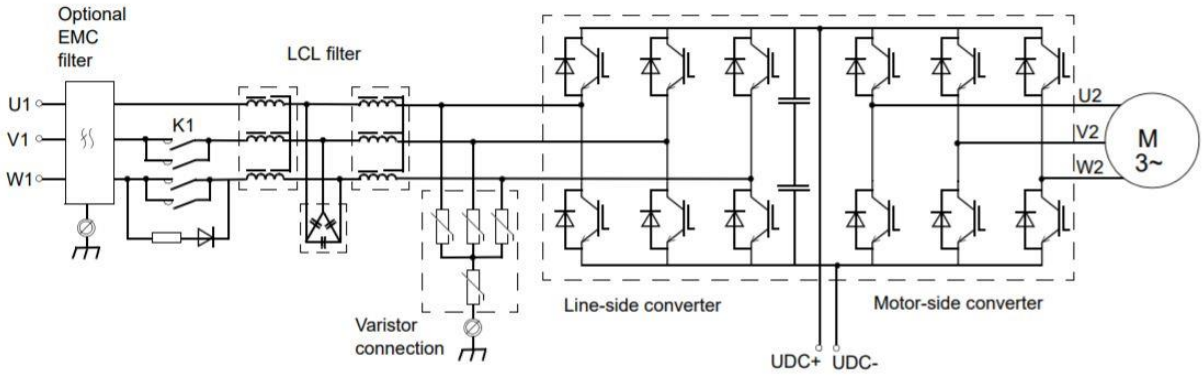

Figure 2.11. The active rectifier (line-side converter) of the ABB ACS800-U11-0020-5 allows for bidirectional power flow, enabling the loading machine to act as a generator [63].

Table 2.3 Technical specification of the regenerative VFD used for motor loading.

Manufacturer	Model No.	Voltage	HP
ABB	ACS800-U11-0020-5	460	15

Bearing temperature measurement. For acquisition of the bearing temperatures during operation, NTC 3950 thermistors were attached to the outer races of both the DE and NDE bearings with silver epoxy, and an MCU was used to read the thermistor voltage signal. To prevent conductive EMI from affecting the measurement, the thermistors were first coated with a layer of thermally conductive and electrically insulating epoxy before being attached to the outer races. For the prevention of radiated EMI, a 1 kHz low pass filter was installed at the MCU analog input pins to attenuate the PWM switching frequency harmonics. The bearing temperature sensing system can be seen in Fig. 2.12. A summary of the temperature data acquisition components and design values can be seen in Table 2.4. The EMI preventative measures taken to improve the thermistor signal drastically improved the signal and the temperature measurement, as can be seen in the signal measurements of Fig. 2.13.

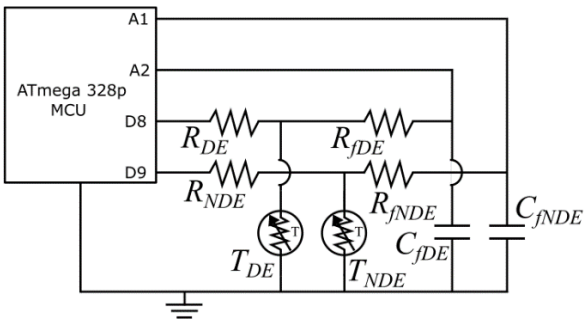

Figure 2.12. Thermistor signal processing circuit for bearing temperature measurement.

Table 2.4. Bearing temperature sensing circuit component summary.

Component	Description	Value
ATmega 328p MCU	MCU used to measure thermistor signal	-
$T_{NDE,DE}$	NTC 3950 Thermistor	100 kΩ
$R_{NDE,DE}$	series resistor with thermistor for voltage divider	100 kΩ
$R_{fNDE,fDE}$	low pass filter resistor	670 kΩ
$C_{fNDE,fDE}$	low pass filter capacitor	220 pF

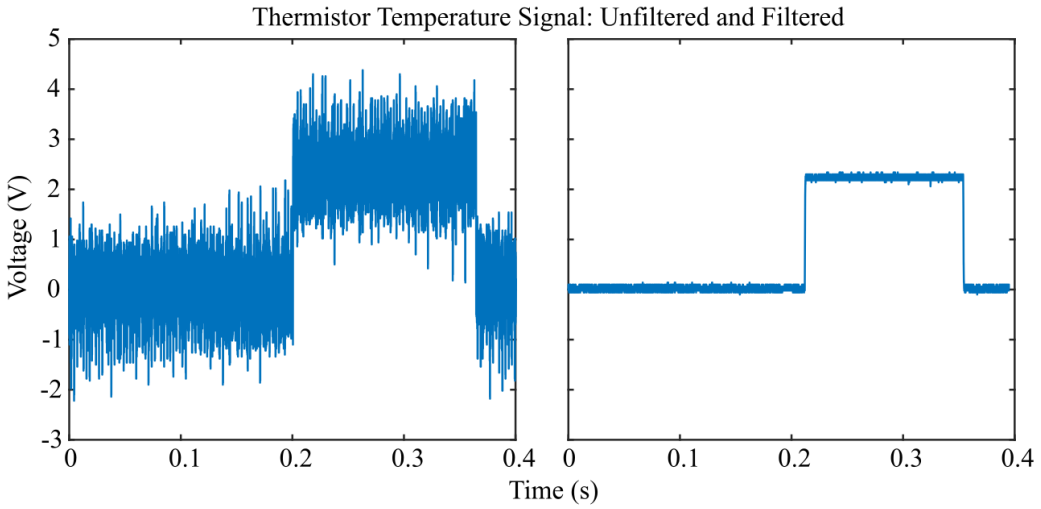

(a) (b)

Figure 2.13. Thermistor temperature signal (a) before and (b) after EMI preventative measures were taken. The fast rise times and high switching frequencies of the PWM inverters produce significant parasitic noise on nearby instrumentation.

Digital pins 8 & 9 of the MCU were used to switch the thermistor on for a measurement and off when a measurement was not taking place. This prevents I^2R losses from adding to the change in thermistor resistance, which would produce erroneous temperature measurements. To extract the bearing temperature from the thermistor voltage signal, the following mathematical approach was taken. First, by measuring the voltage at the divider between $R_{NDE,DE}$ and $T_{NDE,DE}$ it is possible to extract the thermistor resistance.

$$R_{T_{NDE,DE}} = \frac{V_{T_{NDE,DE}}}{V_{DIG} - V_{T_{NDE,DE}}} R_{NDE,DE} \tag{2.7}$$

Then the temperature of the thermistor can be calculated using the following relationship:

$$T = \frac{1}{\frac{1}{T_0}+\frac{1}{B}\log\left(R_{T_{NDE,DE}}-R_{T_{NDE,DE_{T_0}}}\right)} \tag{2.8}$$

Where T is the bearing temperature in Kelvin, T_0 is the ambient/room temperature, B is the thermistor constant, $R_{T_{NDE,DE}}$ is the thermistor resistance, and $R_{T_{NDE,DE_{T_0}}}$ is the thermistor resistance at T_0. A MATLAB script was developed to read the thermistor signal and convert it to a voltage using the various thermistor parameters and Eqs. (2.7-2.8). The script developed to read the thermistor temperature can be found in Appendix A.

Bearing temperature control. For bearing temperature control, silicone heating pads were applied to the DE and NDE housing of the motoring machine to artificially warm the bearings as desired.

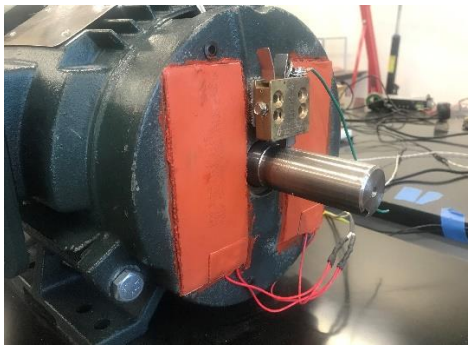

Figure 2.14. Silicone heating pads applied to the DE housing for bearing temperature control.

Motor speed. The speed of the motoring machine of Fig. 2.1 is controlled by the fundamental frequency of the inverters, a parameter on the Toshiba Si-based VFD and a graphical user interface control inside of the Typhoon HIL Model for the SiC drive.

Data Acquisition

To study EDM bearing currents, a data acquisition system was developed to extract shaft voltages and bearing currents with a Tektronix MDO3014 oscilloscope. A MATLAB script implementing Standard Commands for Programmable Instruments (SCPI) was developed to control the oscilloscope from a PC. Measurements of the EDM bearing current transients revealed that the bearing discharge frequencies are in the range of 1-10 MHz (see Ch. 3) depending on the measurement wire parasitic inductance. Therefore, to satisfy the Nyquist sampling criterion, a sampling frequency of 50 MHz was selected. This enabled accurate sampling of the high frequency EDM transients. The oscilloscope can capture 10M samples per channel per acquisition, therefore 200 ms of shaft voltage and EDM bearing current data could be collected during each collection event. The data acquisition hardware setup is shown in Fig. 2.15, and summarized in Table 2.5.

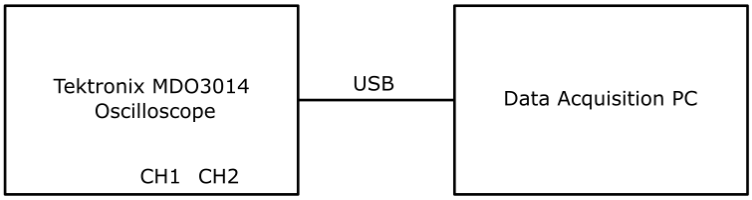

Figure 2.15. Shaft voltage and EDM bearing current data acquisition hardware diagram.

Table 2.5. Summary of data acquisition hardware.

Component	Manufacturer	Model No.
Oscilloscope	Tektronix	MDO3014
Voltage Probe	Tektronix	TPP0250
Current Probe	Tektronix	TCP0030A

The MATLAB script developed to control the oscilloscope and transfer the channel data to the PC can be found in Appendix B. Once the data is successfully transferred to the MATLAB environment, signal processing can begin. Signal processing of the shaft voltage and EDM bearing current channel waveforms will be discussed further in Ch. 5.

Bearing Testbed

An additional testbed was developed which enabled control of the EDM discharge parasitics. This testbed allowed for precise control of the discharge voltage and current, the measurement wire inductance L_w, and the rotor-to-frame capacitance C_{rf}, which is the primary parasitic component that stores the shaft energy prior to discharge. Tuning and alteration of these components and parameters allowed for greater understanding of the discharge characteristics and transients. This section will discuss both the mechanical and electrical design of the bearing testbed. The complete bearing testbed can be seen in Fig. 2.16.

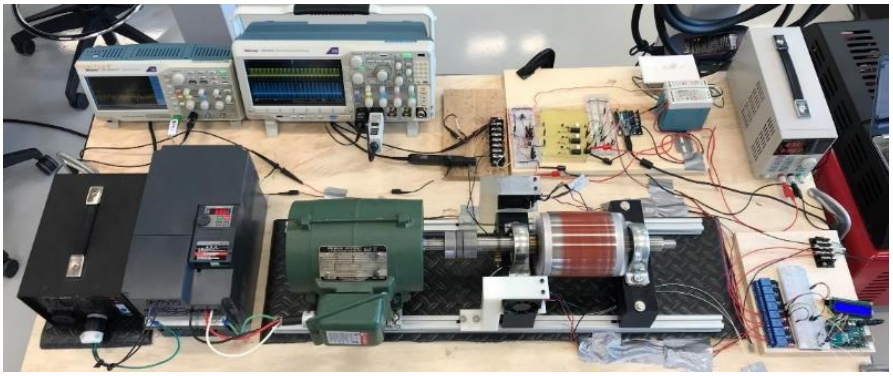

Figure 2.16. Bearing testbed used for EDM damage assessment and vibration accumulation testing.

Mechanical Design

This section highlights the mechanical design of the bearing testbed. The mechanical design was engineered to emulate a motor under typical VFD operation.

Setup and design considerations. In this testbed, a 1 hp IM (green) is used to spin up the 5 hp Toshiba rotor (orange), which is the same rotor that is used in the Toshiba 0054SDSR41A IM from the machine testbed. Again, an insulated shaft coupling is used to prevent the shaft voltages of the green IM of Fig. 2.16 from appearing on the shaft of the orange rotor under test. A VFD is used to drive the IM. This design was selected for two reasons: first, by spinning up the rotor to rated speed externally, the desired shaft voltage and bearing current discharge amplitude can be applied to the bearing under test in a controlled manner. For this testbed, the bearing under test is the DE bearing of the orange rotor. Second, the same 5 hp orange rotor is used as in the machine testbed because it was determined that the axial and radial forces of the rotor alter the discharge phenomenon, which has been demonstrated in [25]. Two conductive pillow blocks are used to mount the rotor bearings to the testbed.

Bearing temperature control. To control the bearing temperature, two heater mounts were 3d printed. Two 250 W heaters were mounted on each side of the DE bearing of the orange rotor. A fan integrated into each heater was used to apply heat to the bearing. This method successfully allowed for bearing temperatures of 20-60°C, the same operational temperatures for the bearings inside of the motors of the machine testbed. Relays controlled by an MCU were used to control the bearing heating. The code used to implement the bearing temperature control can be found in Appendix C.

Electrical Design

EDM switching circuit design and operation. To control the amplitude of the discharge that the bearing is experiencing, a switching circuit was developed with MOSFETs and a microcontroller unit (MCU), as can be seen in Fig. 2.17.

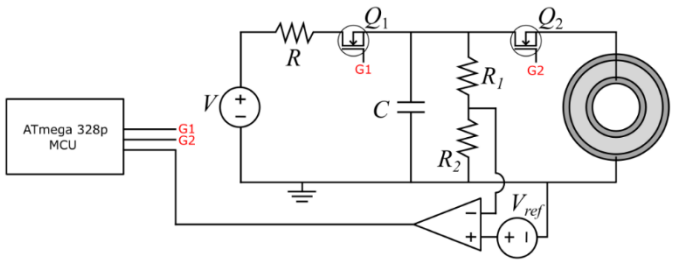

Figure. 2.17. Bearing testbed circuitry to control the discharge amplitude.

The system operates as follows: first the MCU turns on switch Q_1 to charge the capacitor C. Then, once the voltage across the capacitor is equal to the supply voltage V, switch Q_1 is turned off and switch Q_2 is turned on, which allows the electrostatic energy stored in the capacitor to be discharged through the bearing. The resistive divider comprising R_1 and R_2 is used to sense when a discharge occurs by comparing the voltage of the divider with a reference voltage V_{ref} that is less than the supply voltage V. When the voltage of the divider is less than the voltage of the reference, the output of the op amp comparator is driven high, which notifies the MCU that a discharge has occurred. A discharge counter is then incremented within the MCU, and the process repeats. Here the capacitor C emulates the rotor-to-frame capacitance C_{rf}, and the supply voltage V is chosen as the desired discharge voltage. To connect the circuitry to the shaft of the orange rotor under test, jumper wires along with a carbon shaft brush were used. This inevitably introduces a parasitic inductance into the discharge path. Details on the effects of this inductance are highlighted in Ch. 3.

Large values were selected for R_1 and R_2 such that the time constant $(R_1 + R_2)C$ is much larger than the time it takes for a discharge to occur after Q_2 is closed. This ensures that the discharge counter is incremented only when a discharge occurs within the bearing. An oscilloscope capture of discharges applied to a bearing is shown in Fig. 2.18 for a 10V, 400mA test. The discharge shape emulates discharges that are seen from experimental measurements on inverter-driven machines [24], with the key difference that the circuitry allows for continuous discharge amplitude control. The code developed to operate the aforementioned process can be found in Appendix D.

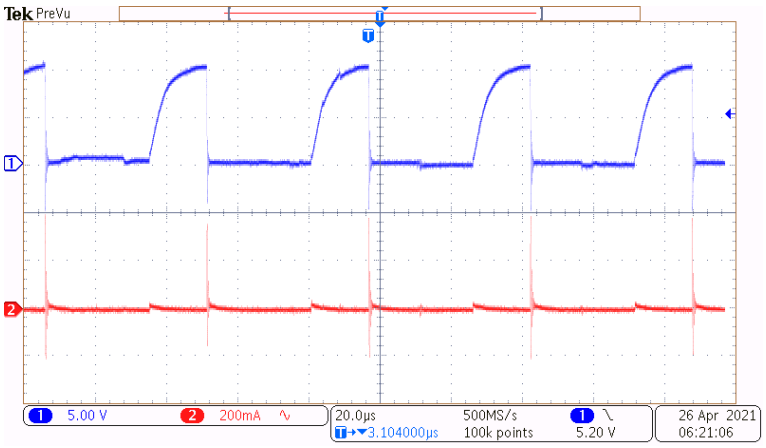

Fig. 2.18. Experimental shaft voltage (blue) and bearing current (red) discharge measurements on the bearing testbed for a 10V, 400 mA test.

Testbed Novelty

This testbed allows for great flexibility in testing various bearing voltages, currents, and discharge energies, all by modifying the discharge components. The testbed is novel in two ways: first, no research program in the literature has applied the exact electrostatic discharging waveforms to the bearing under test as seen in a real motor drive system, most just assume a pulsed square wave [52, 53]. Second, the tunable energy storage components of the discharge circuitry and the discharge voltage can be selected

to understand the effects of different discharge energies on EDM damage. This will provide much more data and information to researchers about what is happening inside the bearing during an EDM event.

Bearing Testbed Vibration Sensor

To track bearing vibration over time, the TE Connectivity 1-1000288 shielded piezo film sensor was mounted onto the pillow block of the bearing testbed. The shielding prevents the large EMI pulses during an EDM discharge from infecting the vibration signal measurement. The vibration signal was recorded in the time domain via oscilloscope and stored for further signal processing.

CHAPTER THREE

Modeling of Bearing Discharges in an Electrical Machine

This chapter details the circuit modeling of the bearing discharge characteristics and transients, shows how the circuit components affect the discharge phenomenon, and connects the inverter CM voltage to the EDM phenomenon. Two separate models are presented. First, a low-level model is developed that details the discharge parasitics that play a role in the discharge phenomenon. Then, a higher-level modeling approach that includes the inverter CM voltage is taken to model shaft voltages and bearing currents in unmodified machines.

Bearing Discharge Parasitic Modeling

Circuit modeling was performed for the three different discharge scenarios: a modified induction machine with polyoxymethylene sleeves to enable bearing current measurement, the bearing testbed, and an unmodified induction machine.

When measuring shaft voltage and bearing current discharges the discharges appear as a damped sinusoid. The damped sinusoid ringing effect is due to parasitic inductances and capacitances within the measurement circuit along with the discharge resistance. Experimental measurements were performed with a network analyzer and a function generator to extract the parasitic component values, as shown in the subsequent sections.

To extract the parasitic values, a network analyzer's S_{11} parameters were employed, which produce a reflection coefficient Γ, a complex value containing

magnitude and phase information that is the ratio between the reflected and incident parts of an electromagnetic wave.

$$\Gamma = \frac{V_{reflected}}{V_{incident}} \tag{3.1}$$

The impedance of the system under measurement can be obtained from the reflection coefficient by use of the system characteristic impedance Z_0:

$$Z = R + jX = Z_0 \frac{1+\Gamma}{1-\Gamma} \tag{3.2}$$

The parasitic inductance or capacitance can then be extracted from the impedance measurement. Alternatively, a first order step function response can be analyzed when the parasitic circuit components are isolated into first order circuits. Here a function generator can be used to apply a step function to the circuit under test. Assuming an ideal step with ∞ slope, the voltage for an RC circuit and the current for an RL circuit are as follows:

$$v(t) = V\left(1 - e^{-\frac{1}{RC}t}\right) \tag{3.3}$$

$$i(t) = \frac{V}{R}\left(1 - e^{-\frac{R}{L}t}\right) \tag{3.4}$$

where the first order time constant τ is equal to RC and L/R for the RC and RL first order circuits, respectively. The time constant τ is the time when the dependent variable reaches $(1\text{-}e^{-1}) \approx 63.2\%$ of its final value, as shown in Fig. 3.1.

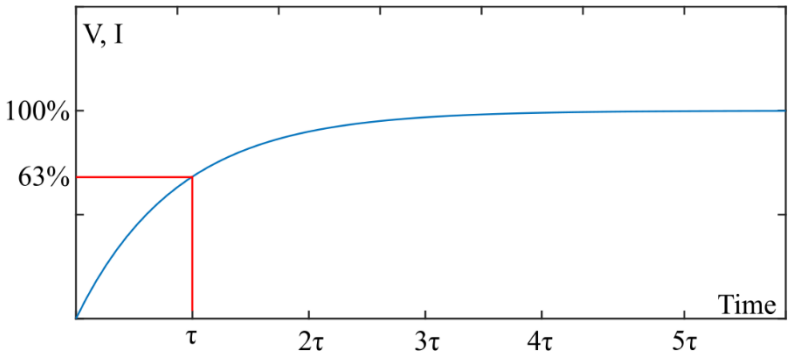

Figure 3.1. First order RC and RL capacitor voltage and inductor current reach ~63% of their final value once τ time has passed after the step function is applied, respectively.

Therefore, a simulated first order step response can be fit to experimentally obtained data to extract the parasitic capacitance or inductance. To do this, a function generator is utilized with a source resistance of 50 Ω. This parasitic extraction method contains some error however, as it is assumed from the previous mathematical analysis that the function generator contains an ∞ slope on the rising edge, which is not possible with real laboratory equipment. Consequently, this measurement method will contain some error. Because of this, the step response results will mainly be used as a secondary check for the VNA extraction method, as the step response method gives a fairly accurate estimate of what the parasitic value is for large L and C components.

Bearing Testbed Discharge Model

An experimental measurement of shaft voltage and bearing current for the bearing testbed is shown in Fig. 3.2. Here the period of the oscillations is ~280 ns, thus the bearing testbed experiences discharges at 3.57 MHz due to circuit parasitics.

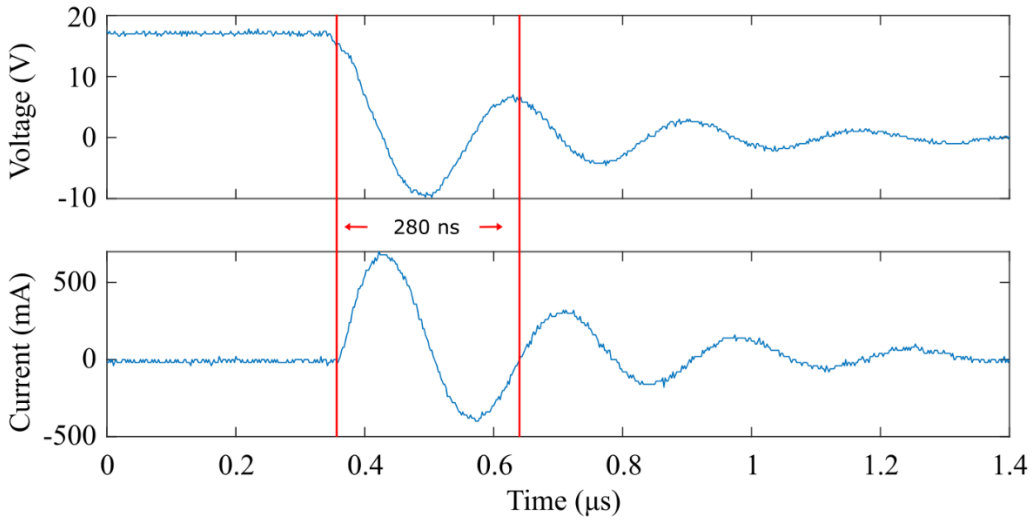

Figure. 3.2. Experimental measurement of a 17V, 700 mA bearing discharge from the bearing testbed.

The equivalent circuit model for the bearing testbed is shown in Fig. 3.3. Wire leads are used to connect the discharge circuitry with the bearing under test, and is accounted for with components L_{wl1} and L_{wl2}, representing the wires leading to and returning from the bearing. The associated resistive components R_{wl1} and R_{wl2} are included. A 2 nF capacitance was chosen to store the energy before the discharge, shown as C_{rf}. The energy stored in this capacitance represents the energy stored in the rotor-frame capacitance prior to discharge. Finally, the discharge is modeled with a parallel RC Circuit, representing the bearing capacitance C_b and the discharge resistance R_b. When a discharge occurs, the switch closes, and the energy stored in C_{rf} is dissipated in the bearing.

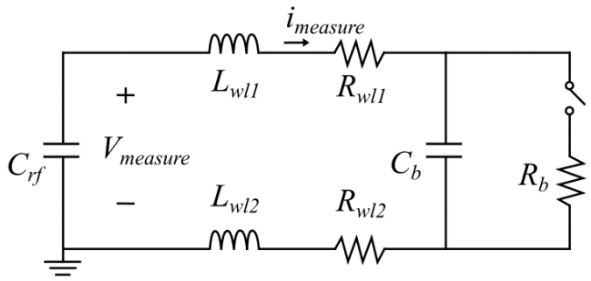

Figure. 3.3. Bearing testbed equivalent circuit discharge model.

Two frequency sweep tests were performed with network analyzer S_{11} parameters to extract the wire lead inductances and the bearing capacitance. First a standstill test was performed to find the wire lead inductance. When the bearing is at 0 RPM, the bearing balls rest directly on the race, which electrically shorts the RC circuit of Fig. 3.3. The rotor frame capacitance C_{rf} was removed from the circuit to prevent its influence on the measurement. To find the bearing capacitance, the network analyzer BNC cable was connected directly across the bearing's inner and outer race while spinning at 1800 RPM. At 1800 RPM, a thin layer of grease insulates the bearing balls from contacting the races, thus a capacitance is formed. The operational temperature of the bearing was kept at 25 °C, which prevented discharges from occurring. The equivalent circuit models for each test to extract L_{wl1}, L_{wl2}, and C_b are shown in Fig. 3.4.

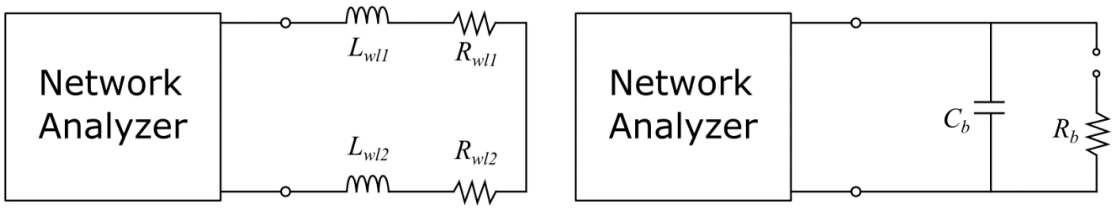

(a) (b)

Figure. 3.4. Equivalent circuit models for extracting (a) lead wire inductance and (b) bearing capacitance for the discharge model.

The S_{11} parameter reflection coefficient was collected over frequencies from 500 kHz to 10 MHz, since this frequency range contains the frequency of each discharge, which does not vary from the value obtained experimentally in Fig. 3.2. Eq. (3.2) was used to calculate the impedance of the test, using the characteristic impedance of the BNC cable used, which is 50 Ω. The results of the frequency sweep are shown in Fig. 3.5. An additional frequency sweep was performed on the 2 nF energy storage capacitance C_{rf} to check its performance at the discharge frequency and to validate the parasitic measurement technique. From Fig. 3.5, it is clear that the measurement technique is validated, and the bearing capacitance measurement agrees with other bearing capacitance measurements reported in the literature for a similar size bearing [56, 64].

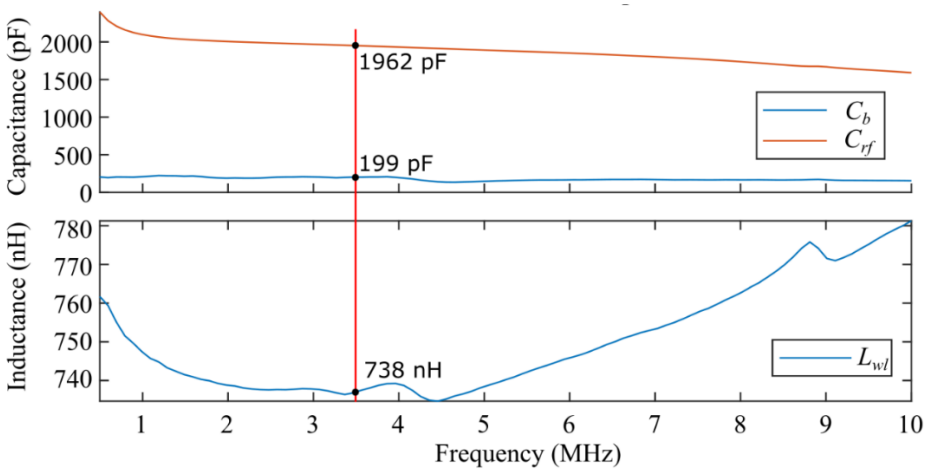

Figure. 3.5. Bearing testbed energy storage capacitance and parasitic component measurements at the discharge frequency.

An additional step response test was performed to validate the wire lead inductance measurement using a function generator. When the bearing is at standstill, the equivalent circuit of Fig 3.4(a) produces a first order RL circuit, when the 50 Ω

impedance of the function generator is included. Therefore, assuming an ideal square wave edge, the current flowing in the circuit during a step response is:

$$i(t) = \frac{V}{R}\left(1 - e^{-\frac{R}{L}t}\right) \tag{3.5}$$

For a 10 V step and 50 Ω source resistance, a curve fit revealed a total measurement wire inductance of ~1 μH. The first order curve fit is shown in Fig. 3.6.

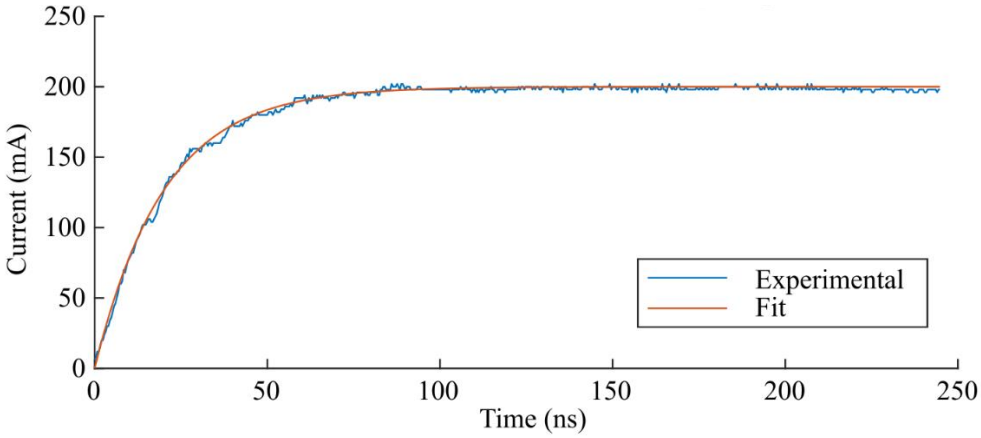

Figure 3.6. Bearing testbed wire lead inductance test step response.

The skin effect theory was used to calculate the wire resistive components R_{wl1} and R_{wl2}:

$$R_{wl1} = R_{wl2} = \frac{R_{wl}}{2} = \frac{\rho l}{A_{eff}} \tag{3.7}$$

$$\delta = \sqrt{\frac{\rho}{\pi f \mu}} \tag{3.8}$$

$$A_{eff} = \pi r^2 - \pi(r - \delta)^2 \tag{3.9}$$

where δ is the skin depth, ρ is the conductor resistivity, l is the length of the conductor, f is the ac frequency, μ is the magnetic permeability, r is the radius of the conductor, and A_{eff} is the effective cross-sectional area due to the skin effect. These equations are valid when $r >> \delta$, and produce $R_{wl1} = R_{wl2} = 48$ mΩ. It was found that slight variations in the

wire resistance due to skin effect and DC resistance were negligible, as the bearing discharge resistance R_b dominated the resistive component of the circuit. The bearing discharge resistance has been reported to be on the scale of 1-10 Ω [6].

The modified LSQ engine optimizer tool in PSpice was employed to fit the simulation shaft voltage and bearing current to experimental data by tuning the circuit component values to minimize the error between the simulation and experimental waveforms. The waveform results from the optimization are shown in Fig. 3.7. To compare the simulation and experimental waveforms, the coefficient of determination (R^2) was computed between the two waveforms, where a value of 0 shows no fit between the curves and a value of 1 is a perfect fit:

$$R^2 = 1 - \frac{R_{SS}}{T_{SS}} \tag{3.10}$$

Here R_{SS} (the residual sum of squares) is the summation of the square of the difference between the simulation and experimental data at each point and T_{SS} (the total sum of squares) is the summation of the square of the difference between the average experimental value and the experimental value at each point.

$$R_{SS} = \sum_{i=1}^{n} \left(v_{sim}(i) - v_{exp}(i) \right)^2 \tag{3.11}$$

$$T_{SS} = \sum_{i=1}^{n} \left(\overline{v}_{exp} - v_{exp}(i) \right)^2 \tag{3.12}$$

Computing the R^2 values for the shaft voltage and bearing current results of Fig. 3.7 produces values of 0.9878 and 0.9912, respectively.

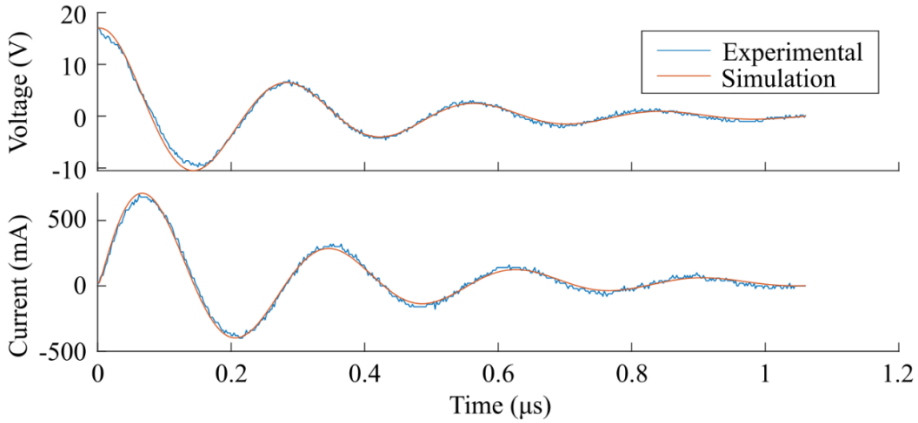

Figure. 3.7. Experimental and simulation results for a 17V, 700 mA discharge on the bearing testbed.

Once the circuit components were optimized, various discharge amplitudes were applied to the model by varying the initial voltage condition on C_{store}. The results were compared with experimental measurements that had the same initial breakdown voltage. The bearing discharge resistance was further tuned to fit the experimental waveforms. The results can be seen in Table 3.1.

Table 3.1. Discharge conditions for fitting simulation to bearing testbed experimental shaft voltage and bearing current.

Discharge Condition	R_b (Ω)	R^2 (V, I)
33 V, 1300 mA	5.68	0.986, 0.990
25 V, 1000 mA	6.80	0.966, 0.986
17 V, 700 mA	6.06	0.988, 0.991
7 V, 250 mA	9.49	0.989, 0.990

From Table 3.1, no R^2 value is below 0.966 for either the voltage or current, therefore the simulation model is verified. To maintain the high R^2 value, the PSpice Optimizer tool had to modify the bearing discharge resistance, tuning it to each discharge condition. In fact, it is expected that the bearing discharge resistance may show some variation between discharges, even discharges of the same amplitude. This can be

attributed to the slight variation in distance between the ball and race of the bearing for each discharge. Therefore, slightly different amplitudes of bearing current can be observed for the same shaft voltage discharge, as will be shown in Chapter Five. A summary of the circuit modeling for bearing testbed discharges is shown in Table 3.2.

Table 3.2. Summary of bearing testbed circuit modeling component values with final values in the "PSpice Optimizer" column.

Component	Literature	Skin Effect	Network Analyzer	Step Response	PSpice Optimizer
L_{wl1}	-	-	369 nH	500 nH	443 nH
L_{wl2}	-	-	369 nH	500 nH	442 nH
R_{wl1}	-	48 mΩ	-	-	50 mΩ
R_{wl2}	-	48 mΩ	-	-	50 mΩ
R_b	1-10 Ω	-	-	-	Table 3.1
C_{rf}	-	-	1962 pF	-	2190 pF
C_b	200-1000 pF	-	199 pF	-	246 pF

Modified Induction Machine Bearing Discharge Model

An experimental measurement of shaft voltage and bearing current for the modified IM is shown in Fig. 3.8. Here the period of the oscillations is ~96.8 ns, thus the modified IM experiences discharges at 10.33 MHz due to circuit parasitics.

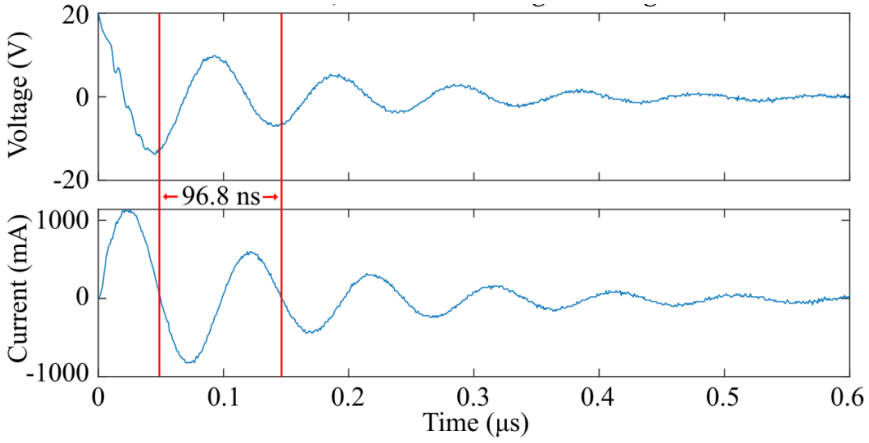

Figure. 3.8. Experimental measurement of a 20V, 1100 mA bearing discharge from the modified IM.

To enable a bearing current discharge measurement, a polyoxymethylene insulating sleeve is installed between the outer race and frame of the machine to isolate the bearing, which introduces an isolation capacitance C_i. A measurement wire is connected between the outer race and the frame of the machine, "forcing" the bearing current through the wire, which also introduces some parasitic impedance comprising of L_w and R_w. The equivalent circuit model for the modified induction machine is shown in Fig. 3.9.

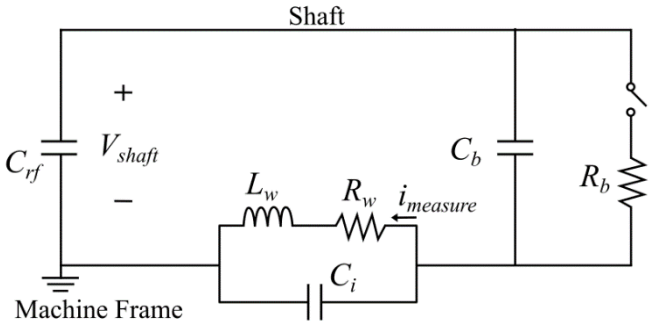

Figure. 3.9. Modified induction machine bearing discharge equivalent circuit model.

Network analyzer S_{11} parameters were used to extract the component values for C_{rf}, C_i, and L_w under rated speed and zero speed conditions. The results from the frequency sweep are shown in Fig. 3.10. The step response component extraction method was also performed for C_{rf}, the results of which can be seen in Fig. 3.11. The model of Fig. 3.9 only contains one bearing, the other is included in the rotor-to-frame capacitance C_{rf}.

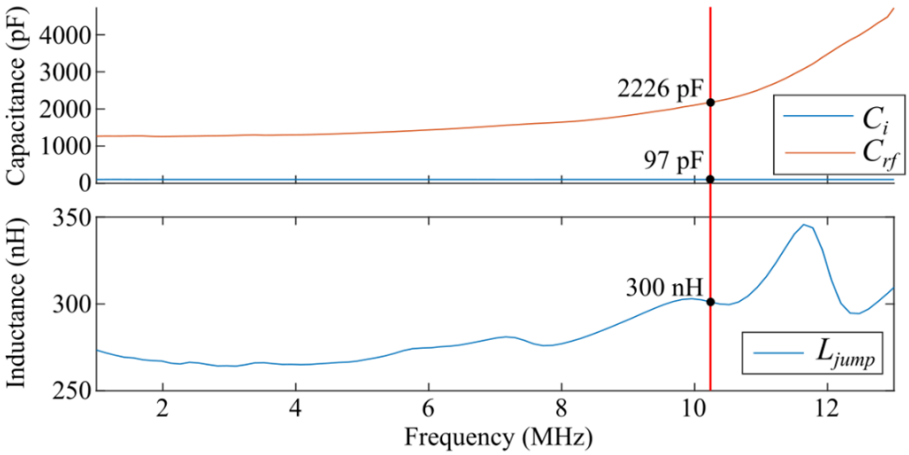

Figure. 3.10. Modified IM parasitic component measurements at the discharge frequency.

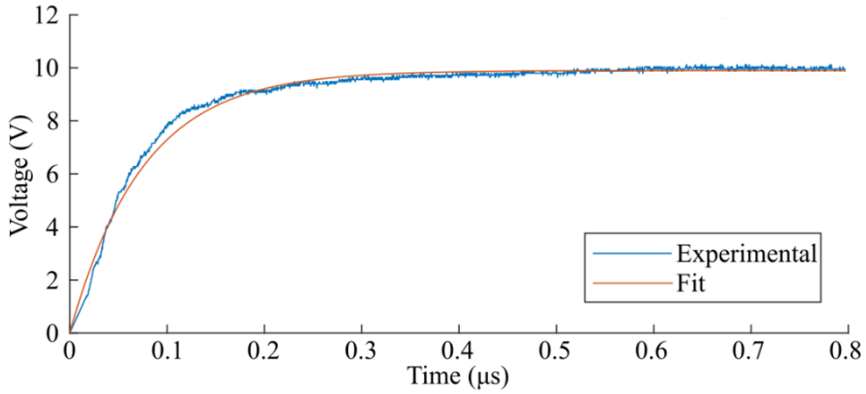

Figure. 3.11. Rotor to frame capacitance voltage step response for modified IM.

For the frequency sweep extraction, values obtained were 2226 pF for C_{rf}, 97 pF for C_i, and 300 nH for L_w. A second measurement of the rotor to frame capacitance using the step response method resulted in C_{rf} = 1500 pF. A similar skin effect analysis was performed for the jumper wire to find its resistance, which produced R_w = 71 mΩ. For the bearing capacitance, the same bearing on the Bearing Testbed is used on the modified IM, therefore the 199 pF measurement remains valid. An additional calculation was performed for the isolation capacitance C_i. The outer race to frame is assumed to have a parallel plate capacitance, therefore the following holds true:

$$C_i = \frac{\varepsilon \varepsilon_0 A}{d} \tag{3.13}$$

where $\mathcal{E}$ is the relative permittivity of polyoxymethylene, $\mathcal{E}_0$ is the permittivity of free space, A is the surface area, and d is the distance between the two plates. 6306 bearings have a diameter of 72 mm and a width of 19 mm, which results in an outer race surface area of 4297 mm^2. Given a polyoxymethylene dielectric constant of 3.7 and thickness of 0.5 mm, the resulting isolation capacitance is 141 pF.

The PSpice optimizer tool was utilized to tune the simulated shaft voltage and bearing current waveforms to match experimental measurements. Bearing discharge resistance values for various discharge amplitudes are detailed in Table 3.3. A summary of the discharge circuit modeling for the modified IM is shown in Table 3.4. Comparing the simulation with experimental measurements resulted in R^2 values greater than or equal to 0.981 for all shaft voltage and bearing current fits. Therefore, the circuit simulation model accurately describes the discharge phenomenon.

Table 3.3. Discharge conditions for fitting simulation to modified IM experimental shaft voltage and bearing current.

Discharge Condition	R_b (Ω)	R^2 (V, I)
20.2 V, 1150 mA	3.25	0.989, 0.994
18.8 V, 1000 mA	3.35	0.983, 0.991
13.4 V, 720 mA	5.00	0.981, 0.989
10.2 V, 560 mA	4.34	0.983, 0.985

Table 3.4. Summary of modified IM circuit modeling component values with final values in the "PSpice Optimizer" column.

Component	Literature	Skin Effect	Calculation	Network Analyzer	Step Response	PSpice Optimizer
L_w	-	-	-	300 nH	-	213 nH
R_w	-	71 mΩ	-	-	-	56 mΩ
R_b	1-10 Ω	-	-	-	-	Table 3.3
C_i	-	-	141 pF	97 pF	-	120 pF
C_{rf}	-	-	-	2226 pF	1500 pF	1045 pF
C_b	200-1000 pF	-	-	199 pF	-	200 pF

Unmodified Induction Machine Bearing Discharge Model

Experimental measurements were performed on an unmodified induction machine to predict the shape of a bearing current discharge (since the machine is unmodified there is no bearing current measurement available). An oscilloscope capture of a shaft discharge event is shown in Fig. 3.12.

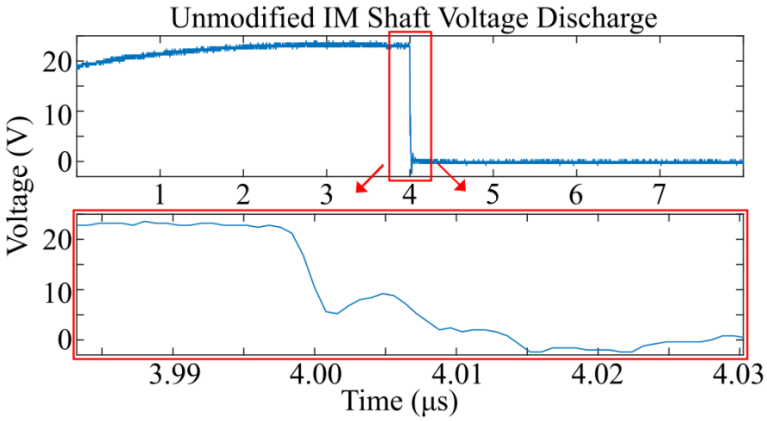

Figure 3.12. A 23 V unmodified IM shaft voltage discharge dissipates in ~17 ns.

When the machine is unmodified, the damped sinusoid behavior is eliminated due to the elimination of the measurement wire parasitic inductance, which is required for a bearing current measurement. The 23 V discharge of Fig. 3.12 goes to 0 V in ~17 ns. This was

modeled in PSpice as a first order RC circuit discharging. The equivalent circuit is shown in Fig. 3.13, with the shaft voltage and bearing current results in Fig. 3.14.

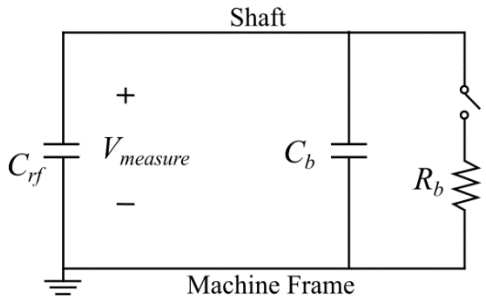

Figure. 3.13. Unmodified induction machine bearing current discharge equivalent circuit model.

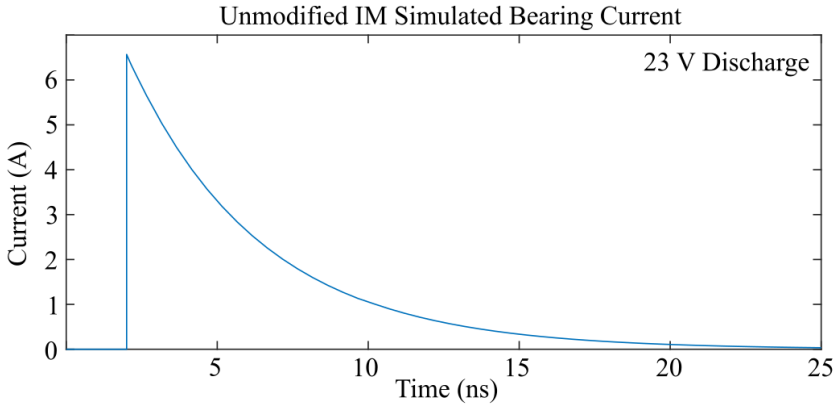

Figure 3.14. Simulated bearing current for a 23 V shaft voltage that dissipates in ~17 ns.

In Figs. 3.13 & 3.14, a value of C_{rf} = 1045 pF and C_b = 200 pF were chosen (results from Table 3.4), as the motor modification to measure the bearing current does not change these component values. For the bearing discharge resistance, a value of R_b = 3.5 Ω allowed the 23 V discharge to dissipate to 0 V within ~17 ns.

Influence of Measurement Wire Inductance on Modified IM Transients

From the previous sections, observation of the discharge transients reveals that the measurement wire inductance alters the time it takes for discharge transients to settle, as well as the amplitude of the bearing current transients. This section will investigate the effects of the measurement wire inductance in detail.

Apparent and actual bearing current. For both the bearing testbed and the modified IM, the bearing current measurements performed were only an apparent measurement. It is not possible to experimentally measure the actual current. This is evident by observing the equivalent circuit models of Figs. 3.3 and 3.9. Here, the apparent measurements were made in the branches consisting of L_w and L_{wl2}, while the actual bearing current that contributes to EDM damage flows in the branch that consists of R_b. The physical meaning of the parallel branch consisting of R_b and C_b is a bearing capacitance due to a lubricant film during operation along with a discharge path that short circuits the bearing capacitance through a small discharge resistance. For this reason, it would be necessary to place a current probe inside of the bearing to get the actual measurement. Therefore, the discharge transients of the actual bearing current will be slightly different than the transients of the apparent bearing current. Since the discharge parasitics are well known, a simulation of the actual bearing current reveals its characteristics, as shown in Fig. 3.15.

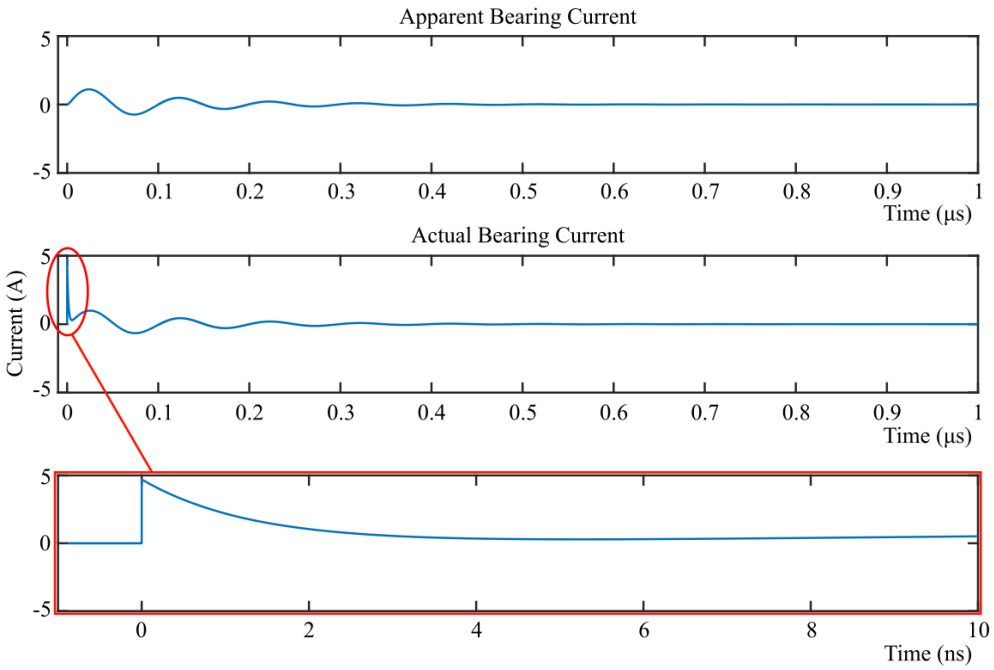

Figure 3.15. Discharge bearing current simulation of the modified IM comparing the apparent and actual bearing currents.

From Fig. 3.15, the actual bearing current contains an additional exponentially decaying transient at the beginning of the discharge due to the small amount of energy stored in the bearing capacitance.

Effect of measurement wire inductance on discharge transient time. To understand the influence of the measurement wire inductance on the bearing current transients, a parameter sweep was performed in PSpice on the modified IM model to observe settling time of the bearing current discharge transient. This can be seen in Fig. 3.16.

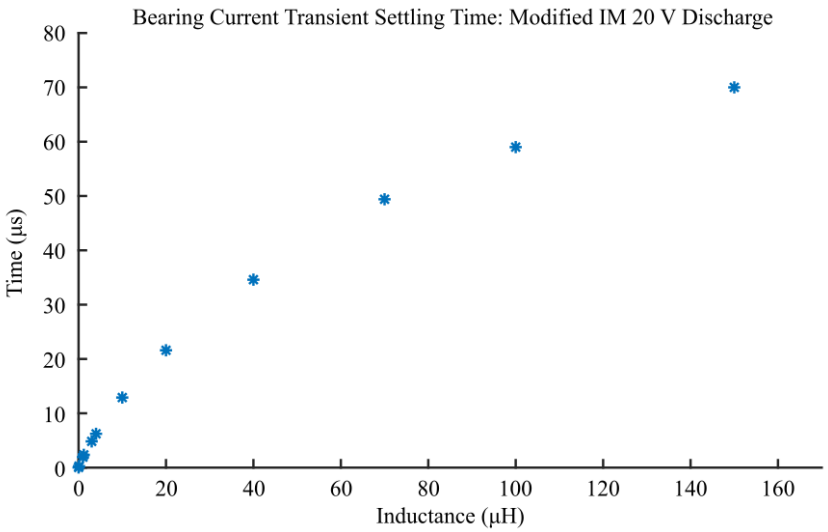

Figure 3.16. The measurement wire inductance affects the time it takes for a bearing current discharge to settle, in this case for a 20V discharge on the modified IM.

As the measurement wire inductance increases, the time for bearing current discharge transients to settle also increases, despite there being the same amount of energy dissipated in the bearing. Since the energy of a 20V discharge is independent of the measurement wire inductance, it follows that the power or rate of energy transfer into the discharge decreases with an increase in measurement wire inductance. With a lower rate of energy transfer, it is hypothesized that bearing current discharges with a longer transient settling time cause less damage to the race and ball surfaces because the energy dissipated in the bearing has more time to propagate through the steel than it would if transient settling time was shorter. This means that an impedance in series with the bearing could prevent EDM damage from occurring within the bearing, extending its lifetime. This hypothesis will be further explored in the FE modeling chapter, Chapter Four.

Comparison of discharge amplitudes. Since the discharge models of Figs. 3.3 & 3.9 are linear systems, the ratio between the peak current in the unmodified IM and the peak apparent current for a modified IM are the same for various shaft discharge voltages, which for the measurements in this research is:

$$\varphi = \frac{\hat{I}_{MOD}}{\hat{I}_{UNMOD}} = 0.2 \tag{3.14}$$

This ratio is dependent on the inductance of the measurement wire L_w. As $L_w \to 0$, the bearing current amplitude approaches $\hat{I}_{UNMOD}$. This ratio is useful because during measurement and characterization of bearing currents it reveals what the peak bearing current would be for an unmodified IM. Using this in tandem with the discharge circuit model gives full knowledge of EDM discharges in an unmodified IM.

Bearing Discharge Modeling with CM Voltage Included

A higher-level shaft discharge model was developed by modeling the dynamics and parasitics of the capacitive voltage divider present in all electric machines. The state space circuit model of the machine capacitive divider is shown in Fig. 3.17. In this model, C_1 represents the stator-to-rotor capacitance, C_2 is the rotor-to-frame capacitance, C_3 is the bearing capacitance, R is the dynamic bearing resistance, L is the parasitic inductance introduced by the measurement wire, and r is an additional resistance added to the model in series with C_1 and C_2 to simplify the mathematical derivations, whose value is chosen so that its effects are negligible. The nodes labeled 1 & 2 represent the outer race of the bearing and machine shaft, respectively. Through modeling in the previous section, it was discovered that the isolation capacitance introduced by the bearing

insulating sleeve has negligible effects on the discharge profile. For this reason, it has been excluded from this state space approach.

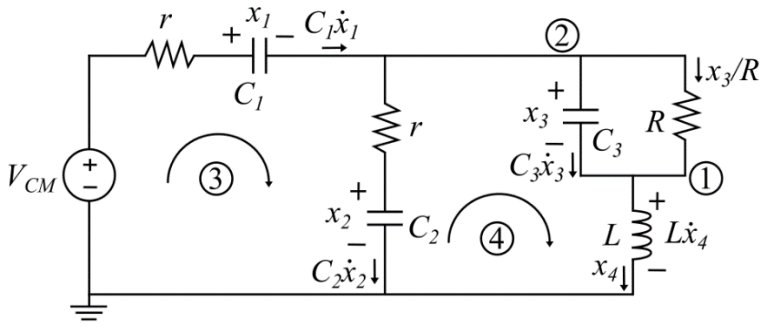

Figure 3.17. State space circuit representation of shaft voltage breakdown and EDM bearing currents.

From the circuit model, nodal and loop equations are written for the nodes and loops labeled 1-4. The equations generated from 1-4 correspond with Eqs. (3.15-3.18), respectively.

$$C_3\dot{x}_3 + \frac{1}{R}x_3 = x_4 \tag{3.15}$$

$$C_1\dot{x}_1 = C_2\dot{x}_2 + C_3\dot{x}_3 + \frac{1}{R}x_3 \tag{3.16}$$

$$V_{CM} = rC_1\dot{x}_1 + x_1 + rC_2\dot{x}_2 + x_2 \tag{3.17}$$

$$x_2 + rC_2\dot{x}_2 = x_3 + L\dot{x}_4 \tag{3.18}$$

Solving for the change in state variables results in the following system of differential equations:

$$\dot{x}_1 = -\frac{1}{2rC_1}x_1 - \frac{1}{2rC_1}x_2 + \frac{1}{2C_1}x_4 + \frac{1}{2rC_1}V_{CM} \tag{3.19}$$

$$\dot{x}_2 = -\frac{1}{2rC_2}x_1 - \frac{1}{2rC_2}x_2 - \frac{1}{2C_2}x_4 + \frac{1}{2rC_2}V_{CM} \tag{3.20}$$

$$\dot{x}_3 = -\frac{1}{RC_3}x_3 + \frac{1}{C_3}x_4 \tag{3.21}$$

$$\dot{x}_4 = -\frac{1}{2L}x_1 + \frac{1}{2L}x_2 - \frac{1}{L}x_3 - \frac{r}{2\mathrm{L}}x_4 + \frac{1}{2L}V_{CM} \tag{3.22}$$

Typically, this system of equations would be linear, with an input V_{CM}. However, the shaft voltage is directly controlled by two variables in the model: the CM voltage V_{CM} and the bearing resistance R. This modeling approach will attempt to capture the dynamically changing bearing resistance. From the previous circuit modeling sections, during a discharge the bearing resistance collapses to a value in the range of 1-10 Ω. When discharges aren't occurring (i.e., the lubricant is intact), the bearing resistance is a much higher value which enables a voltage to be present on the shaft. Therefore, the shaft voltage is influenced by two model parameters: V_{CM} and R. With the bearing resistance as an input, the system of differential equations becomes nonlinear due to the division of the state x_3 with the bearing resistance R, although remains stable because the bearing resistance can only be a positive real number (i.e., permissible values of R can only decrease the shaft voltage. Any increase in shaft voltage is due to V_{CM}, which is bounded by the DC bus voltage). The model outputs of interest are the shaft voltage (node 2) and the apparent bearing current, which are described by the following:

$$V_{shaft} = -\frac{1}{2}x_1 + \frac{1}{2}x_2 - \frac{r}{2}x_4 + \frac{1}{2}V_{CM} \tag{3.23}$$

$$I_b = x_4 \tag{3.24}$$

To solve the model, experimental measurements were made on the modified IM of the CM voltage, shaft voltage, and apparent bearing current. The differential equations were implemented using Simulink. The experimental CM voltage was fed into the model, and the experimentally measured shaft voltage was used as a reference. The shaft voltage computed by the model was compared with the experimentally measured shaft voltage. This comparison produces an error which can be used to actuate the dynamic bearing

resistance to a value which minimizes the error. Thus, the bearing resistance is calculated by a feedback loop that chooses its value in order to drive the simulated shaft voltage to the experimentally measured shaft voltage. The simulated apparent bearing current can then be compared with the experimentally measured apparent bearing current to evaluate the validity of the model. The component values of Fig. 3.17 used in the simulation of the differential equations of Eqs. (3.19-3.22) are given in Table 3.5.

Table 3.5. Simulink state space model parameters.

Component	Description	Value
C_1	stator-to-rotor capacitance	150 pF
C_2	rotor-to-frame capacitance	1 nF
C_3	bearing capacitance	200 pF
L	measurement wire inductance	213 nH
r	computation resistance	1 μΩ
R	dynamic bearing resistance	-

The Simulink schematic used to employ Eqs. (3.19-3.24) is shown in Fig. 3.18, and the model results can be seen in Fig. 3.19. The change in each state is calculated beginning with an initial current of 0 V across all capacitances and 0 A through the measurement wire inductance. The CM voltage and the shaft voltage are fed into the model on the left, and the model outputs are sent to the MATLAB workspace on the right.

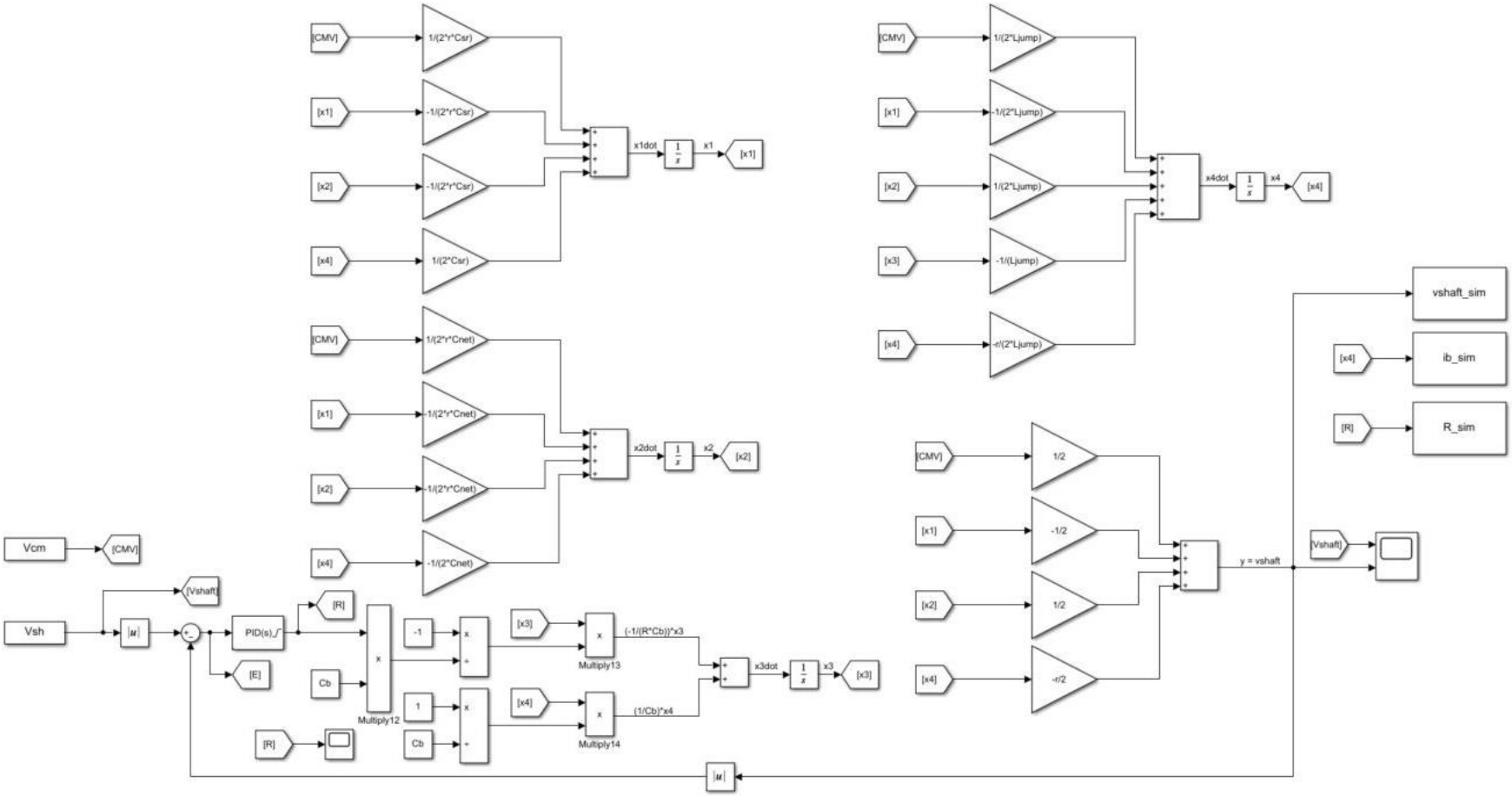

Figure 3.18. Simulink schematic employing the differential equations of Eqs. (3.19-3.24). An experimental shaft voltage measurement is used as a reference to tune the simulated shaft voltage, which results in a bearing resistance calculation.

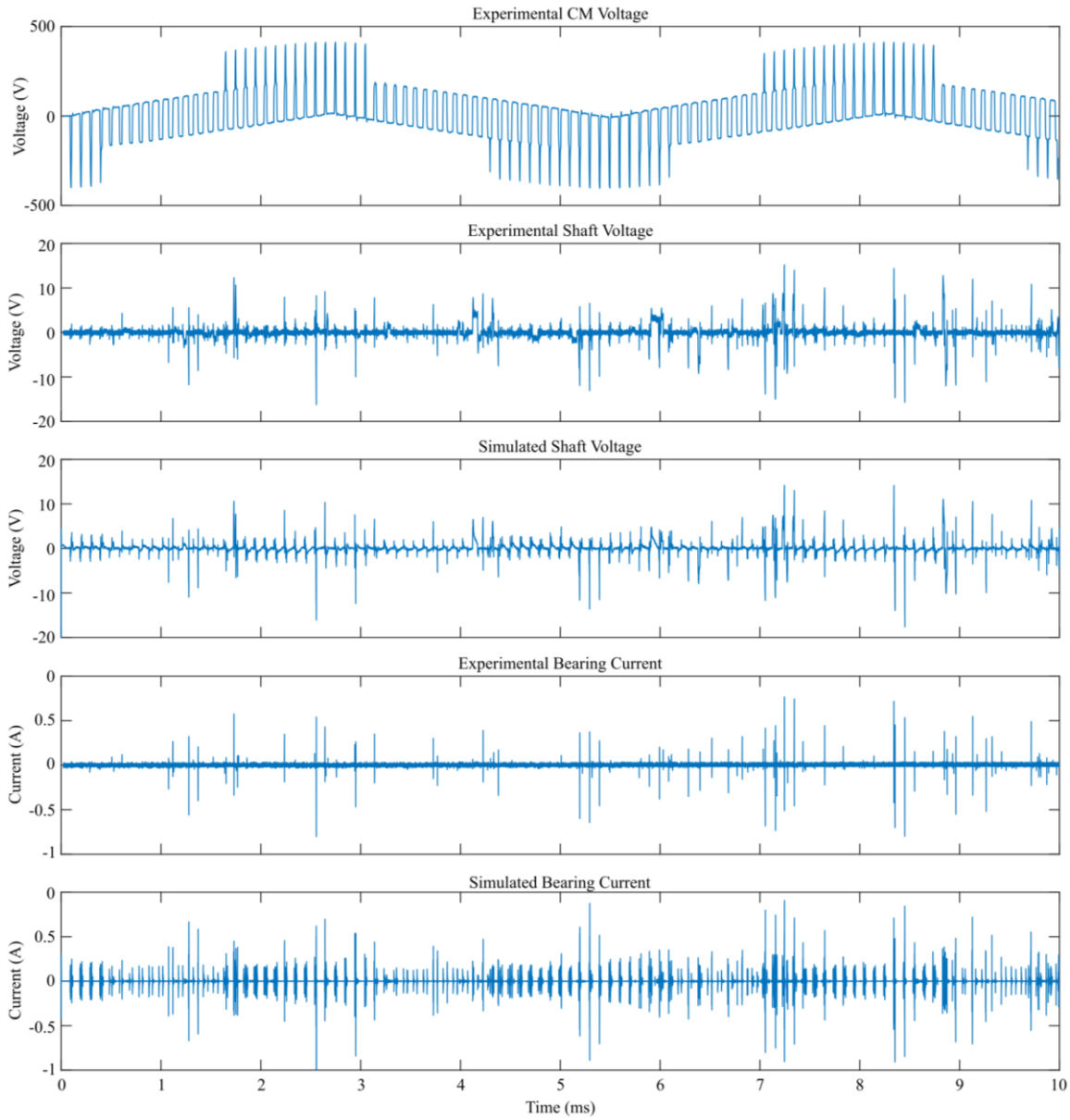

Figure 3.19. Experimental CM voltage, shaft voltage, and bearing current on the modified IM compared to Simulink model simulation results.

Overall, the simulation results show a good match with the experimental measurements. A tradeoff had to be taken when selecting the controller gains to calculate the bearing resistance of Fig. 3.18. To capture the high frequency transients of the shaft voltage and the bearing current, the proportional gain needed to be set high. This enabled an accurate simulation in the event of a discharge where the bearing resistance immediately

collapses. On the other hand, too high of a proportional gain causes saturation of the bearing resistance, which results in the bearing resistance switching back and forth between the upper saturation limit (in this case 1 MΩ) and the smallest possible resistance (1 Ω). This resulted in the bearing resistance being 1 MΩ when the error was positive and 1 Ω when the error was negative in order to drive the simulated shaft voltage to the experimental shaft voltage as quickly as possible. Unfortunately, a saturated bearing resistance switching back and forth between the saturation limits does not describe the physical reality of the bearing resistance. Therefore, a tradeoff was made between precisely capturing the high frequency EDM transients and realistically computing the bearing resistance. For the model shown in Fig. 3.18, the controller used is a proportional controller, where PID gains selected were 100, 0, and 0 for the proportional, integral, and derivative gains respectively. The resulting bearing resistance from the simulation results of Fig. 3.19 are shown in Fig. 3.20.

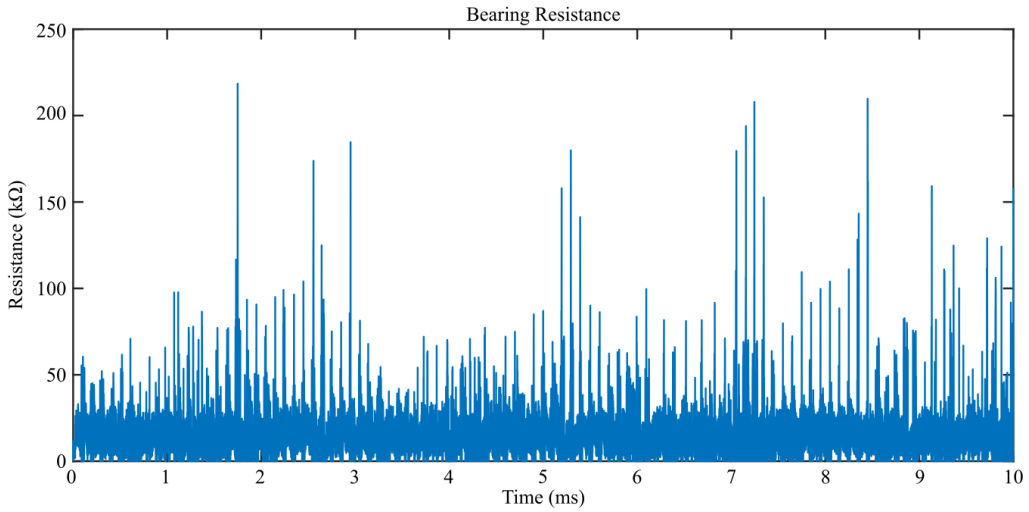

Figure 3.20. Computed bearing resistance for the simulation results of Fig. 3.19 on the modified IM.

From Fig. 3.20, the bearing resistance typically ranges between 5-30 kΩ, but becomes lower during a shaft voltage discharge or higher when the shaft voltage is able to build up to a relatively large value. As mentioned previously, tradeoffs between transient accuracy and a reasonable bearing resistance were made when setting the controller gains to compute the bearing resistance. Because of this, there are many possible bearing resistances than can be computed that give reasonable simulation results based on the controller gains chosen in the model. For this reason, the bearing resistance computation is not definitive, but gives a general sense of how the value is changing dynamically over time. This model can also be useful when comparing the effects of different lubricants on EDM discharge activity. By holding the controller gains constant, comparisons of the bearing resistance can be made between lubricants relative to one another.

Conclusions

This chapter investigated the modeling of EDM bearing currents on a micro- and macroscopic level. Precise circuit modeling in PSpice circuit simulation software was performed to describe EDM bearing currents for several different discharge scenarios: a modified IM, an unmodified IM, and a bearing testbed. To extract the discharge parasitics, experimental tests were performed with a network analyzer and a function generator. Through circuit modeling and experimental measurements, it was determined that the discharge resistance varies between discharges in a range of 1-10 Ω due to the race, ball, and lubricant dynamics. Two parasitic components are introduced into the discharge when modifying a machine for EDM bearing current measurement: an isolation capacitance from the bearing insulating sleeve and an inductance from the measurement

wire. Simulation results showed that the isolation capacitance has negligible effects on the discharge profile. However, the measurement wire inductance used to measure bearing currents can significantly alter the discharge profile. This inductance causes a damped sinusoidal discharge, and alters the discharge frequency, apparent bearing current magnitude, and the time that the discharge transient takes to dissipate. The measurement wire inductance may play a key role in the severity of the damage that occurs at the discharge location, because of the rate of energy transfer. This will be considered further in Ch. 4. Therefore, it is expected that the unmodified machine's discharges will be more severe for the same energy level discharge as a modified machine. Comparing the modified and unmodified motor discharge transients showed that a ratio of 0.2 described the difference between the peak bearing current in a modified machine and an unmodified machine (i.e., the peak bearing current is 5x greater in the unmodified machine), and that the unmodified machine discharge transients lasted ~17 ns while the modified machine discharge transients lasted ~600 ns. EDM bearing current transients on the Bearing Testbed lasted ~1200 ns. A higher machine level modeling approach was also taken which included the inverter CM voltage. The results of the model demonstrated how the CM voltage produces a voltage on the shaft through capacitive coupling, and how the bearing resistance collapses during a shaft voltage discharge. It is estimated that the dynamic bearing resistance is typically 5-30 kΩ, but becomes much lower during a discharge event and can be much higher during a large amplitude shaft voltage event.

CHAPTER FOUR

Finite Element Model of Bearing Discharge With Imaging Validation

A finite element model was developed to investigate the mechanical damage that occurs on the race surface during an EDM discharge. This chapter focuses on the impact of the electrical discharge on the mechanical EDM damage that it produces on the bearing ball and race surfaces, including the influence of the measurement wire inductance, and how the damping phenomenon produced by its presence affects the size of the damage spot on the race surface. Additionally, the model was used in conjunction with experimental results to determine the discharge energy threshold that produces damage on the race and ball surfaces. The size of the EDM damage spot is compared for various discharge amplitudes, and a statistical approach is taken to evaluate the EDM damage spots experimentally. Experimental results are compared with FE model results to validate the developed FE model. This chapter is further developed from results presented in [65].

Finite Element Model of Bearing Discharge

An advanced 4D FE model including time evolution of the electrical discharge transients was developed in COMSOL Multiphysics to investigate the damage that electrical discharges have on bearing ball and race surfaces. The developed model, in conjunction with experimental work and validation, enables various scenarios to be solved computationally and provides a method for determining the threshold discharge energy that causes damage to the bearing race and ball surfaces. Once validated experimentally, the

FE model provides an efficient tool for investigating the different parameters that influence EDM activity in a bearing, such as lubricant properties, discharge gap distance, and ball and race materials.

FE Model Development

The geometric design of the model contains two rectangles with a small gap in between. The top rectangle acts as the bearing ball, while the bottom rectangle is the bearing outer race. The gap in between the two rectangles is the thin lubricant layer where the discharge takes place. This geometry is then rotated axially 360° to develop a 3D model with radial symmetry. The lubricant layer thickness ranges from 0.3-0.5 μm, which is a typical range for lubricant film thicknesses for bearings running between 1500-2000rpm, as shown in Fig. 4.1 [66]. The discharge region is ~ 0.8 μm in diameter. This value was chosen because the literature has reported bearing race surface pits with a diameter of 0.5-1 μm [20]. Although the bearing race and ball are curved surfaces, the flat surface of the FE model is a valid approximation because of the small scale of the discharge diameter compared to the bearing ball diameter.

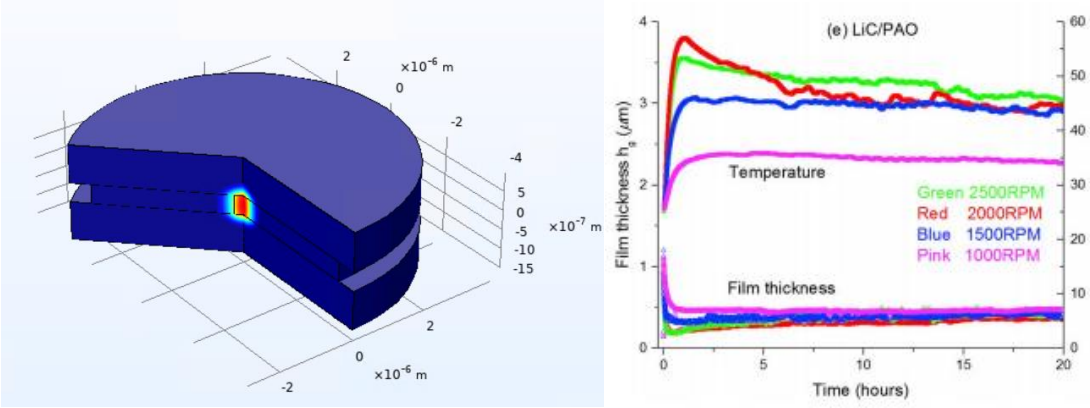

(a) (b)

Figure. 4.1. (a) 3D model of bearing discharge and (b) experimental film thickness of grease in a ball bearing [66].

To understand what happens to the localized bearing steel around the discharge area, the model employed an evenly distributed heat source in the discharge area which was a result of the electrical discharge through the grease converting to heat, with the heat then transferring into the bearing steel. This is implemented using the heat transfer for fluids and solids physics within COMSOL, which allows the grease/steel interface to function properly. The discharge voltage and current transients from the discharge circuit modeling of Ch. 3 were used to calculate the instantaneous power to be applied to the discharge area at any instant in time. Integration of this instantaneous power gives the energy of the discharge, as shown in Eq. (4.1).

$$E_{discharge} = \int_0^t p(t)dt \, , p(t) = i(t)v(t) \tag{4.1}$$

Here *p(t)* is the instantaneous power of the discharge, *v(t)* is the shaft discharge voltage and *i(t)* is the actual bearing current, not to be confused with the apparent bearing current that can be measured experimentally. This reveals the importance of a highly accurate discharge circuit model. The discharge models of Ch. 3 allow for computation of

the actual bearing current from the apparent bearing current. Since the actual bearing current is what damages the ball and race surfaces, this is the current necessary to calculate an accurate discharge energy for the FE model. Figure 4.2 shows the shape of the instantaneous power dissipation through the bearing for a 10V shaft voltage discharge on modified and unmodified IMs, as determined using models developed in PSpice, with the inset plot showing the 0-10 ns region magnified to emphasize the differences between the two, where the measurement wire inductance causes a damping effect and follow-on oscillations in the discharge current.

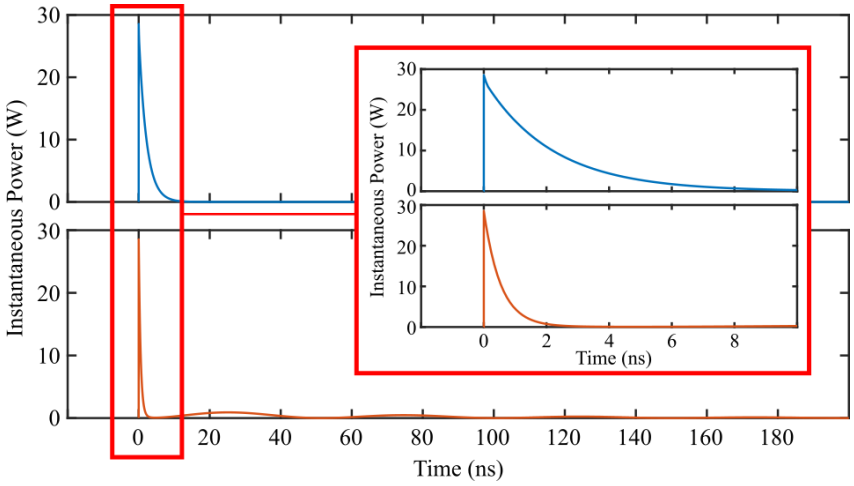

Figure 4.2. Instantaneous power dissipation in the bearing gap for unmodified IM (blue) and modified IM (orange).

Although the two discharges of Fig. 4.2 have the same energy, the modified machine's energy dissipation for any particular discharge is spread out further over time due to oscillations from the measurement wire inductance. Discharges on the unmodified motor dissipate more energy in a shorter amount of time, therefore it is proposed that discharges on the unmodified motor are more damaging than on the modified motor. Since the grounding wire alters the discharge phenomenon, an accurate FE model describing a

modified motor is of vital importance in determining the electric discharge machining (EDM) damage that results from discharges in an unmodified motor.

An ambient temperature of 40°C is used for the model initial conditions, with the boundaries fixed at ambient. Pyrolysis of the grease is simulated as an irreversible phase change in the grease: once the grease reaches 300°C [67], the fluid consumes 1.7MJ/kg of energy [68] to produce carbon black. The COMSOL model properties are summarized in Table 4.1.

Table 4.1. Heat transfer properties employed in the FE model.

Model Component	Description	Value	Unit
Steel	Heat Capacity	475	J/kgK
	Density	7850	kg/m^3
	Thermal Conductivity	46.6	W/mK
Grease	Heat Capacity	2000	J/kgK
	Density	0.86	g/mL
	Thermal Conductivity	0.2	W/mK
Carbon Black	Heat Capacity	710	J/kgK
	Density	2	g/cm^3
	Thermal Conductivity	710	W/mK

Acquisition of Model Data

To monitor the calculated temperature of the bearing in the FEM, temperature probes are placed at 20 locations on the bearing as shown in Fig. 4.3: one at the center axis and 0.02 µm inside the steel domain (i.e., above the grease/ball interface), ten in the parallel direction of the grease/ball interface at a spacing of 0.2 µm to measure the breadth of the discharge, and ten along the center axis with a spacing of 0.1 µm to measure the depth. These probes were placed to determine how deep into the bearing steel the temperature exceeds the steel's solidus temperature, which is 1350°C for the bearings considered in this research.

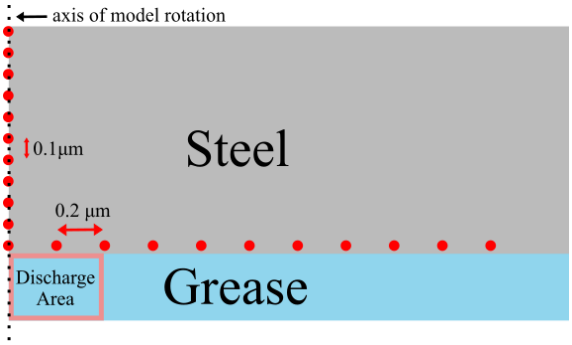

Fig. 4.3. Diagram displaying the location of the heat indicator probes.

Results

This section highlights the results of the FE model and demonstrates how various experiments were carried out on the bearing testbed to validate the model.

Experimental Evidence

To validate the FE model, the bearing testbed was employed because precise control of the discharge amplitude (energy) is possible, where the discharges occurring on the motor testbed are variable in nature, following a distribution (Ch. 5). It was hypothesized that the heat dissipation into the bearing steel is proportional to the discharge amplitude, since a larger amplitude contains more energy. Therefore, a larger amplitude of discharge would cause more damage to the bearing, and if the discharge energy is low enough, no damage would occur. To test this hypothesis, 8 experiments were carried out, where each experiment had a different discharge amplitude. The number of discharges were recorded, and the bearings were cut open for inspection upon experiment completion. A summary of the experiments performed along with the damage result is shown in Table 4.2. The shaft voltage and bearing current amplitudes of column 1 are similar to the amplitudes found on an electric machine, that is the ratio of peak bearing current to shaft

discharge voltage is the same. To select the discharge amplitudes of Table 4.2, the FEM was used in tandem with an experimental bisection method and engineering intuition. After completing a few of the experiments, it became clear that damage could be detected on the ball and race surfaces of the bearings with fewer discharges. This explains why each discharge amplitude test doesn't have an equal number of discharges. Upon experiment completion, the bearings were cut open and prepared for imaging with an Olympus LEXT OLS5100 laser microscope. A damage scale was developed to characterize the intensity of the EDM damage on the surface of the bearing races, as seen in Table 4.2. Images of the frosted region of the outer bearing races are shown in Fig. 4.4 using the microscope's 5x objective.

Table 4.2 Summary of discharge energy threshold levels for EDM damage experiments.

Experiment	Energy/Discharge	# of Discharges	Damage
17 V, 700 mA	316 nJ	12,983,774,249	*****
16 V, 650 mA	280 nJ	11,057,372,599	*****
10 V, 400 mA	110 nJ	5,394,301,756	****
7.5 V, 300 mA	62 nJ	7,396,457,952	****
6 V, 240 mA	40 nJ	10,511,137,690	***
5.5 V, 220 mA	34 nJ	6,124,563,786	**
5 V, 180 mA	27 nJ	4,268,783,089	**
4 V, 125 mA	17 nJ	7,970,709,414	*

***** significant frosting on race surface, pits and pillars visible

**** frosting on the race surface, pits and pillars visible

*** slight frosting on the race surface, pits and pillars visible

** very light frosting on race surface, difficult to detect with human eye

* no frosting or EDM damage detected, even with microscope

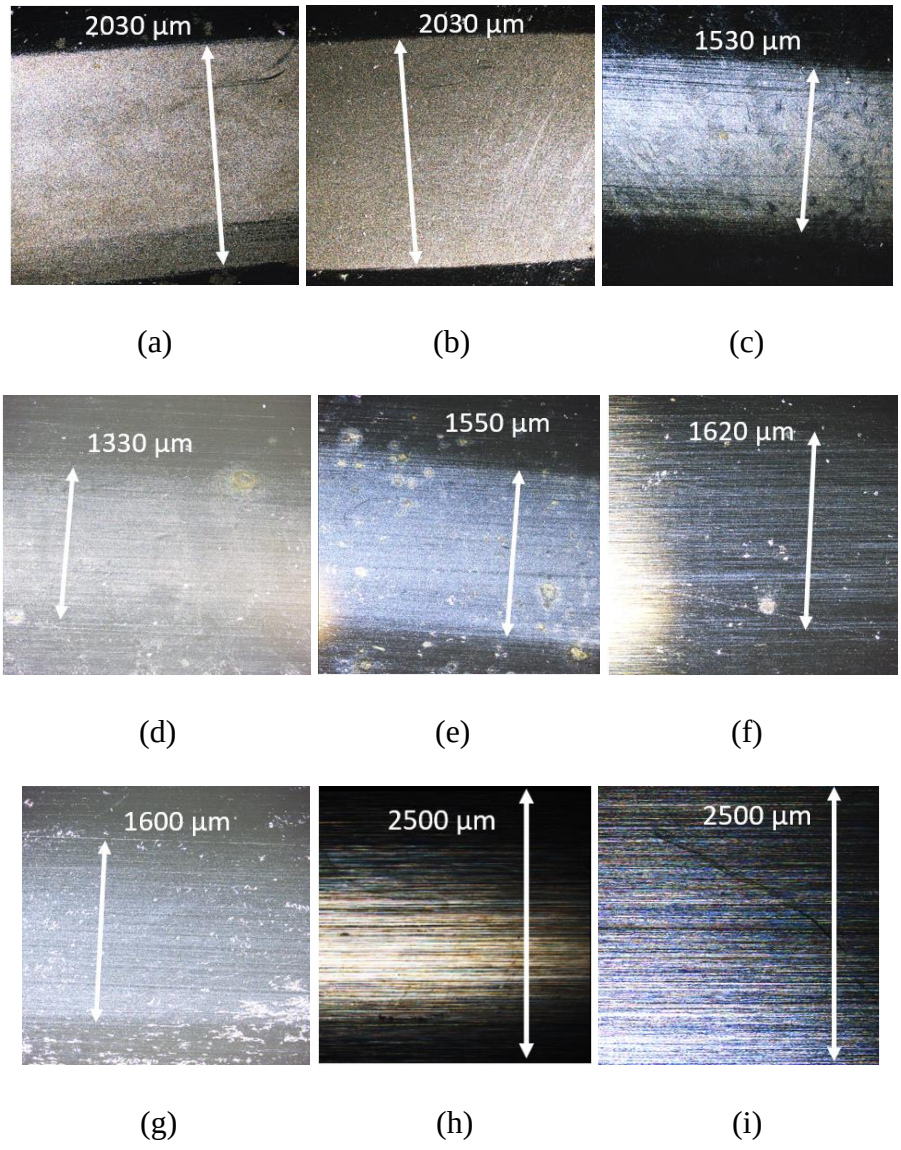

Figure. 4.4. Laser microscope images from experiments of Table 4.2 at 5x magnification. (a) 17V, 700mA (b) 16V, 650mA (c) 10V, 400mA (d) 7.5V, 300mA (e) 6V, 240mA (f) 5.5V, 220mA (g) 5V, 180mA (h) 4V, 125mA (i) new undamaged bearing.

From Table 4.2 and Fig. 4.4, the experimental threshold for an EDM discharge to create damage to the steel of the race and balls is between 4-5 V, which corresponds to discharge energies between 17-27 nJ. Below 17 nJ, the energy of the discharge does not cause EDM damage to the steel of the balls or races. The frosting region is due to most of the discharges occurring in a local area, however, individual discharge damage could be

seen outside of the frosting regions, although the occurrence of this is rare. For images a-g, the arrows display the width of the frosting region, while for images h and i the arrows are shown to give perspective on the size of the image since there is no frosting damage. There are a few other defects to note on the images of Fig. 4.4. To cut the bearings open for imaging a water-injected diamond saw was used. Since water encountered the bearing, small oxidation patches occasionally occurred on the same surfaces that were imaged. These marks are much larger in diameter than the EDM damage spots and are composed of various colors in the image due to the microscope laser. These oxidation marks can especially be seen in Fig. 4.4(d, e, f). Additionally, the bearings contain some microdefects from the manufacturing process. Imaging results displayed occasional scratches, scuffs, and small defects to the race surface, such as the scratch that is ~30° rotated clockwise from the polishing lines in Fig. 4.4(f) and the white blotches that can be seen in the lower right corner of Fig. 4.4(g). Similar defects can also be seen on brand new bearings, and bearings that have been spun without electrical discharges, as seen in Fig. 4.5. However, these defects are much different in appearance than EDM damage spots and frosting, as will be shown in the next section.

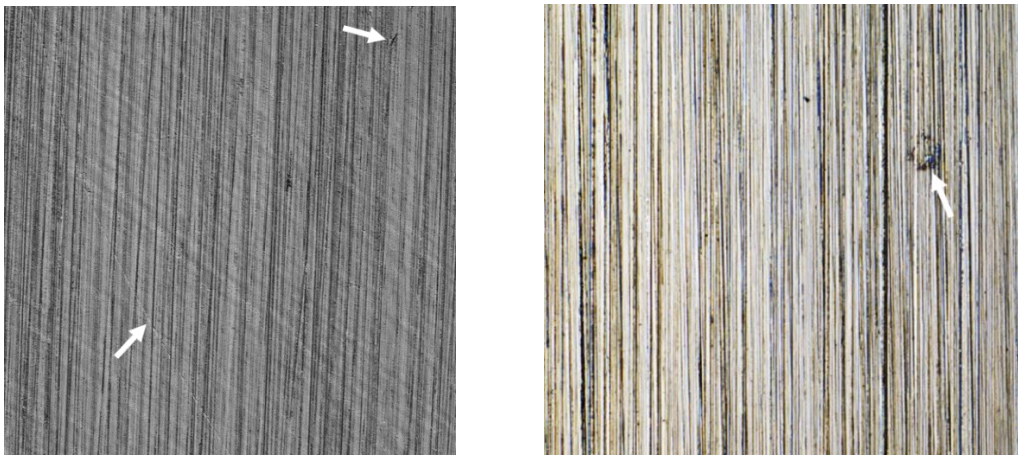

(a) (b)

Fig. 4.5. Microdefects can be seen on the bearing race surface for (a) new bearings that have not been spun and (b) new bearings that have been spun for two weeks without EDM activity.

FE Model Results

Various bearing testbed PSpice discharge amplitudes were fed into the FE Model to determine the discharge energy threshold that exceeds the solidus temperature of the steel, resulting in EDM damage on the ball and race surfaces. Various amplitudes were swept, and the steel temperature was plotted spatially along the steel-grease interface as shown in Fig. 4.6, and plotted against the depth into the steel, as can be seen in Fig. 4.7.

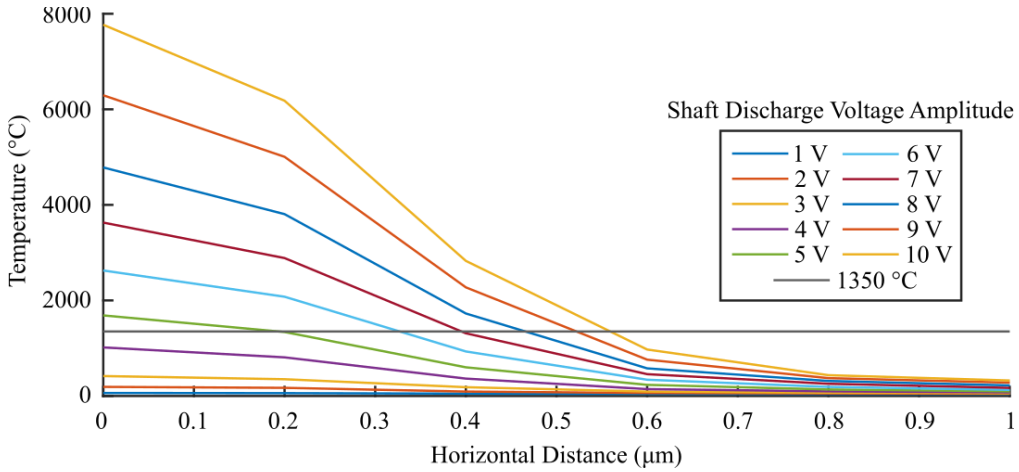

Fig. 4.6. Temperature along the surface of the bearing steel for various discharge amplitudes. The discharge is centered at the point x = 0.

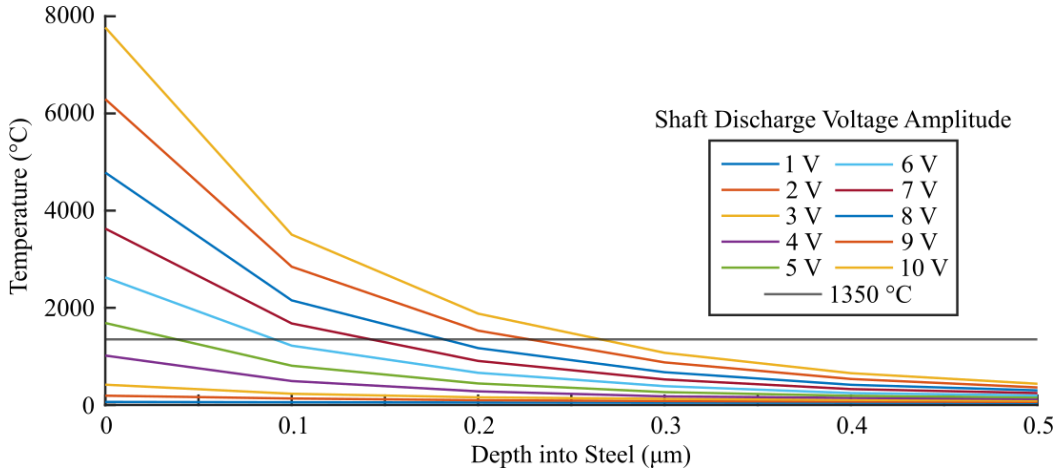

Figure 4.7. Temperature into the bearing steel for various discharge amplitudes. The surface of the steel on the plot is at the point x = 0.

From the plots of Figs. 4.6 and 4.7, the temperature of the steel exceeds the solidus temperature when a 5 V shaft discharge occurs, but not when a 4 V shaft discharge occurs. The green line labeled 5 V gives a maximum temperature just above the solidus temperature of the steel at the center of the model (0 μm from the center), whereas the purple line labeled 4 V is just below the solidus temperature. Linearly interpolating between these two values to determine the shaft discharge voltage that results in bearing

damage yields a calculated value of 4.6 V, which lies between the lowest voltage tested experimentally that showed damage (5 V) and the highest voltage that did not show damage (4 V). Therefore, the threshold for EDM damage is between 4-5 V, which agrees with the experimental results of the previous section. Given that an EDM damage spot is only generated on the ball and race surfaces when the local steel exceeds the solidus temperature, the intersection of the solidus temperature with the voltage curves of Figs. 4.6 and 4.7 gives the approximate EDM damage spot radius and depth into the steel.

Therefore, the accuracy of the FE model is validated experimentally, and can be used to make predictions about the damage that is occurring inside of a bearing for scenarios that are difficult to be evaluated experimentally, including accurately determining the damage to a bearing for the various shaft discharge voltages produced by PWM inverters.

Statistical Analysis of EDM Pits and Pillars

To test the hypothesis of EDM damage spot size being proportional to the discharge energy, various measurements were performed on the eight experiments with the Olympus LEXT OLS5100 laser microscope. Since the frosted regions contain a high density of discharge damage, it is difficult to make a measurement in this region, due to the discharge damage overlapping or multiple discharges occurring in the same exact location. For this reason, measurements were taken on the edges of the frosted regions. This provided a high density of EDM damage spots, yet not high enough of a density to cause overlapping of damage spots, which in turn would corrupt the measurement. Of particular interest in measuring the EDM damage spots is the diameter and depth of the damage spot because this information can be directly compared to the FE model results of Figs. 4.6 and 4.7.

However, results for the depth of the EDM damage spots proved difficult to obtain and find any statistical trends for a couple of reasons. First, when the local steel melts due to an EDM discharge it hypothesized from the FE model that re-solidification occurs within tens of ns, depending on the amplitude of the discharge. During this time, the liquid steel can move freely within the local area of the discharge. In the case of a micropit, the liquid steel moves out of the melted area, and in the case of a micropillar additional steel is added to the location, perhaps from the bearing ball if the micropillar were located on the bearing race. Between these two extremes, the liquid steel can distribute in an infinite number of ways at various locations. In this research, the bearing outer races were primarily imaged, and it was found that mircopillars are the primary form of damage on the outer race. It is hypothesized that this may be due to centrifugal forces within the bearing depositing small amounts of liquid steel from the ball to the race. Second, the curves of the bearing race surfaces make imaging with high zoom objectives difficult. Micro- pits and pillars were imaged with the LEXT 5100's 50x long objective at a working distance of ~10 mm, which provides great information about the diameter of the damage area, but isn't quite enough resolution to get highly accurate height and depth measurements. Moving up to the next objective, 100x, requires a working distance of 0.3 mm, which is too close for the curvature of the bearing races. Therefore, the focus of the imaging was placed on the EDM damage spot diameters.

An imaging procedure was developed, which consisted of 50 EDM damage spot diameter measurements for each of the eight bearing experiments of Table 4.2. An example of a bearing race image for the 17 V discharge race is shown in Fig. 4.8(a), with a bearing race with no electrical damage shown in Fig. 4.8(b) for comparison.

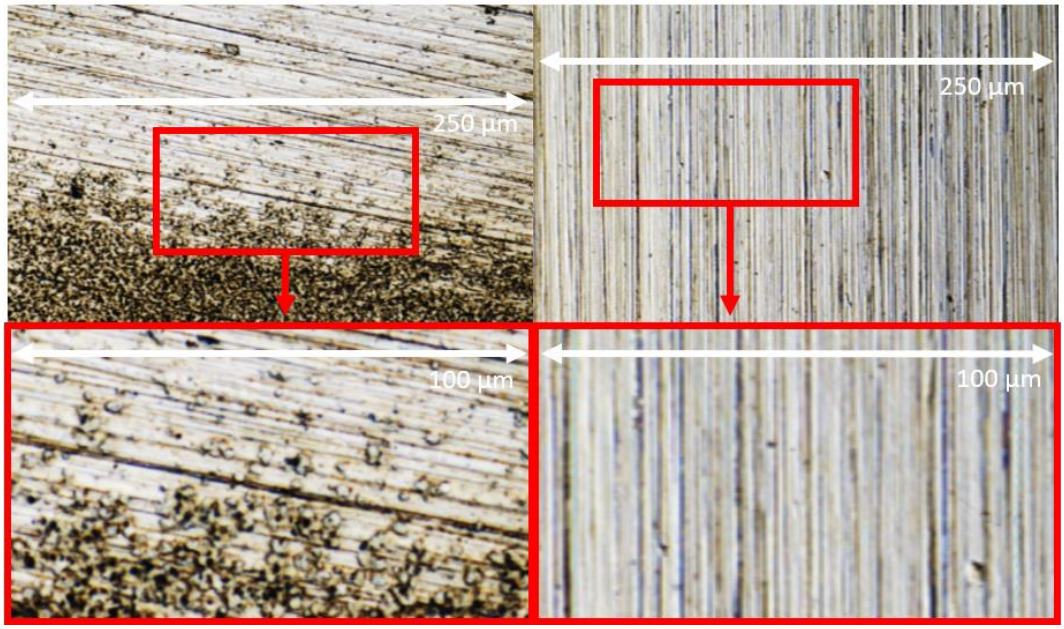

(a) (b)

Figure. 4.8. (a) 17 V discharge damage on edge of frosted region and (b) an undamaged bearing that was spun for two weeks without any EDM activity.

Using the spatial points of Fig. 4.6 where the steel temperature for each discharge voltage intersects the steel's solidus temperature, the FE model results for the predicted diameter of the EDM damage spot can be compared with the statistics acquired from imaging, as shown in Fig. 4.9. Each box and whisker plot of Fig. 4.9 indicates 50 imaging samples at each discharge voltage amplitude.

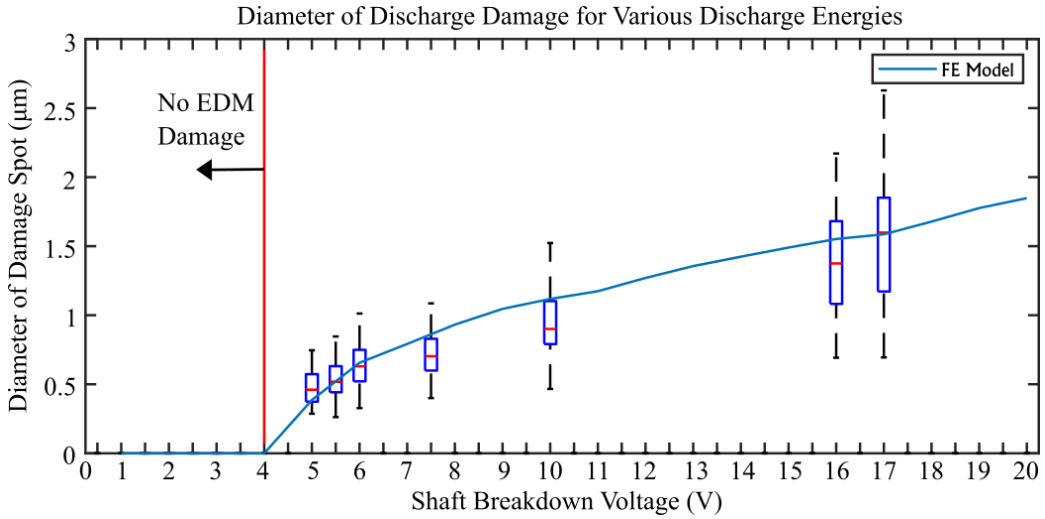

Figure. 4.9. Box and whisker plots denote the imaging statistical results for each discharge voltage value. The FE model results for the EDM damage diameter for a specific discharge voltage are overlain for comparison.

The imaging statistics are compared with the FE Model numerically in Table 4.3. The box and whisker statistical representation was chosen because it visually demonstrates how the imaging diameter data distribution compares to the FE Model results. In Table 4.3., UQ is the upper quartile, LQ is the lower quartile, IQR is the inner quartile range, and the percent error is computed between the imaging diameter mean and the FE model diameter result.

Table 4.3. Comparison between imaging statistics and FE model results.

Experiment	Imaging Diameter (µm)					FE Model Diameter (µm)	Percent Error (%)
	Median	Mean	UQ	LQ	IQR		
17 V, 700 mA	1.599	1.522	1.851	1.172	0.679	1.586	-4.0
16 V, 650 mA	1.375	1.389	1.681	1.082	0.599	1.552	-10.5
10 V, 400 mA	0.901	0.933	1.102	0.791	0.311	1.118	-16.5
7.5 V, 300 mA	0.703	0.709	0.829	0.599	0.230	0.862	-17.7
6 V, 240 mA	0.630	0.631	0.749	0.521	0.228	0.656	-3.8
5.5 V, 220 mA	0.518	0.533	0.631	0.442	0.189	0.521	2.3
5 V, 180 mA	0.465	0.472	0.573	0.374	0.199	0.386	22.2
4 V, 125 mA	-	-	-	-	-	-	-

Overall, the FE model shows a good comparison with the imaging results, validating the developed FE model. The error that does exist can be explained by a few factors. One key factor is that it was assumed that the EDM damage spots are perfect circles when being measured, when in reality they can appear in various shapes and sizes. To mitigate this error when imaging, the diameter chosen to measure was randomized by the operator as able, which should effectively cancel out this error effect with a large sample size. However, this error most likely cannot be completely eliminated due to operator bias, and therefore may contribute to the discrepancy between the imaging and FE model results. Another source of error is the assumption made of a constant discharge resistance and gap between the ball and bearing race in the FE model, when these value changes dynamically with bearing operation. As will be demonstrated in Ch. 5., the discharge resistance (and in turn the ball-race gap) follows a distribution across discharges, which will alter the rate of energy dissipation into the steel, affecting the size of the EDM damage spot. This phenomenon is demonstrated in the next section of this chapter with the FE model. Considering these potential sources of error, the percent error statistic of Table 4.3 validates the FE model.

Effect of Measurement Wire Inductance

With the FE model now validated with experimental results, the model can be used to answer other research questions, such as the effect of the measurement wire inductance on the EDM damage area. To do this, 20 V discharges on the modified and unmodified IM are investigated. The results are seen in Fig. 4.10.

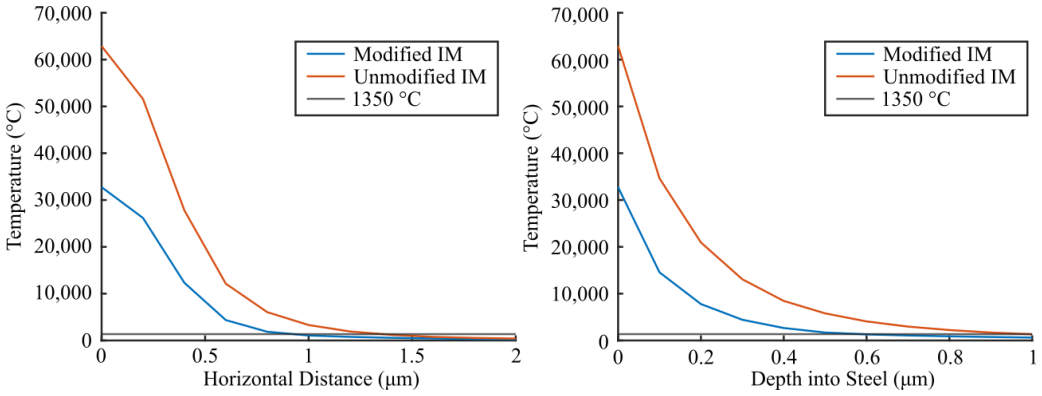

Figure 4.10. A 20 V discharge simulated on the FE model for the modified and unmodified IM.

Here, the measurement wire inductance of the modified machine dampens the rate of energy transfer into the discharge gap, which results in less heat propagating through the steel, which in turn results in less damage than the unmodified machine. The FE model predicts that a 20 V discharge will cause an EDM damage spot with a radius (diameter) of ~1.25 μm (~2.5 μm) and a depth of ~ 1μm for the unmodified motor and an EDM damage spot with a radius (diameter) of ~0.92 μm (~1.84 μm) and a depth of ~0.6 μm for the modified motor. Thus, the EDM damage spots are expected to be smaller for the modified machine compared to the unmodified machine for the same discharge energy. With an increase in the measurement wire inductance, it can be expected that the rate of energy dissipation into the bearing steel will continue to decrease.

Conclusions

This chapter presented the development of an advanced 4D finite element model to evaluate the mechanical damage that occurs due to EDM discharges inside a bearing. The FE model results were validated statistically with experimental evidence from various bearings, and it was found that the FE model could even predict the threshold

discharge energy that creates damage on the bearing ball and race surfaces. In addition, the results of the FE model and the PSpice discharge circuit modeling of Ch. 3 reveal that an impedance such as the measurement wire inductance placed in series with the EDM discharge can dampen the rate of energy dissipation in the gap. The slower rate of energy dissipation means that heat generated by the discharge has more time to propagate through the metal, which in turn means that the localized temperature will not build up to as a high of a value than it would if the series impedance was not there. Adding an additional impedance into the discharge path may be an effective solution for prolonging bearing lifetime.

CHAPTER FIVE

Characterization of Shaft Voltages and EDM Bearing Currents due to Si- and SiC-based PWM Inverters

This chapter provides a statistical analysis of shaft breakdown voltages and EDM bearing currents inside of PWM inverter-driven machines. The causes and contributing factors of the variation in EDM discharge amplitudes are explored, and special emphasis is placed on comparing inverters comprised of Si and SiC semiconductor devices. Distribution functions are fit to experimentally collected data that effectively demonstrates the effects of the bearing temperature and load.

Bearing EDM Amplitude

Due to the permissible switching states of the TLSS inverter, the resulting CM voltage appears as discrete values of the DC bus, where the possible values are -V_d, -1/3V_d, +1/3V_d, +V_d. By employing the machine BVR (Eq. 1.7), the shaft voltage is then:

$$V_{shaft} = \frac{C_{sr}}{C_{sr}+C_{rf}+2C_b} V_{CM} \tag{5.1}$$

From this it follows that the shaft voltages generated by the CM voltage will also appear in discrete levels, voltages of which are reduced by the ratio of the machine parasitic capacitances. It would then be expected that the shaft discharge voltage along with the EDM bearing current amplitude would have four discrete levels, two of which are equal and opposite in amplitude to the remaining two. However, in practice, the CM voltage and machine shaft voltages do not follow these discrete amplitude levels. To understand this, a framework reaching beyond the BVR theory is required.

Three-Phase Rectifier CM Voltage

When a nonlinear load is applied to a power system, additional voltage and current harmonics will be generated in the system. The Si and SiC three-phase motor drive power electronic systems considered in this research employ a three-phase diode rectifier on the front end of the motor drive systems to produce the necessary dc bus voltage for the inverter. A circuit diagram of the three-phase rectifier can be seen in Fig. 5.1, where the three-phase voltage source input is defined as follows:

$$v_a = \sqrt{2}\mathrm{V}\sin(wt) \tag{5.2}$$

$$v_b = \sqrt{2}\mathrm{V}\sin(wt - 120°) \tag{5.3}$$

$$v_b = \sqrt{2}V\sin(wt + 120°) \tag{5.4}$$

For the three-phase system considered in this research, *V* is the rms amplitude of the phase voltages, in this case 277 V, and *w* is the angular frequency where the grid frequency is 60 Hz.

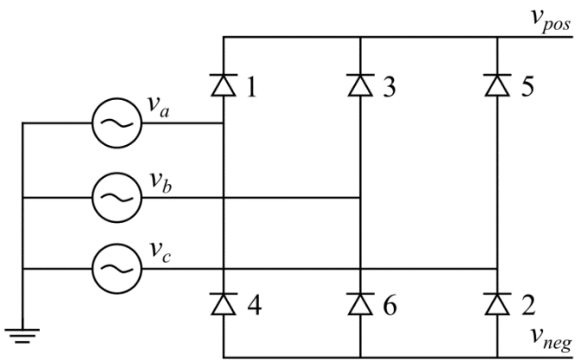

Figure 5.1. Three-phase ac/dc diode rectifier.

The three-phase diode rectifier, also known as a six-pulse bridge rectifier, selects portions of the source line-to-line voltage to synthesize a dc voltage, which is measured between v_{pos} and v_{neg}. The rectified dc voltage contains 6 pulses per system voltage period. Only

two diodes conduct at any one time, the diode conduction pairs being 1-2, 3-4, 5-6.

Being a nonlinear load, the three-phase diode rectifier produces a CM voltage as follows:

$$V_{CM} = \frac{v_{pos}+v_{neg}}{2} \tag{5.5}$$

A simulation was performed in MATLAB/Simulink to investigate the three-phase diode rectifier's CM voltage characteristics. A purely resistive load was connected between v_{pos} and v_{neg}. The results are shown in Fig. 5.2, where v_d is the dc voltage measured between v_{pos} and v_{neg}.

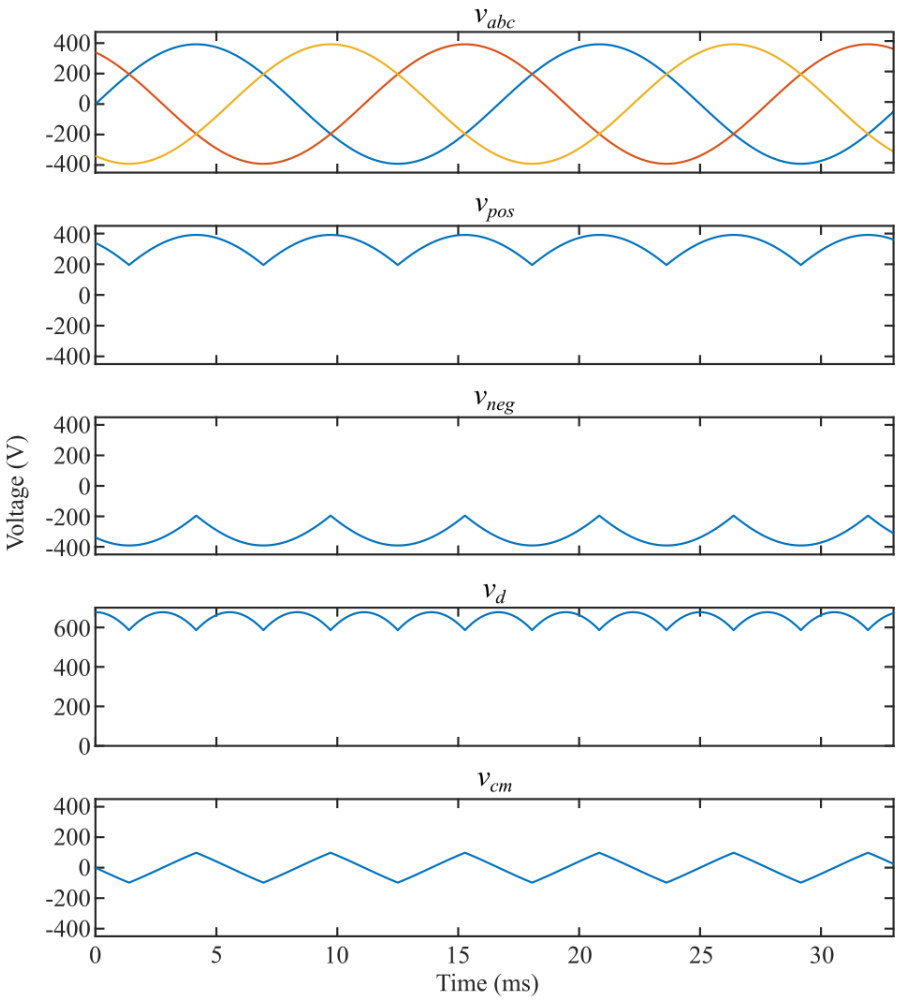

Figure 5.2. Two cycles of three-phase rectifier waveforms. From top to bottom: three phase input line voltages, positive terminal of dc bus to system ground, negative terminal of dc bus to system ground, dc bus voltage, three-phase rectifier CM voltage.

The rectifier's CM voltage is independent of the load resistance. The main component of the rectifier CM voltage is the 3rd harmonic of the power system frequency, for this system 180 Hz. The CM peak value is $\frac{\sqrt{2}}{4}V$ (97.93 V), which is 35% of the system line voltage. For capacitive loads, the CM voltage is reduced to 23% of the system line voltage [69]. To decompose the harmonics of the CM voltage for a resistive load, an FFT is provided in Fig. 5.3.

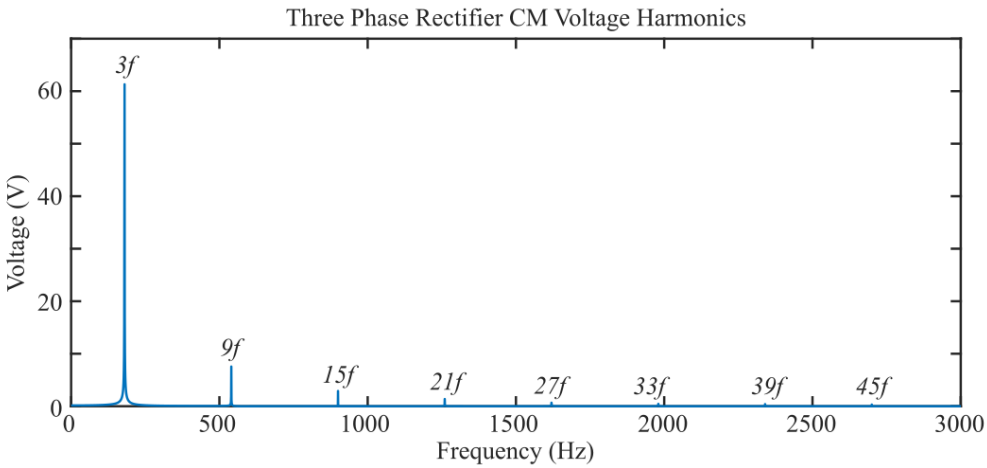

Figure 5.3. The three-phase six-pulse diode bridge rectifier produces a CM voltage that contains triplen harmonics.

From Fig. 5.3, the rectifier's CM voltage contains triplen harmonics of the power system fundamental frequency (n = 3, 9, 15, 21…..), with the 3rd harmonic being the primary component with the largest amplitude. Therefore, the power electronic system CM voltage present in the machine windings is a superposition of the CM voltages generated by the three-phase diode rectifier and the TLSS inverter.

$$V_{CM_{sys}} = V_{CM_{rectifier}} + V_{CM_{TLSS\ Inverter}} \tag{5.6}$$

Experimental measurements of the CM voltage of the motor drive system reveals the superposition of the rectifier and TLSS inverter CM voltages, as shown in Fig. 5.4.

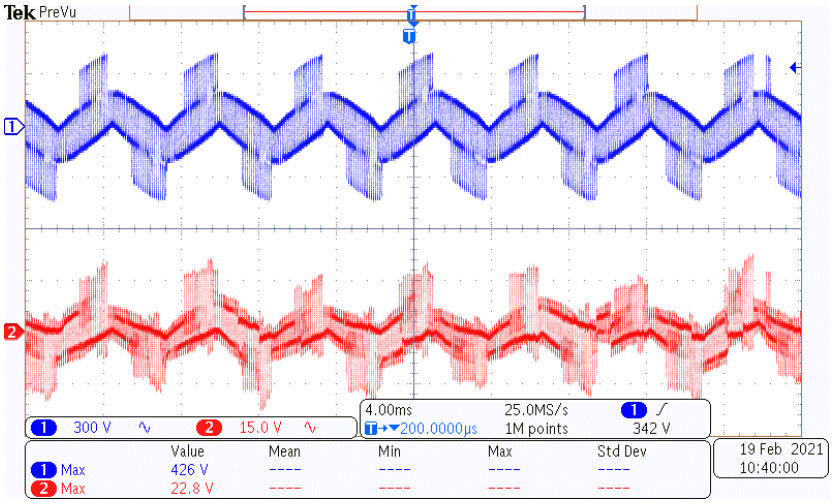

Figure 5.4. CM voltage (blue, 300 V/div) and shaft voltage (red, 15 V/div) of Toshiba IM with 20°C bearing temperature.

The amplitude of the CM voltage for both the Si and SiC drives are the same, due to the same DC bus voltage of ~675 V employed. Clearly from Fig. 5.4 the shaft voltage is a proportional fraction of the CM voltage due to the capacitive divider effect. From the max values of Fig. 5.4, The BVR for the Toshiba machine is 22.8/426 = 5.3 %. Close inspection of Fig. 5.4 shows the superposition of the TLSS inverter CM voltage and the three-phase rectifier CM voltage. At a 20°C bearing temperature, the shaft voltage follows the CM voltage closely according to the BVR because the bearing lubricant remains intact at this temperature (i.e., there is no dielectric breakdown of the lubricant). The strong 3rd harmonic of the rectifier CM voltage prevents the shaft voltage discharge and EDM bearing current amplitudes from having 4 discrete levels.

Bearing Operational Temperature

Although the BVR is dependent on the ratio between the capacitances of Eq. (1.7), as the bearing temperature increases the dielectric strength of the grease weakens (i.e., the lubricant film thins), allowing for breakdown of either the DE or NDE bearing

capacitance, which results in bearing current discharges at lower shaft voltages than the shaft voltage according to the BVR, as shown in Fig. 5.5, where typical bearing temperatures for 5 hp motors range from ~20-60°C for ~20°C ambient temperature.

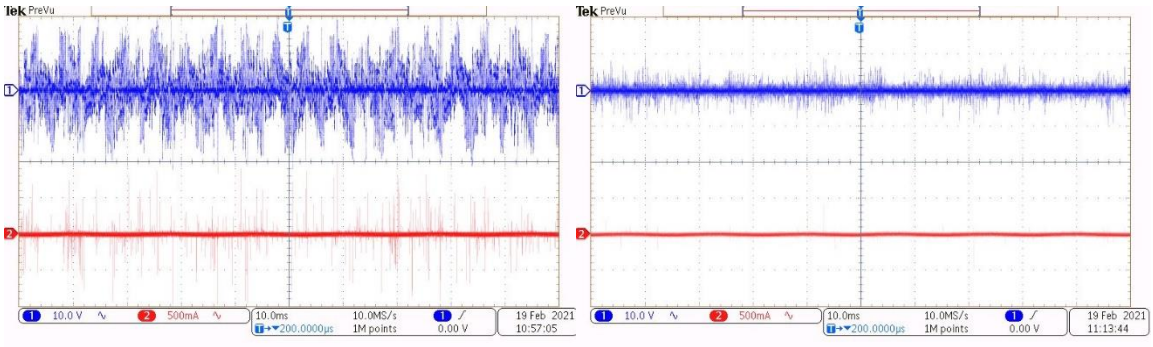

(a) (b)

Figure 5.5. Shaft voltage (blue, 10 V/div) and EDM bearing current (red, 500 mA/div) at (a) 35°C and (b) 50°C.

Since the energy stored electrostatically in the rotor assembly is dependent on the square of the shaft voltage ($E = \frac{1}{2}(C_{rf} + 2C_b){V_{shaft}}^2$), higher energy discharges occur at lower bearing operational temperatures due to an increase in the threshold voltage for dielectric breakdown. Consequently, operational temperature may play a significant role in bearing lifetime.

Bearing and Lubricant Dynamics

For any given motor operational point, shaft voltage and bearing current discharges vary in amplitude between discharges, as can be seen in Fig. 5.6.

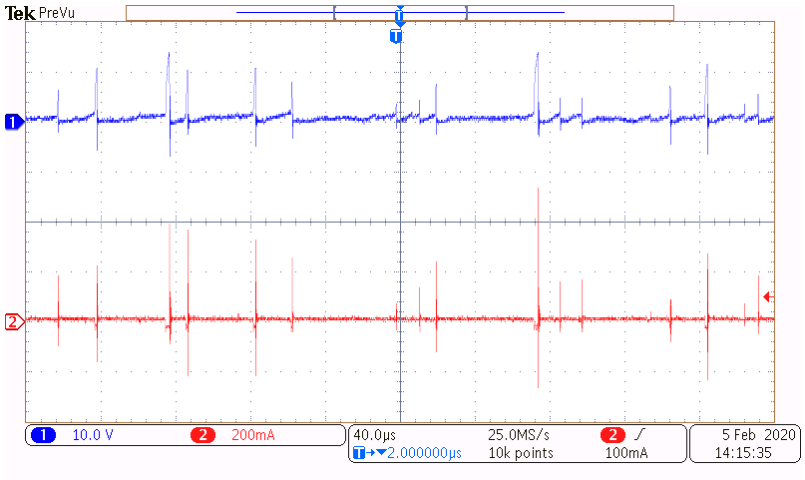

Figure 5.6. Shaft voltage (blue, 10 V/div) and bearing current (red, 200 mA/div) amplitudes vary in intensity.

This is due to the discrete discharge levels produced by the inverter CM voltage, the strong 3rd harmonic component of rectifier CM voltage, and is also due to asperity differences along the race and ball surfaces, as well as differences in grease thickness, which continuously changes the distance between the race and ball surfaces, leading to variable discharge amplitudes. In other words, the amplitude of any particular discharge depends on the instantaneous dynamic bearing resistance at the moment a change in the CM voltage occurs. If the dynamic bearing resistance dominates the bearing impedance at the time of a CM voltage edge event, the shaft is effectively connected to the frame of the machine, which is at ground potential. This results in the shaft being at ground potential and no shaft voltage can accumulate.

CM Voltage dv/dt Direction

Additionally, the sign of the slope of the successive CM voltage edges also impacts the shaft voltage and EDM bearing current discharge amplitude, as successive edges with the same dv/dt sign direction have the ability to build the shaft voltage up to

an even larger value, which produce the largest amplitude of discharges. In general, there are four primary ways in which the CM voltage produces voltages on the machine shaft, which can result in EDM discharges, as shown in Fig. 5.7. This is due to the four different levels of the DC bus that are permissible for the CM voltage: $-V_d$, $-1/3V_d$, $+1/3V_d$, $+V_d$ (Fig. 1.3). The edges of the CM voltage typically occur in groups of 4. This is due to the SVPWM switching algorithm that utilizes the two zero state vectors to efficiently switch back and forth between two inverter phase vectors. Details on the space vector switching algorithm can be seen in Ch. 2. Red markers are provided in Fig. 5.7 to show how the changing CM voltage is synchronized with a voltage beginning to build on the shaft.

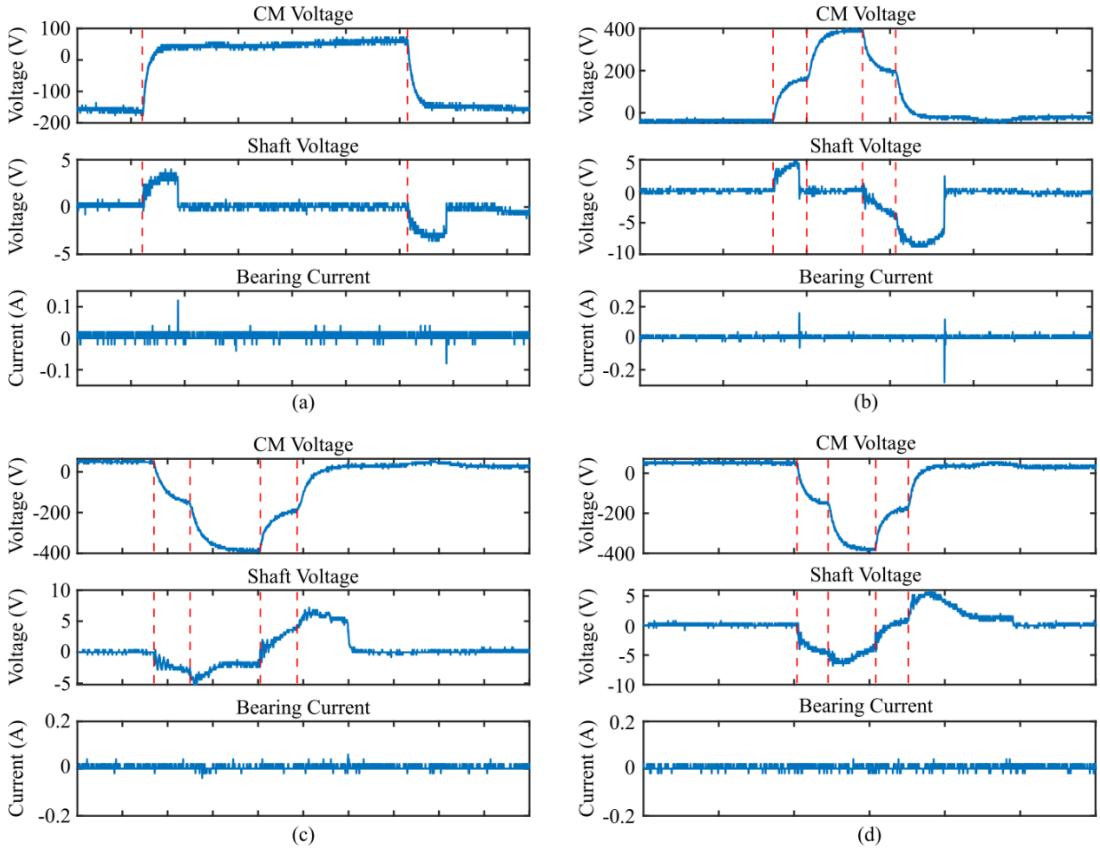

Figure 5.7. The four generic ways in which the CM voltage produces a shaft voltage, leading to an EDM bearing current event.

Discharge due to one CM voltage dv/dt event. From Fig 5.7(a), two discharge events are shown in which a single CM voltage change produces each. The capacitive coupling causes a voltage to begin building on the shaft when the CM voltage switches. Shortly after, the bearing lubricant breaks down, discharging the shaft. A spike in the bearing current can be seen at this time.

Discharge due to two CM voltage dv/dt events. In Fig. 5.7(b), another single CM voltage change event produces a discharge, as occurred in Fig. 5.7(a). After this, another CM voltage change produces no shaft voltage. This is most likely due to low capacitive coupling during this time frame (i.e., the dynamic bearing resistance dominates the overall bearing impedance). However, after this, two additional CM voltage changes occur, this time in a negative direction. The first does not result in shaft voltage breakdown, therefore the second CM voltage change electrostatically builds in a negative direction upon the first, increasing the voltage in absolute value even further. A discharge then results in a larger bearing current amplitude due to the larger amount of energy stored electrostatically.

Discharge due to three CM voltage dv/dt events. In Fig. 5.7(c), a discharge is the result of three CM voltage changes. Notice that the second CM voltage change event does not "stick" onto the shaft as the others do. The third CM voltage change brings the shaft voltage back to a positive value, and then the fourth CM voltage change builds the shaft voltage even larger, which results in dielectric breakdown.

Discharge due to four CM voltage dv/dt events. From Fig. 5.7(d), all four of the CM voltage edges reflect onto the shaft, which result in a near zero shaft voltage since the two negatively sloped edges cancel out with the two positively sloped edges.

In summary, the shaft volage and bearing current discharge amplitude depends on how well the shaft voltage "sticks" which depends on the dynamic bearing resistance, which is dependent on temperature. The four generic ways in which a discharge occurs is due to one, two, or three CM voltage edges producing shaft voltages. When all four CM voltages produce a shaft voltage without breakdown, the shaft voltage may result in zero potential at the end of the four switching events, depending on the dynamic bearing resistance at the time of the CM voltage event. The examples provided in Fig. 5.7 are only examples of the generic cases, and any combination of CM voltages changes can result in a shaft voltage buildup and discharge. However, the CM voltage never changes in the same slope direction more than two times successively, so the shaft voltage will not build up larger than what is possible from two CM voltage change events.

This section highlighted the factors which affect shaft voltage and bearing current discharge amplitudes. Upon first inspection of the TLSS inverter BVR theory, one might expect that the shaft voltage and bearing current discharge amplitudes would occur at four different discrete levels, just as the inverter CM voltage takes on four discrete values of the DC bus. However, the three-phase rectifier on the front end of the motor drive system produces a CM voltage that has a strong 3rd harmonic at 180 Hz. This rectifier CM voltage is superimposed onto the TLSS inverter CM voltage, which means that the system CM voltage does not take on four discrete values of the DC bus, therefore the shaft voltage and bearing current discharge intensity also does not. Additionally, it was

demonstrated experimentally that the bearing lubricant temperature alters the discharge amplitude. Bearing and lubricant dynamics also play a significant role, as these influence the level of capacitive coupling onto the rotor assembly. Finally, it was demonstrated that shaft voltages can build on one another successively, which results in the largest shaft voltage and bearing current amplitudes.

EDM Characterization

From the previous section, several factors contribute to the variation in EDM discharge intensity. For an accurate lifetime prediction of motor bearings subject to EDM currents, it becomes necessary to understand in detail the potential discharge amplitudes that occur at any given motor operational point as well as how the discharge amplitudes change with motor variables such as operational temperature and load, because the discharge amplitude intensity is directly correlated to the lifetime of the bearing. To do this, a novel technique has been developed to characterize shaft voltage and EDM bearing currents for Si and SiC inverter motor drive systems. The two semiconductor technologies are compared, and EDM activity is characterized across machine temperature and loading. The results reveal which motor operational points are most dangerous for bearing lifetime, as well as the differences in EDM intensity between conventional (Si) and wide bandgap (SiC) devices in inverter-driven motors.

Experimental Procedure

To investigate the impact of Si and SiC device inverter switching speeds and frequencies on machine bearing EDM currents, an experimental procedure was developed for the testbed of Fig. 2.1. The bearings operate in a temperature range between ambient

(~20°C) and full machine loading (~60°C). At various operating points between 30°C & 60°C, 1000 ms of shaft voltage and EDM bearing current data were recorded on the modified IM. Once the data was collected, an algorithm was developed that iterates through each waveform and extracts the peak bearing current, as well as the shaft breakdown voltage that produced the bearing discharge. Only discharges with an amplitude greater than 50 mA were recorded to prevent current probe noise due to bearing displacement current from affecting the data. Additionally, discharges less than 50 mA most likely do not cause EDM damage to the race surface, and therefore do not affect bearing operational lifetime. Therefore, these small amplitude discharges can be disregarded. The developed algorithm to extract the shaft voltage and bearing current discharge amplitudes can be seen in Appendix E. All data was collected at a motor speed of 1800 RPM and a switching frequency of 10 kHz.

Experimental Results

The results from this experimental procedure are shown in Fig. 5.8, where the extracted data is displayed for both the Si and SiC inverter.

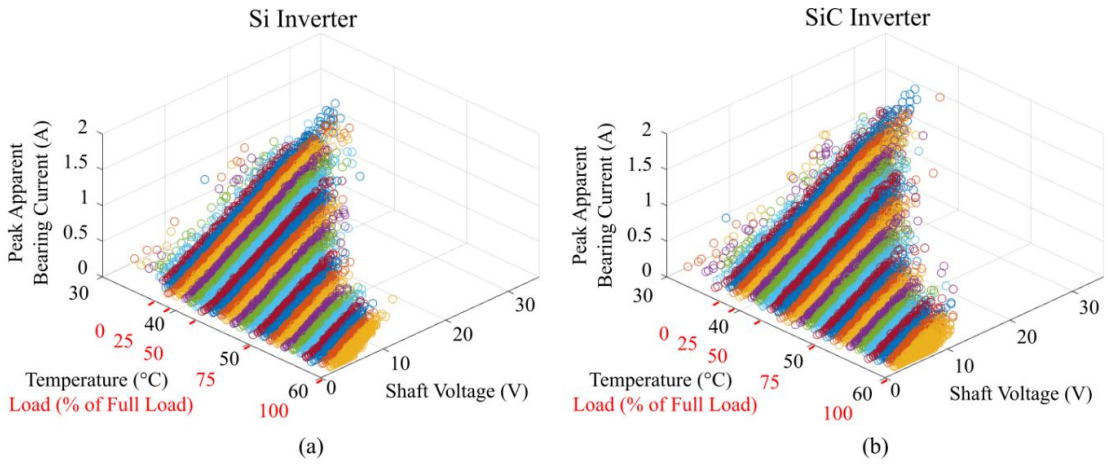

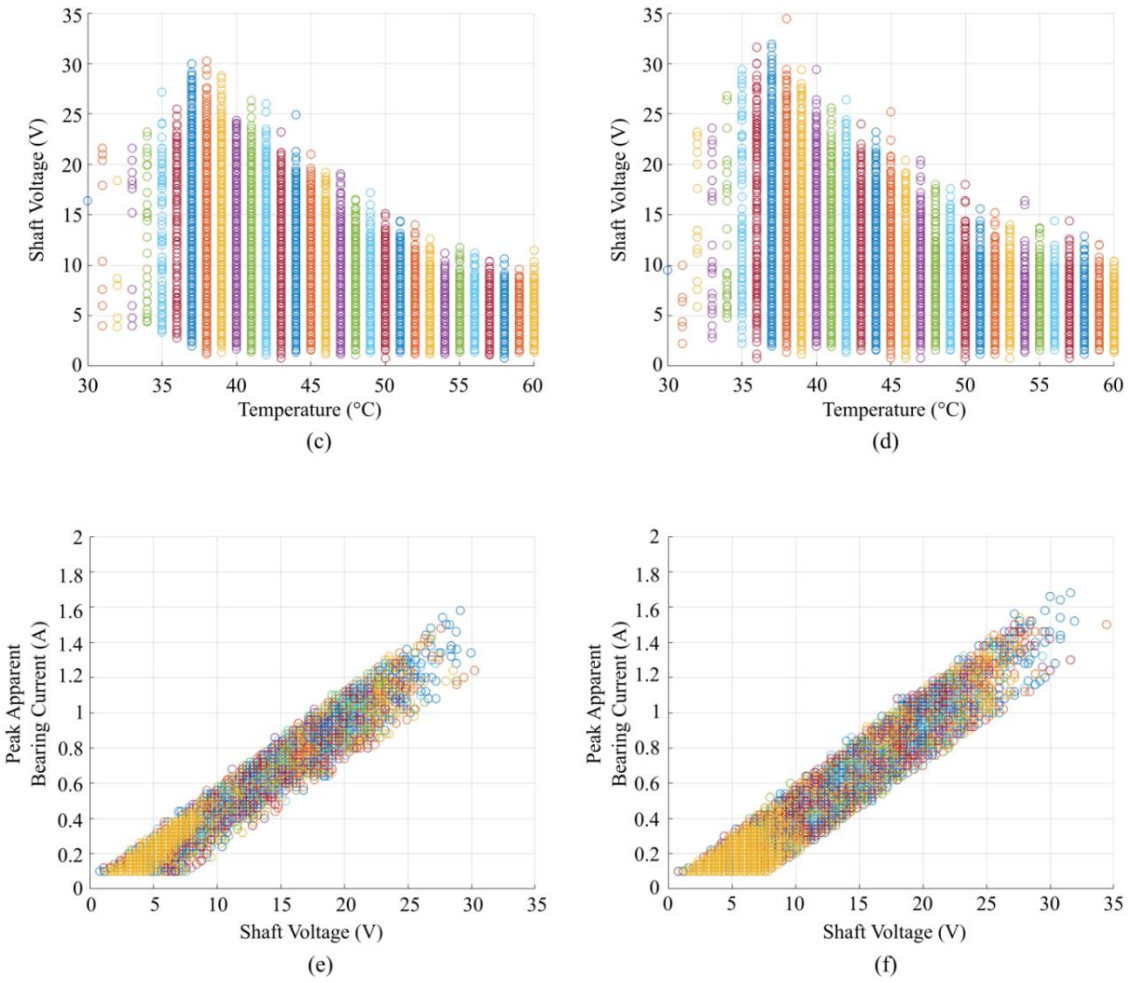

Figure 5.8. Bearing EDM shaft voltage and bearing current data for various bearing operational temperature: 3D plots for (a) Si and (b) SiC inverters, 2D plots comparing shaft discharge voltages against operational temperature for (c) Si and (d) SiC inverters, and 2D plot displaying the peak apparent bearing currents for a given shaft breakdown voltage for (e) Si and (f) SiC inverters.

Analysis

As the bearing temperature and machine load increase, the maximum amplitude of the shaft voltage and bearing current discharges decrease, due to a thinner lubricant at higher temperatures. A thinner lubricant leads to an increase in the electric field between the inner and outer race of the bearing for the same shaft voltage, which results in discharges occurring at lower voltages. In other words, the maximum possible shaft voltage for each

operating point decreases with an increase in temperature and load because the lubricant dielectric cannot support an electric field greater than the electric field required to produce dielectric breakdown and a discharge. At a 37°C bearing operational temperature, the lubricant is just becoming thin enough to produce discharges. Since this is the operational point with the thickest lubricant where discharges are present, it is also the operating point with the largest amplitude of shaft voltages and bearing currents. Below 37°C, the lubricant is thick enough that a discharge event becomes very rare (34 discharge events at 34°C in 1000 ms vs. 10,961 discharge events at 39°C in 1000 ms), and the shaft voltage is a fraction of the machine CM voltage.

Peak Apparent Bearing Current Distribution

The peak apparent bearing current amplitude is linearly dependent on the shaft breakdown voltage at each motor operational point due to the linearity of the discharge circuit (Ch. 3, Fig. 5.8(e&d)). A line of best fit was implemented for the data displayed in Fig. 5.8(e&d).

$$i_{fit}(v) = 0.05v - 0.07, i_{fit} > 0 \tag{5.7}$$

However, inspection of Fig. 5.8(e&d) reveals that the peak apparent bearing current for any amplitude of shaft voltage discharge does not exactly follow the relationship of Eq. (5.7), but follows a distribution, appearing within a certain range of the linear relationship. This is due to the variable discharge resistance. To investigate this, three different discharge sets were analyzed for the Si and SiC inverter shaft voltage and bearing current data: 9.7 V discharges produced by the SiC inverter at 42°C, 7 V discharges produced by the SiC inverter at 37°C, and 15 V discharges created by the Si inverter at 38°C. It was determined

that the peak apparent bearing current for any particular shaft voltage follows a normal distribution, the results of which can be seen graphically in Fig. 5.9.

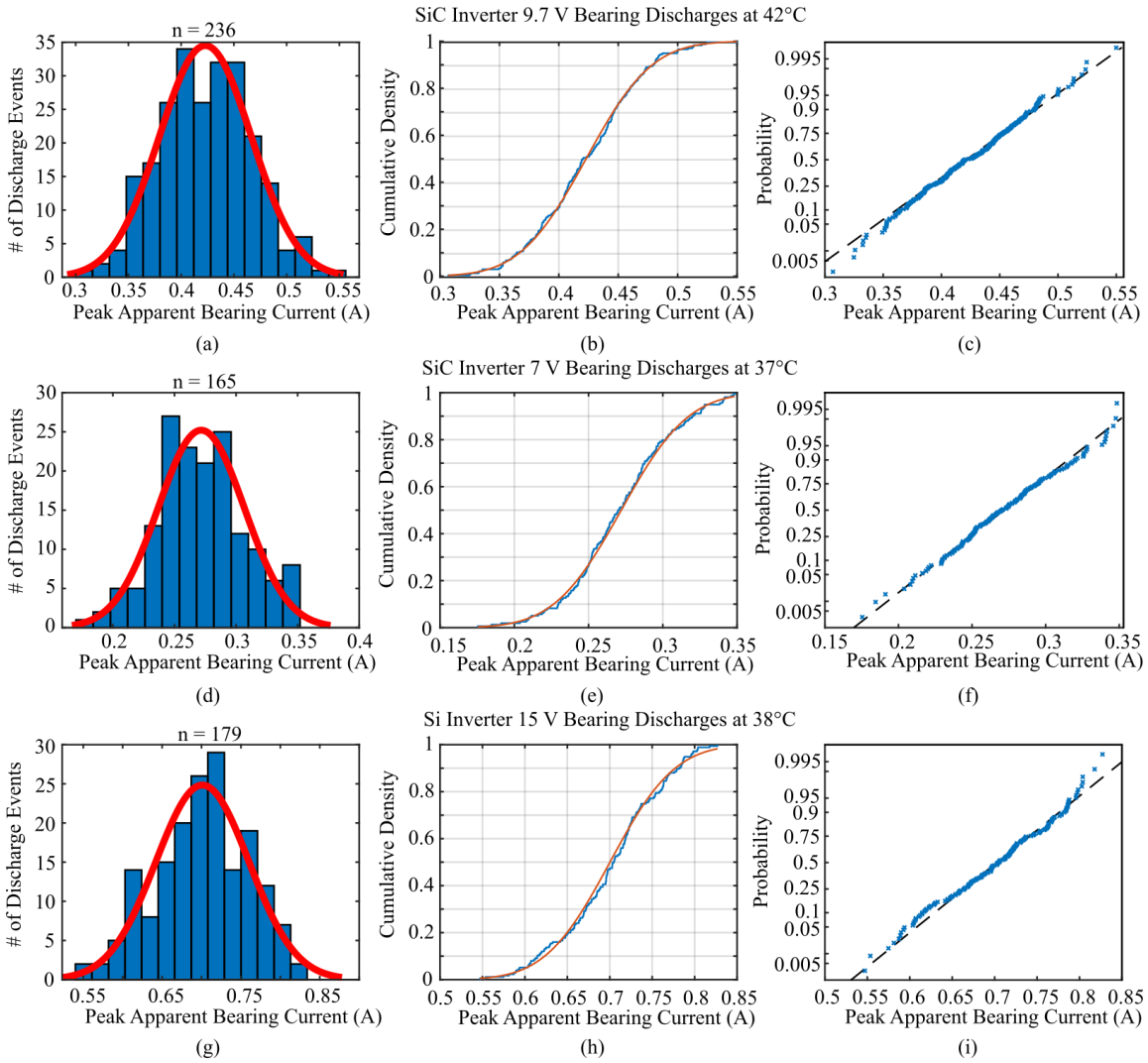

Figure 5.9. The resulting peak apparent bearing current follows a normal distribution for any particular shaft breakdown voltage: (a, d, g) histograms of experimental data with fitted theoretical normal distributions, (b, e, h) cumulative density plots comparing data (blue) with theoretical normal distributions (orange), and (c, f, i) probability plots demonstrating the normally distributed data for 9.7 V and 7 V discharges from the SiC inverter and 15 V discharges from the Si inverter from top to bottom, respectively.

From Fig. 5.9, the plots demonstrate the normally distributed peak apparent bearing current data for any particular shaft breakdown voltage. A few modifications to the data were necessary. First, small groups of outliers were identified beyond three standard deviations below the mean of each distribution. These outliers are due to algorithm error. The algorithm used to extract discharge amplitudes iterates through the shaft voltage and apparent bearing current oscilloscope waveforms, searching for local maximums in the bearing current signal. When a bearing current local maximum is detected, it is recorded along with the maximum shaft voltage within that local area. Although effective, the algorithm is prone to occasional error such as noise and larger amplitude displacement currents. These outliers were thoroughly investigated, and it was determined from viewing the shaft voltage and bearing current waveforms that discharge events recorded below three standard deviations from the peak apparent bearing current mean were false readings from the algorithm, and therefore can be disregarded. Second, the ADC resolution of the Tektronix MDO3014 oscilloscope for this application was 20 mA, therefore each data point extracted by the algorithm falls into a bin with 20 mA spacing. In order to test for normality of the data, the Shapiro-Wilk Test was implemented [70], which was used in tandem with visual evaluations of Fig. 5.9. The Shapiro-Wilk Test is very sensitive to discrete data. By adding a uniformly distributed random noise signal to the data with an amplitude of 0.02, the data can be moved out of the discrete bins into a continuous distribution without altering the mean or standard deviation of the distribution. To see the effects of the injected noise and elimination of the outliers that are a result of algorithm error, a probability plot of the raw data is provided in Fig. 5.10. This plot does not contain the uniformly distributed noise and includes the erroneous outliers.

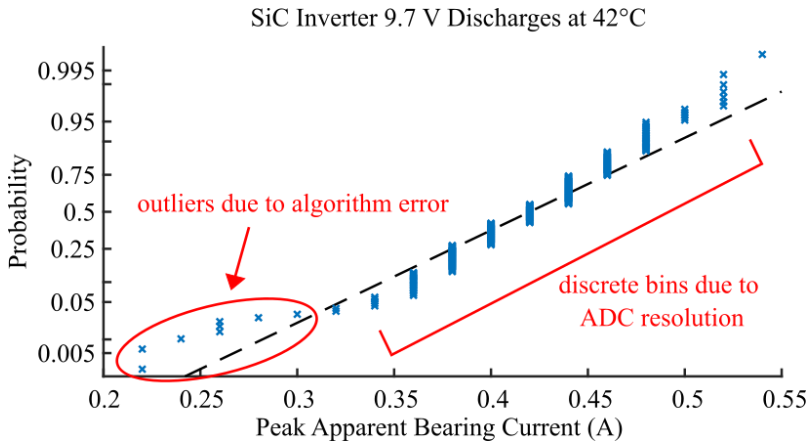

Figure 5.10. Probability plot of the raw SiC 9.7 V, 42°C peak apparent bearing current data.

Visual comparison of Fig. 5.10 and Fig. 5.9(c) demonstrates how the outliers due to algorithm error do not follow the main body of data that is normally distributed, and cause the tail of the distribution on the upper end > 0.5 A to begin departing from the theoretical normal distribution line. Additionally, the discrete data bins spaced 20 mA apart are also apparent. Discarding the irrelevant outliers and adding the uniformly distributed noise allowed for accurate use of the Shapiro-Wilk test and for ease in visually evaluating the cumulative density and probability plots of each distribution. The numerical results of the data displayed graphically in Fig. 5.9 are shown in Table 5.1, where a Shapiro-Wilk Test for normality was conducted at a significance level of $\alpha = 0.05$. A percent error statistic is also calculated to compare the mean value μ of the current distribution with the fitted line of Eq. (5.7). The normal distribution standard deviation is denoted σ.

$$\delta = \frac{i_{\mu} - i_{fit}}{i_{fit}} \times 100\% \tag{5.8}$$

Table 5.1. Normal distribution statistics for peak apparent bearing current distributions of Fig. 5.9.

			Peak Apparent Bearing Current				
Inverter	Bearing Temperature	Shaft Voltage	i_{fit} Eq. (5.7)	μ	δ Eq. (5.8)	σ	Shapiro Wilk Test $\alpha = 0.05$
SiC	42	9.7	0.415	0.423	1.9%	0.044	accept
SiC	37	7	0.280	0.272	-2.9%	0.035	accept
Si	38	15	0.680	0.701	3.1%	0.059	accept

From Table 5.1, the Shapiro Wilk null hypothesis to determine if a normal distribution is a reasonable assumption of the peak bearing current distributions for a single shaft voltage can be accepted with 95% probability (α = 0.05). The primary reason for the current distribution is the varying bearing discharge resistance between each discharge. This can be attributed to slight variations in lubricant thickness upon breakdown for each discharge, asperity differences on the race and ball surfaces, alignment of the bearing and shaft, and radial and axial bearing loads. Therefore, the potential discharge resistances of each discharge also follow a normal distribution, since this distribution causes the peak apparent bearing current distribution.

Discharge Resistance Distribution

To investigate this, the modified IM equivalent circuit discharge model of Ch. 3 was employed to explore the bearing discharge resistances that are associated with the peak apparent bearing current amplitudes measured that form the distributions of Fig. 5.9. A parameter sweep was performed in PSpice on the bearing discharge resistance,

resulting in varying peak apparent bearing current amplitudes. The results can be seen in Fig. 5.11.

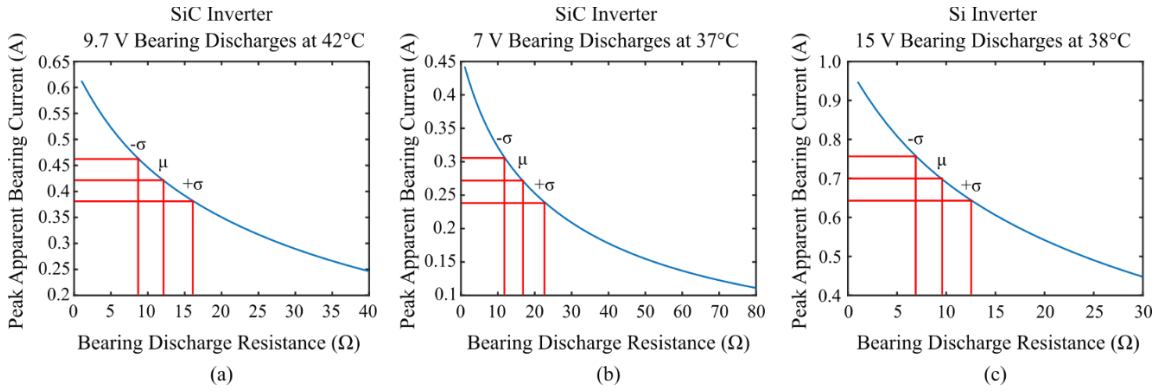

Figure 5.11. The normally distributed peak apparent bearing current is due to a normally distributed bearing discharge resistance. This can be seen for discharges produced by the SiC inverter at (a) 9.7 V, 42°C, (b) 7 V, 37°C, and for the Si inverter at (c) 15 V, 38°C.

From Fig. 5.11, markers are provided to demonstrate how the mean and standard deviation of the current distributions align with the mean and standard deviation of the bearing discharge resistance distributions. A summary of the bearing discharge resistance normal distributions is provided in Table 5.2.

Table 5.2. Summary of bearing discharge resistance normal distributions produced by the SiC inverter at 9.7 V, 42°C, and 7 V, 37°C, and for the Si inverter at 15 V, 38°C.

			Bearing Discharge Resistance (Ω)	
Inverter	Bearing Temperature	Shaft Voltage	μ	σ
SiC	42	9.7	11.9	3.4
SiC	37	7	16.5	4.8
Si	38	15	9.0	2.3

In the literature, bearing discharge resistances are reported in the range of 1-10 Ω [6]. The results displayed in Table 5.2. validate the bearing discharge resistance value and shows that they can also span to slightly higher values.

Discharge Amplitude

This section analyzes the parameters that affect the amplitudes of the EDM discharges. To compare the change in maximum discharge intensity at each operational temperature, an average of the 100 largest discharges at each temperature point are compared between Si and SiC inverters, as is seen in Fig. 5.12, where the shaft voltage for the machine when line-driven is provided as a reference.

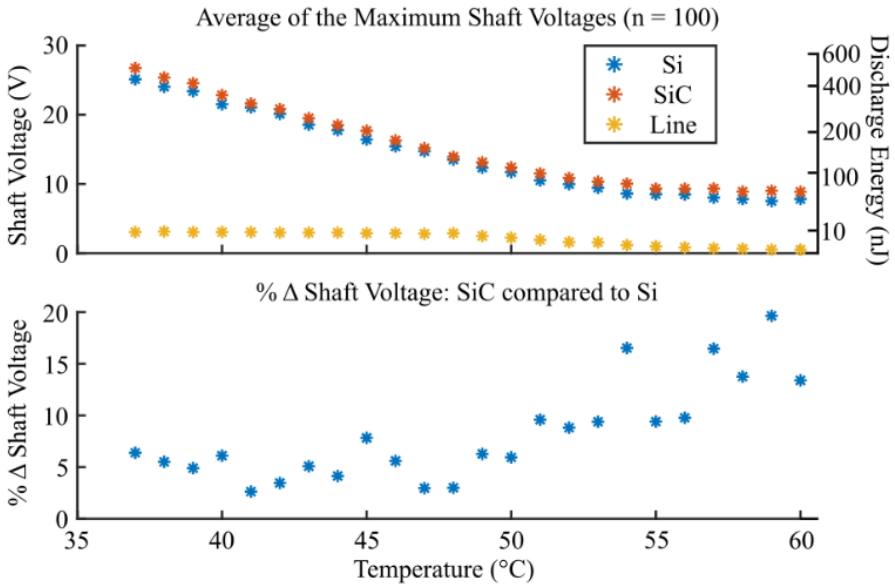

Figure 5.12. Comparison of maximum shaft discharge voltages at various bearing operational temperatures for Si- and SiC-based inverters, with line-driven operation included.

Both the Si and SiC inverter started to experience shaft voltage breakdown and bearing current shoot through at a bearing temperature of ~37°C, while the line driven

machine shaft voltage begins to break down at ~51°C. A plot of the percent change in the largest shaft voltages between Si and SiC inverters is provided in Fig. 5.12:

$$\%\Delta = \frac{V_{SiC} - V_{Si}}{V_{Si}} \times 100\% \tag{5.9}$$

On average when comparing Si and SiC devices, the largest shaft voltage discharges increased by 8.2% across all temperatures, and since the resulting peak bearing current is linearly proportional to the shaft breakdown voltage, the bearing current amplitude increases as well. The results show that dielectric breakdown theory due to device rise time becomes especially relevant above bearing temperatures of 50°C (machine loads > 75% of rated load), as the SiC shaft voltage showed an average increase of 12.7% in this region compared to Si. The corresponding discharge energies are also provided in Fig. 5.12, calculated using the models of Ch. 3:

$$E_{discharge} = \frac{1}{2}\left(C_{rf} + 2C_b\right){V_{shaft}}^2 \tag{5.10}$$

Here, V_{shaft} is the shaft voltage at the time of the discharge event. To calculate bearing current for an unmodified machine, the ratio φ of Eq. (3.14) can be employed, since the slope of the linear relationship between the shaft breakdown voltage and the peak apparent EDM bearing current depends on the outer race-to-frame grounding wire inductance L_w.

Inverse Gaussian Analysis

The variation in shaft breakdown volage and peak bearing current at each operational temperature can be described with an inverse Gaussian distribution, where the mean μ and the shape parameter λ describe the distribution. Only the shaft voltage will be considered in this analysis, since it has been demonstrated that the shaft voltage is the causal factor for lubricant breakdown and EDM bearing currents. The peak apparent

bearing current distributions for a given operational temperature can be calculated from the modeling of Ch. 3 by using the shaft voltage initial breakdown conditions, for both modified and unmodified machines. The generic form of the inverse Gaussian distribution is shown in Eq. (5.11).

$$f\left(V_{shaft}, \mu, \lambda\right) = \sqrt{\frac{\lambda}{2\pi {V_{shaft}}^3}}\, e^{\left(-\frac{\lambda(V_{shaft}-\mu)^2}{2\mu^2 V_{shaft}}\right)} \tag{5.11}$$

The inverse Gaussian distributions describing the Si and SiC shaft breakdown voltages can be seen in Figs. 5.13 & 5.14 for various temperatures, while Fig. 5.15 visually demonstrates the inverse Gaussian shape of the raw data for 1000 ms of shaft breakdown voltages at a bearing temperature of 45°C.

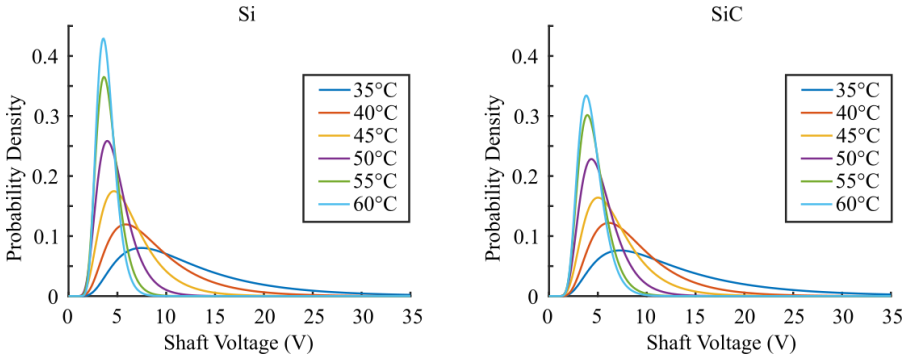

Figure 5.13. Si and SiC inverter shaft breakdown voltage inverse Gaussian distributions for various bearing operational temperatures.

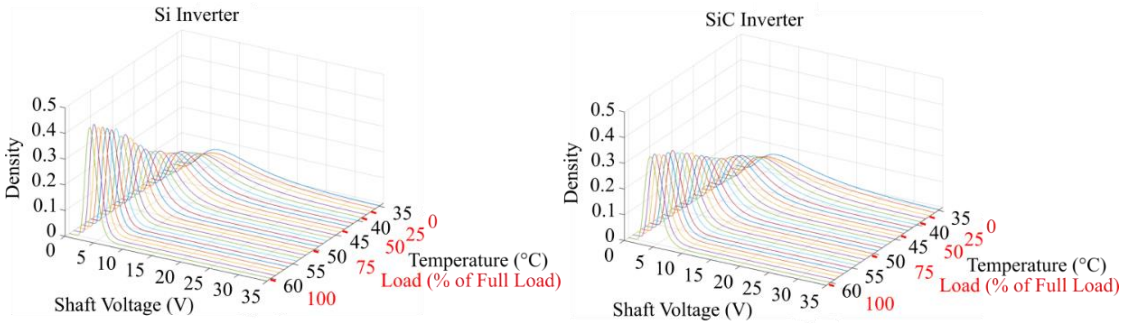

Figure 5.14. 3D plots of Si and SiC inverter shaft breakdown voltage inverse Gaussian distributions across bearing operational temperatures.

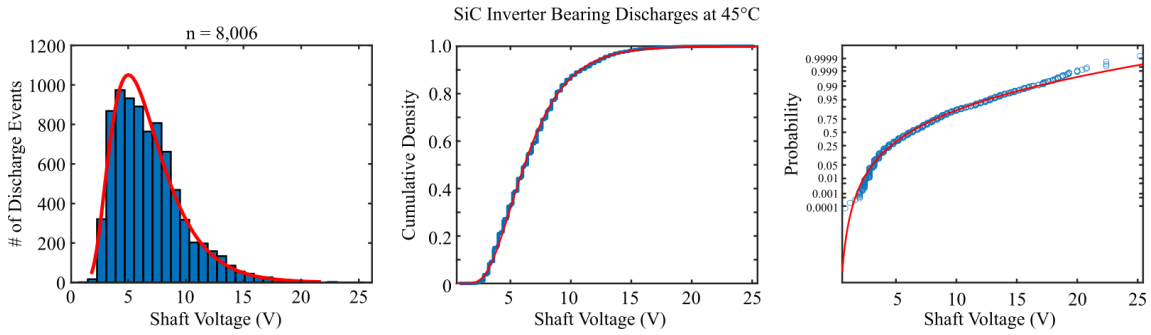

Figure. 5.15. SiC inverter shaft breakdown voltage data at a bearing temperature of 45°C: (a) histogram with fitted distribution, (b) cumulative density plot, and (c) probability plot. In 1000 ms at at f_s = 10 kHz, 8,006 discharge events were recorded.

From Fig. 5.14, the distributions are dependent on bearing temperature. A comparison of the mean and scale parameter for Si and SiC inverter inverse Gaussian distribution functions at various operational temperatures is summarized in Table 5.3.

Table 5.3. Summary of mean (μ) and shape (λ) parameters for shaft discharge voltage inverse Gaussian distributions over various bearing operational temperatures.

Bearing Temperature	Si		SiC	
	μ	λ	μ	λ
35°C	12.3527	35.2079	12.8455	32.1061
36°C	12.4745	34.7524	12.7091	27.1138
37°C	12.0070	32.8321	11.4103	31.5019
38°C	10.6137	34.0036	10.3232	35.4892
39°C	9.4384	32.2878	9.3202	35.5080
40°C	8.6808	32.2458	8.7105	36.1585
41°C	7.9537	31.6164	8.0266	33.5604
42°C	7.6655	30.6267	7.5649	33.5297
43°C	7.2186	30.3921	7.2825	32.8228
44°C	6.8500	30.8592	7.0392	32.7083
45°C	6.3150	30.4267	6.7725	33.4267
46°C	6.0649	30.9156	6.3739	32.8333
47°C	5.8453	31.5336	6.1311	34.7440
48°C	5.4703	31.8667	5.8569	36.0973
49°C	5.1271	34.7397	5.5887	36.8487
50°C	4.8606	35.4712	5.3871	36.9513
51°C	4.5872	39.3704	5.1204	38.7430
52°C	4.4020	41.6240	4.9985	39.8471
53°C	4.3783	42.5335	4.8522	40.2537
54°C	4.1525	47.5079	4.7711	42.4918
55°C	4.1232	48.5210	4.5945	43.8452
56°C	4.0623	51.3341	4.5568	44.0631
57°C	3.9937	53.5966	4.5423	44.1554
58°C	3.9755	56.1018	4.3837	43.2468
59°C	3.9337	61.6098	4.3703	47.1179
60°C	3.9279	60.6665	4.3743	47.8430

The distribution parameters can be seen graphically in Fig. 5.16. Difference plots are provided for ease in viewing the effects of device rise time on the Si and SiC inverse Gaussian distributions.

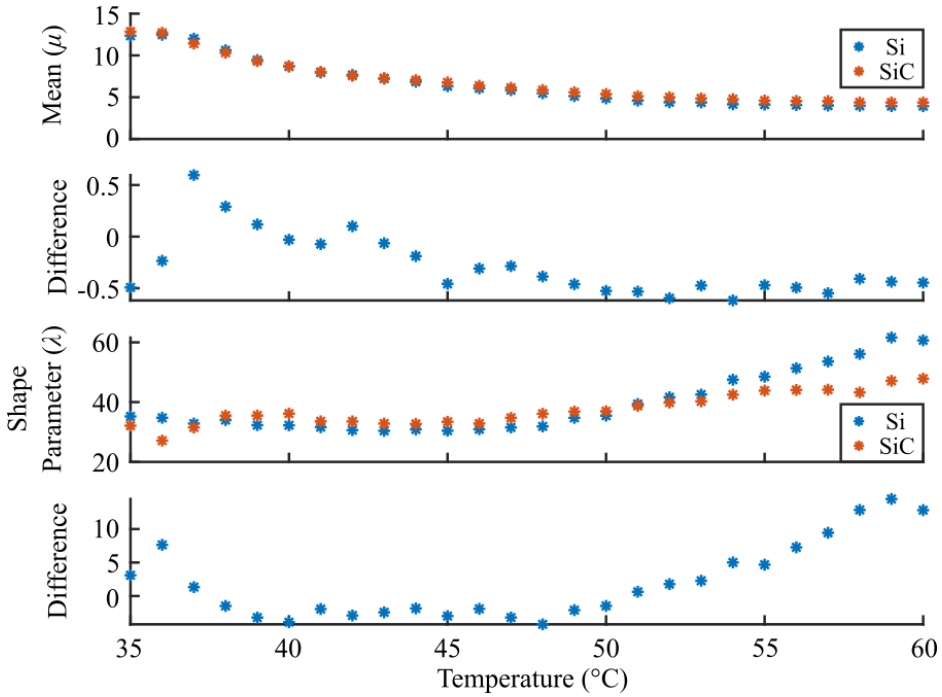

Figure 5.16. Mean and shape parameters of the shaft breakdown voltage inverse Gaussian distributions plotted against temperature. Difference plots are also provided to see the difference between Si and SiC inverters.

A slight difference in the distribution mean can be seen at temperatures greater than 45°C (greater than 50% of machine full load) and a significant difference in the distribution shape parameter develops above 50°C, as can be seen in the difference plots of Fig. 5.16. For temperatures below 45°C, the trend of the differences between the distribution parameters are not as strong, although the plots of Fig. 5.12 still suggest that shaft voltages due to SiC inverters can reach slightly larger magnitudes in this region. As the temperature increases, the decreasing mean shows how the distribution of shaft breakdown voltages are shifted to lower values, while the increasing shape parameter helps account for the discharge

voltages being concentrated into a narrower value of voltages, becoming less right skewed with an increase in temperature. When comparing the Si and SiC distributions, the relatively larger mean and lower shape parameters of the SiC inverter shows that the distributions cluster more narrowly at a lower shaft breakdown voltage for the Si inverter. The smaller shape parameter exhibited by the SiC inverter at temperature greater than 50°C demonstrates that these distributions are more skewed to the right than the Si inverter distributions at the same temperature, which means that the experimentally measured amplitude of shaft breakdown voltages is larger in this region for the SiC inverter.

Therefore, although EDM discharges due to shaft voltages and bearing currents are most intense at no load/lightly loaded conditions, the greatest difference between EDM discharges for Si and SiC devices is seen at bearing temperatures greater than 50°C, which correspond to machine loading levels greater than 75% of rated load. These results indicate that substantial differences in bearing lifetime may be seen when driving a machine at rated load with SiC devices, compared to Si devices.

EDM Rate

Now that the amplitudes of EDM discharges have been fully characterized with probability density functions, the final aspect to acquire to fully describe their activity is how often they occur, which is known as the EDM rate. Muetze et al. demonstrated that the EDM rate is linearly proportional to the PWM switching frequency [20]. However, the results shown in Fig. 5.17 indicate that the EDM rate is also dependent on the bearing temperature, and by extension the machine loading level. In Fig. 5.17, the switching frequency remains fixed at f_s = 10 kHz, and the EDM rate is normalized about the switching frequency.

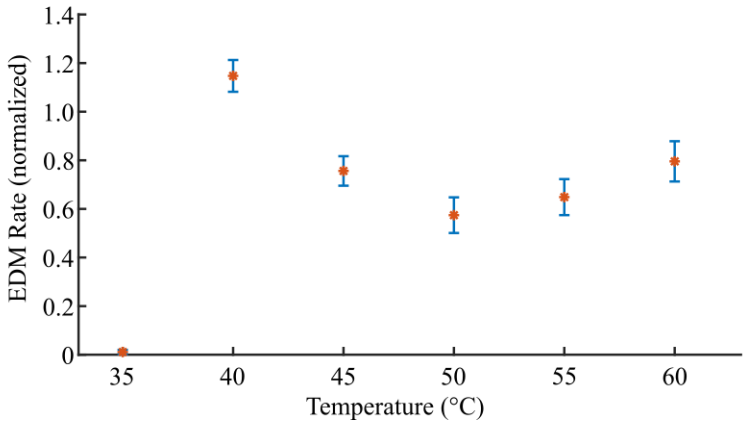

Figure 5.17. Average EDM rate for experiments conducted using the aforementioned procedure with standard deviation error bars. The EDM rate is normalized about the inverter switching frequency, where f_s = 10 kHz for these measurements.

At low bearing temperatures and machine loading conditions (e.g., < ~37°C), the lubricant remains intact causing the EDM rate to remain low. Above the dielectric breakdown threshold the largest EDM rate is seen around 40°C, which corresponds to no/light machine loading. In this region the EDM rate exceeds the PWM switching frequency. Recall that the inverter has six semiconductor switches operating at the switching frequency, therefore EDM rate exceeding the switching frequency rate is permissible. The EDM rate then decreases for medium machine loading, and then increases again at full load to ~0.8f_s. From this, it can be concluded that the EDM rate is most damaging to bearings at no/lightly loaded conditions, followed by full load conditions.

Discussion

Various researchers have demonstrated that the voltage slew rate of a voltage pulse applied across a dielectric significantly affects the breakdown voltage magnitude [34-38]. Wang et al. [34] developed a high-level mathematical concept to predict an

expectation breakdown voltage given an inception voltage, a maximum possible breakdown voltage, an exponentially probabilistic function that describes the electron delay time of the system, and a slew rate of the applied voltage pulse. Applied to the bearing discharge phenomena, the expectation voltage is the predicted breakdown voltage, the inception voltage is the dielectric's breakdown voltage at DC, and the maximum possible voltage is typically set by the system's voltage source. The model effectively demonstrates how voltage pulses with higher slew rates produce larger expectation voltages at breakdown, given all other parameters are fixed. Unfortunately, this mathematical method contains too many degrees of freedom to apply to the physics considered in this research. Nevertheless, the concept remains a valid framework for analyzing electrical discharge behavior in motor bearings for alterations in the semiconductor device slew rate and contains the underlying principle that connects the BVR theory with the pulsed dielectric theory. As previously discussed, the BVR is set based on the machine parasitic capacitances. These parasitics do not change with temperature, therefore the voltage that attempts to build on the shaft as produced by the CM voltage remains constant in amplitude throughout bearing operational temperature. However, the threshold for lubricant dielectric breakdown decreases with an increase in temperature, as has been experimentally and statistically demonstrated in this chapter. The temperature T_d at which the threshold for bearing lubricant dielectric breakdown becomes equal to the maximum shaft voltage is where the first bearing discharges appear, as seen in Fig. 5.18.

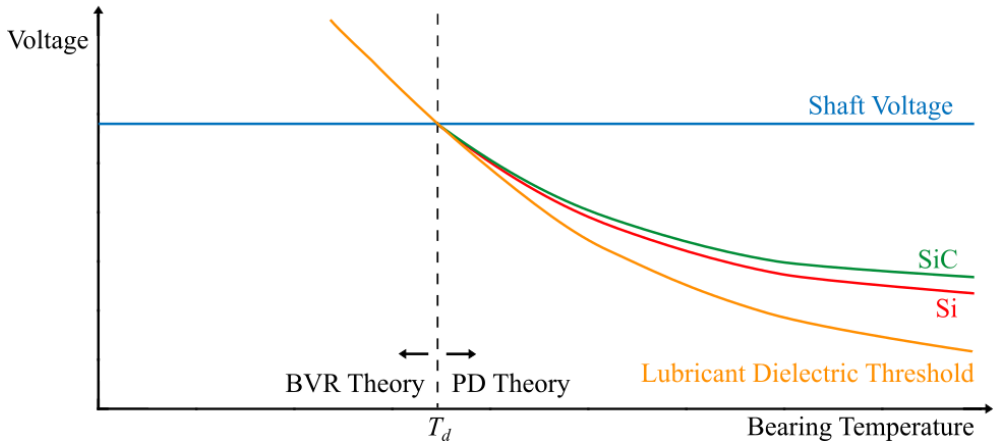

Figure 5.18. Comparison of the lubricant dielectric threshold at DC, and shaft discharge voltages produced by Si and SiC inverters. The temperature at which discharges are first observed is denoted T_d.

In Fig. 5.18, the blue line represents the shaft voltage as set by the BVR. The orange line represents the threshold for bearing lubricant dielectric breakdown. Above T_d the shaft voltage set by the BVR exceeds the lubricant dielectric threshold, resulting in discharges. Therefore, BVR theory explains the shaft voltage amplitude below T_d, while pulse dielectric theory explains shaft voltage amplitude above T_d. Connecting to the work performed by Wang et al., the lubricant dielectric threshold (orange) represents the inception voltage, while the shaft voltage as set by BVR theory represents the maximum possible breakdown voltage. Since the inception voltage of the lubricant is greater than the maximum possible voltage on the shaft in the BVR region ($T_d < 0$), no discharges occur, the lubricant remains intact, and the shaft voltage is a fraction of the CM voltage as set by the BVR. Above T_d, the inception voltage drops below the maximum possible breakdown voltage, allowing discharges to occur. As the temperature increases, the difference between the maximum possible shaft voltage and the inception voltage also increases, and therefore the slew rate of the semiconductor switching devices begins to

affect the expectation voltage for shaft breakdown. The increasing difference between the maximum possible shaft voltage and the lubricant dielectric threshold as the bearing temperature increases is the reason that the difference in expectation breakdown voltage between Si and SiC switching devices becomes more apparent. This explains why only a small difference between Si and SiC shaft breakdown voltages can be seen below 50°C, and the difference between the devices becomes larger and more significant above 50°C.

CHAPTER SIX

Vibration due to EDM Bearing Currents and Lifetime Projection

When an EDM discharge event occurs, Chapter Four demonstrated that a small local area of bearing steel melts, damaging the ball and race surface, the extent to which is dependent on the discharge energy (i.e., shaft voltage and bearing current amplitudes). As time goes on, more and more defects accumulate on the ball and race surfaces due to additional EDM discharges, and as the bearing spins and the balls run over the defected surfaces, the vibration increases over time. Eventually, the vibration reaches a level that is no longer acceptable, and the bearing is considered to have failed. The International Organization for Standardization (ISO) has developed ISO 10816-1 [71] to determine acceptable and unacceptable machine vibration levels for Class I – Class IV machines, which can be seen in Fig. 6.1.

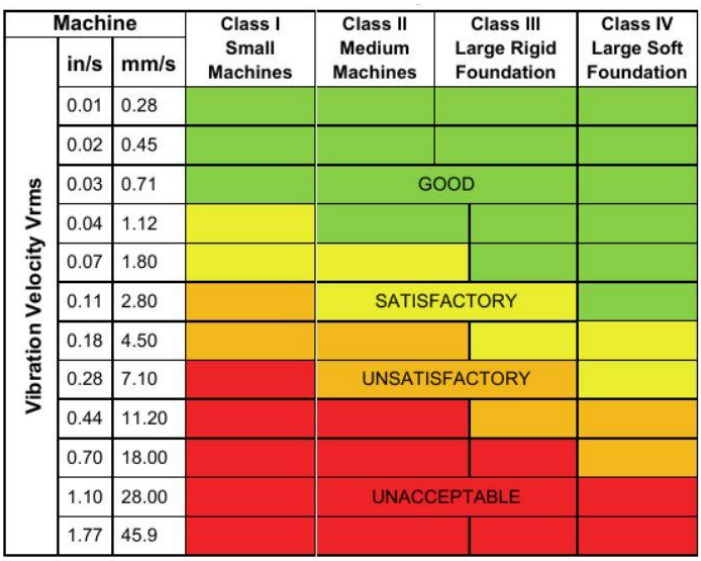

Figure 6.1 ISO10816-1 standard for vibration severity in electrical machines

In this research, the 5 hp bearings used fall under the category “Class 1 Small Machines”. Therefore, the lifetime of the bearing is determined by the amount of time it takes for the bearing vibration to cross over into the “unacceptable” region of operation, that is when the vibration meets or exceeds 7.10 mm/s. The vibration level of a bearing can be easily monitored over time through the use of a commercially available vibration meter, such as the Fluke 805 FC, which is used in this work. In a typical industrial setting, technicians will monitor machine vibrations with a vibration meter, looking for a sudden jump in vibration amplitude which indicates the beginning of the exponential increase in vibration, as shown in Fig. 1.10. When it has been determined that the bearing’s vibration has reached the beginning of the exponential increase, the machine can be temporarily decommissioned and prepared for bearing replacement.

This vibration data-driven maintenance method is effective yet requires highly accurate record keeping and frequent vibration measurements to be made by technicians. This chapter proposes an alternative method that will be tested through experimental evidence, namely using the EDM shaft voltage and bearing current distributions at each motor operational point to predict the number of discharges until bearing failure. This will be achieved by analyzing the experimental results of vibration degradation patterns of various bearings subject to varying EDM discharge amplitudes on the bearing testbed. By performing the experiments at an accelerated rate, timely results can be obtained, and then lifetime predictions can be extrapolated down into the discharge energy region that is typical for 5 hp motors.

Bearing Defect Frequencies

In a rolling element bearing that rotates at f_{spin} with the outer race stationary and the inner race rotating, the expected defect frequencies are:

$$f_c = \frac{f_{spin}}{2}\left(1 - \frac{D_r}{D_p}\cos(\alpha)\right) \tag{6.1}$$

$$f_{bpo} = \frac{f_{spin}N_r}{2}\left(1 - \frac{D_r}{D_p}\cos(\alpha)\right) \tag{6.2}$$

$$f_{bpi} = \frac{f_{spin}N_r}{2}\left(1 + \frac{D_r}{D_p}\cos(\alpha)\right) \tag{6.3}$$

$$f_{bs} = \frac{f_{spin}D_p}{2D_r}\left(1 - \left(\frac{D_r}{D_p}\cos(\alpha)\right)^2\right) \tag{6.4}$$

Each parameter is as follows: f_c is the cage frequency, f_{bpo} is the outer race ball pass frequency, f_{bpi} is the inner race ball pass frequency, f_{bs} is the ball spin frequency, D_p is the bearing pitch diameter, D_r is the rolling element diameter, N_r is the number of rolling elements, and α is the contact angle [41, 72]. The contact angle is demonstrated in Fig. 6.2. The contact angle is the angle formed between two lines, the first being a line between the two ball contact points on the inner and outer races, and the second line being perpendicular to the tangential motion of the bearing.

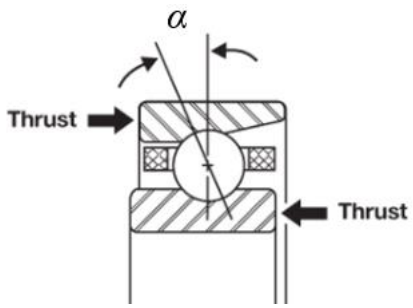

Figure 6.2. Bearing contact angle α [73].

Eqs. (6.1 & 6.4) give the cage frequency and the ball spin frequency, respectively, while Eqs. (6.2-6.3) give the vibration frequency generated for a single defect on the outer and inner race, respectively. Therefore, if more than just one defect is present on the inner or outer race, one can expect frequency harmonics to be generated that are multiples of f_{bpo} and f_{bpi}. For the 6306 bearings considered in this research, the bearing parameters and defect frequencies are highlighted in Table 6.1.

Table 6.1. SKF 6306 bearing parameters and defect frequencies for 1800 rpm operation (f_{spin} = 30 Hz).

Bearing Parameter	Value	Defect Frequency	Value
N_r	8	f_c	11.25 Hz
D_p	12.5 mm	f_{bpo}	90 Hz
D_r	50 mm	f_{bpi}	150 Hz
α	0°	f_{bs}	60 Hz

Experimental Procedure

An experimental procedure was developed to analyze the connection between EDM discharge energy and the number of discharges to bearing failure. Each bearing tested was subject to a fixed discharge energy, which was applied at a level that is much larger than discharge energies typically seen on 5 hp motor bearings driven by PWM inverters. The reasoning for this is the fact that discharge energies that occur in typical

PWM inverter motor drive systems can be very small in energy, resulting in a lengthy amount of time for the bearing to fail. To achieve timely results in the laboratory setting, larger amplitude discharges are chosen because these discharges will cause more damage to the ball and race steel, as was demonstrated in Chapter Four, which in turn will produce more vibration in a shorter amount of time. A summary of the experimental parameters for the experiments conducted is given in Table 6.2.

Table 6.2. Summary of accelerated vibration experiment parameters.

Experiment No.	Discharge Voltage	Energy/Discharge (nJ)
1	90	8100
2	80	6400
3	70	4900
4	90	8100
5	90	8100

Bearing Speed	Bearing	EDM Rate	Piezo Sensor	Vibration Meter
1800 RPM	SKF 6306-2Z/C3	25 kHz	TE Connectivity SDT Shielded	Fluke 805 FC

Each experiment is performed at a fixed speed of 1800 RPM and a fixed EDM Rate of 25 kHz. Various discharge voltages were employed, where the discharge energy can be calculated from the voltage as $\frac{1}{2}CV^2$, using the values from the bearing testbed. In the first three experiments the discharge voltage was 90 V, 80 V, and 70 V, which corresponds to discharge energies of 8100 nJ, 6400 nJ, and 4900 nJ, respectively. An additional two experiments (4-5) were performed at the 90 V (8100 nJ) discharge level to observe the repeatability of the results. Each experiment used SKF 6306-2Z/C3 bearings. Two methods were employed to measure bearing vibration: a Fluke 805 FC vibration meter and a TE Connectivity SDT shielded piezo sensor. The Fluke 805 FC was used to track the bearing vibration relative to ISO10816-1, while the piezo sensor acquired

vibration time domain data. Vibration measurements were performed every 24 hours with the Fluke 805 FC and every 6 hours with the piezo sensor. Each experiment ran until the bearing was determined to be failed per ISO10816-1.

Results

The results obtained by the Fluke 805 FC vibration meter can be seen graphically in Fig. 6.3 and numerically in Table 6.3. ISO10816-1 is included in Fig. 6.3 to demonstrate the vibration measurement crossing the failure threshold.

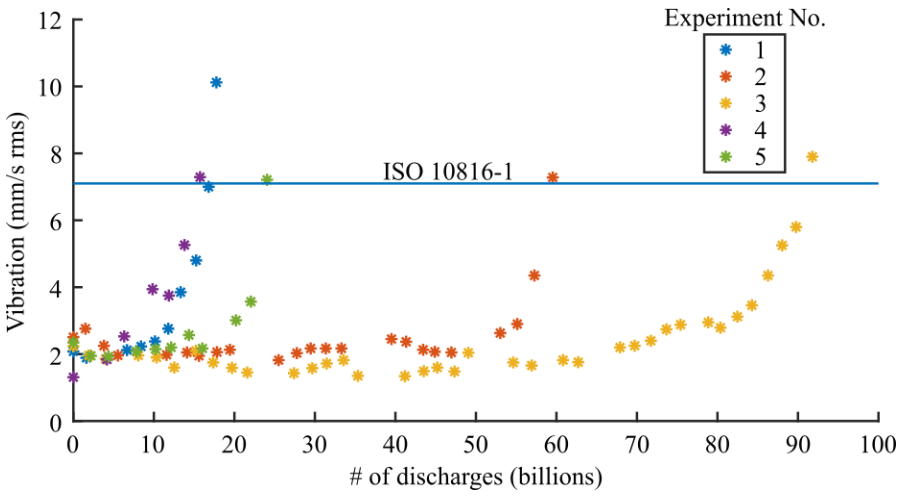

Figure 6.3. Fluke 805 FC vibration meter results for the experiments of Table 6.2.

Table 6.3. Fluke 805 FC vibration meter results for the experiments of Table 6.2.

Experiment No.	Discharge Voltage	Energy/Discharge (nJ)	# of discharges to failure	Time to failure (days)
1	90	8100	16,900,000,000	9
2	80	6400	59,540,000,000	29
3	70	4900	90,770,000,000	48
4	90	8100	15,740,000,000	8
5	90	8100	24,060,000,000	12

Similar exponentially increasing vibration signals can be seen from the piezo vibration sensor, as shown in Fig. 6.4 for experiment no. 1, the first 90 V (8100 nJ) discharge test. Although the piezo sensor is shielded, significant EDM EMI infects the electrical signal. However, close observation of Fig. 6.4 still reveals that the electrical signal vibration envelope is increasing as more discharges occur, as indicated with the red arrows.

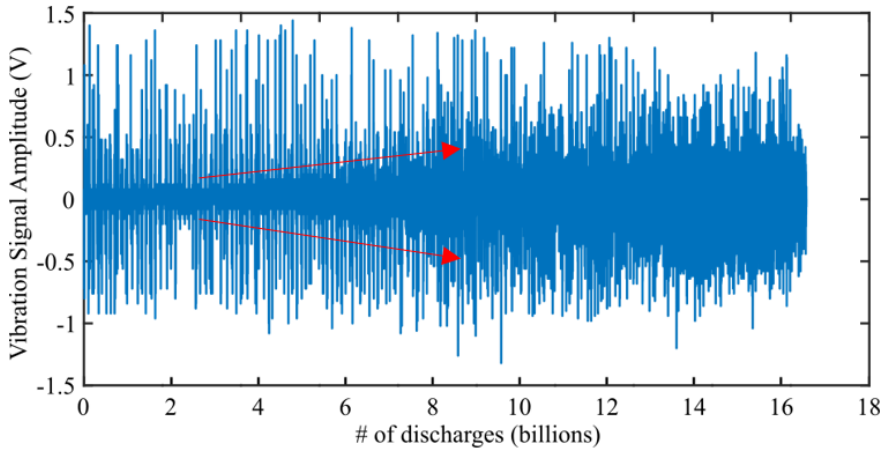

Figure 6.4. Piezo vibration sensor electrical signal over the course of the first 90 V (8100 nJ) discharge experiment (experiment no. 1) with red arrows indicating an increase in the vibration envelope.

As expected from the FE model, the number of discharges to failure correlates with the discharge amplitude, as can be seen in Table 6.3. For the repeated 90 V (8100 nJ) experiments (1, 4-5), the sample mean for number of discharges to failure is 18.9 billion. At the 80% confidence level, the number of discharges to failure for 90V discharges is 18.9 billion ± 4.1 billion (±~20%).

To observe the vibration harmonics generated by the EDM discharges in the various bearings tested, the discrete Fourier transform (DFT) is computed for the time domain piezo vibration signals. The DFT for experiment no. 1, the first 90 V (8100 nJ)

discharge test, can be seen in Fig. 6.5. In general, for all experiments conducted, as EDM discharges cause damage to the race and ball surfaces, harmonics develop in the vibration signal in the range of 1-5 kHz due to the fluting that develops on the inner and outer race surfaces. The specific frequencies at which the harmonics appear depend on the number of flutes and their locations on the race surfaces. Since the piezo vibration sensor was attached to the bearing testbed pillow block, the sensor primarily picks up the f_{bpo} frequency, which is 90 Hz and its multiples. Therefore, the harmonics that appear in the vibration signal are due to flutes generated by the EDM discharges, and the harmonics in the 1-5 kHz range are spaced by 90 Hz each.

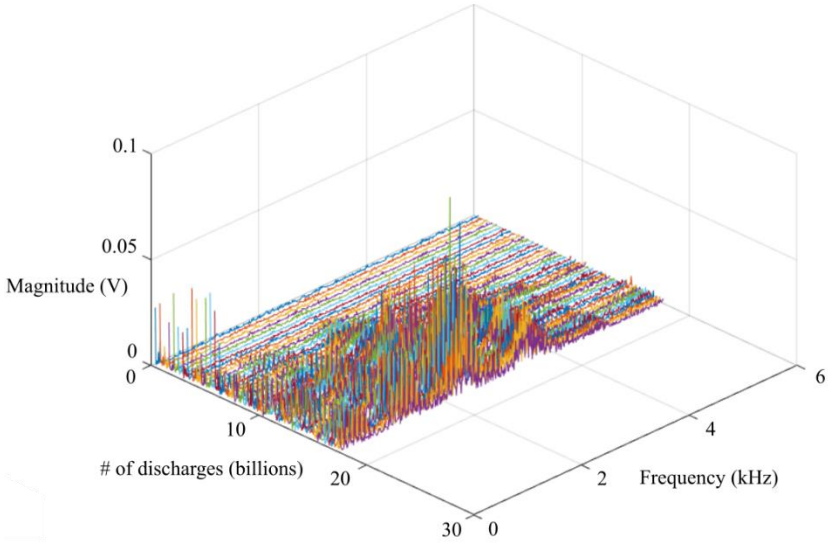

Figure 6.5. DFT of the piezo vibration sensor electrical signal over the course of the first 90 V (8100 nJ) discharge experiment (experiment no. 1).

Analysis

In Fig. 6.6, the discharge energy is plotted against the number of discharges to failure. A line of best fit using the sample mean for the three 90 V experiments is shown in orange. For this analysis, it is assumed that the number of discharges to failure results

for the 80 V and 70 V experiments are the sample mean for that particular discharge energy, and that the true mean will fall within ±20% percent of that value, like it did for the 90 V experiments. Therefore, additional lines (yellow, purple) of best fit located at ±20% of the sample means are added to the plot of Fig. 6.6. The area between these two lines describes the 80% confidence interval of the true mean number of discharges to failure. The lines of best fit can be extrapolated down into the discharge energy region that is typical for the 5 hp motors considered in this research. From Chapters Four and Five, the smallest amplitude EDM discharge that causes damage is between 4-5V, which is 17 nJ for a 4 V discharge. The largest amplitude of EDM discharges seen on 5 hp motors driven by PWM inverters is 35 V, which is 1340 nJ. These two boundaries are marked with a grey box in Fig. 6.6, and the region between them describes the potential discharge energies that can occur, which follow the inverse Gaussian distributions of Chapter Five. The lines of best fit in Figure 6.6 are detailed in Table 6.4, where *m* and *b* are the fit slope and y-intercept, respectively. The dependent variable (number of discharges) is in billions, while the independent variable (discharge energy) is in nJ.

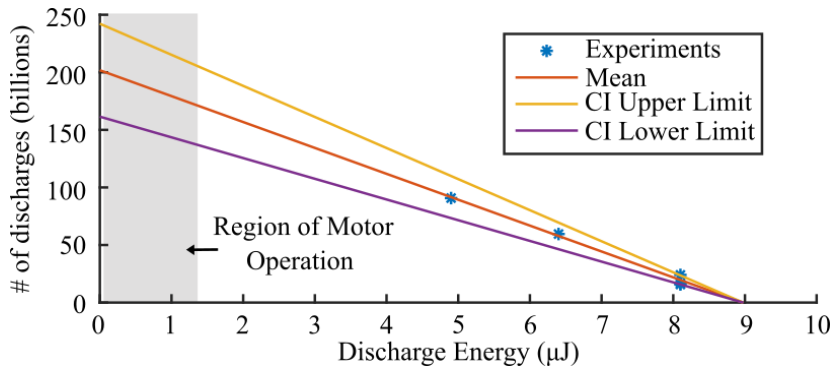

Figure 6.6. Experimental lines of best fit with confidence interval bounds extrapolated down into the region of EDM discharge energy seen on 5 hp motors. The plot shows the number of discharges to failure plotted against the energy of each discharge.

Table 6.4. Lines of best fit for number of discharges to failure given the discharge energy.

Fit	Fit Color (Fig. 6.6)	*m*	*b*
Sample Mean	Orange	-0.02249	201.8
CI Upper Limit	Yellow	-0.02699	242.2
CI Lower Limit	Purple	-0.01799	161.5

For 35 V (1340 nJ) discharges, the extrapolation predicts that a bearing will fail after 171.9 billion discharges, and for 4 V (17 nJ) discharges, the prediction is 201.4 billion discharges, both values of which may vary ±20% to lie within the 80% confidence interval. However, as demonstrated in Chapter Five, the discharge energies do not remain constant, but follow a distribution.

Bearing State of Health

To account for the variable nature of the EDM discharges, a bearing state-of-health metric (SOH) is defined, which attaches a numerical value to the health of the bearing at any point in its lifetime, where a value of 1 indicates a new, healthy bearing and 0 is a failed bearing.

$$SOH = 1 - \sum \frac{10^{-9}}{m d_e + b} \tag{6.5}$$

Here, *m* and *b* are the slope and y-intercept of the line of best fit used in the extrapolation, d_e is the discharge energy, and the 10^{-9} multiplier accounts for the dependent variable unit of the line of best fit being in billions. Using Eq. 6.5, each discharge energy that occurs in the bearing can be summed into the equation, and the SOH can be computed. This value can be used in real time for industrial machine operators to assess the health of their equipment.

Lifetime Prediction for Si and SiC EDM Discharges

Using the experimentally obtained inverse Gaussian probability distribution functions of Chapter Five, a random series of shaft voltage values are generated for several motor operational points: 0 p.u., 0.25 p.u., 0.5 p.u., 0.75 p.u., and 1 p.u. of rated load. The discharge energy can then be calculated from Table 3.4 and Eq. 5.10, and the sequence of discharge energies can be fed into Eq. 6.5 to calculate a bearing's SOH against the number of discharges that have occurred. This can be seen in Fig. 6.7 for the Si inverter. As expected from Fig. 6.6 and Table 6.4, bearings on a PWM inverter-driven motor will last for 161.5-242.2 billion discharges at the 80% confidence interval. The mean sample values are shown in Fig. 6.7 with the 80% confidence interval limits shown in dashed lines, and an inset plot is provided for viewing near the zero SOH point.

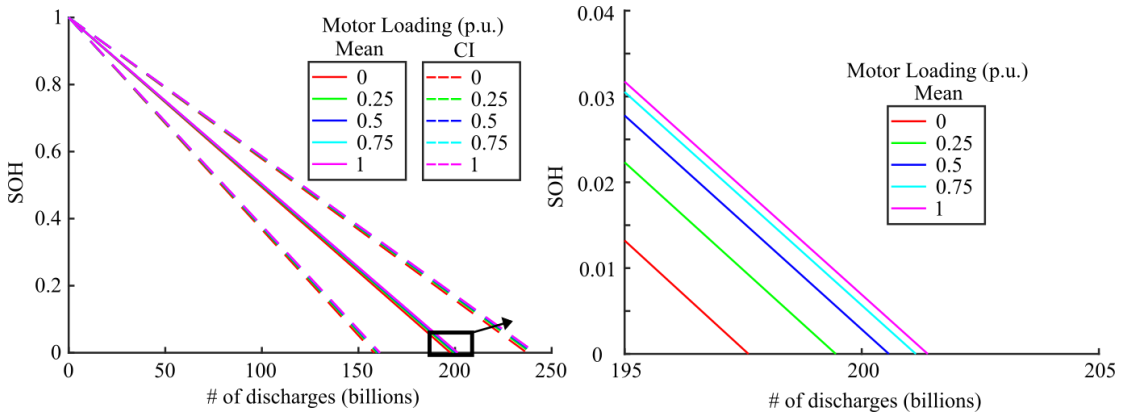

(a) (b)

Figure. 6.7. Bearing SOH lifetime projections for the Si inverter: (a) computed with sample mean values (solid) and 80% confidence interval (dashed) and (b) inset of region below 0.04 SOH.

From Fig. 6.7, the computation predicts that bearings will fail faster due to no/light load motor operation (~197.60 billion discharges) versus full load operation

(~201.43 billion discharges). Although the 80% confidence interval for each of the motor load operational points encloses each sample mean, as shown in Fig. 6.7(a), the prediction of the number of discharges to failure for different motor loads relative to one another remains valid because these SOH curves were computed with the inverse Gaussian distributions. Therefore, bearings will fail faster for no/light load operation compared to rated load operation.

Figure 6.8 shows the comparison between Si and SiC inverter operation. For clarity, the 80% confidence interval upper and lower bounds have been removed from the plot, since a sufficient discussion about their significance has been conducted above.

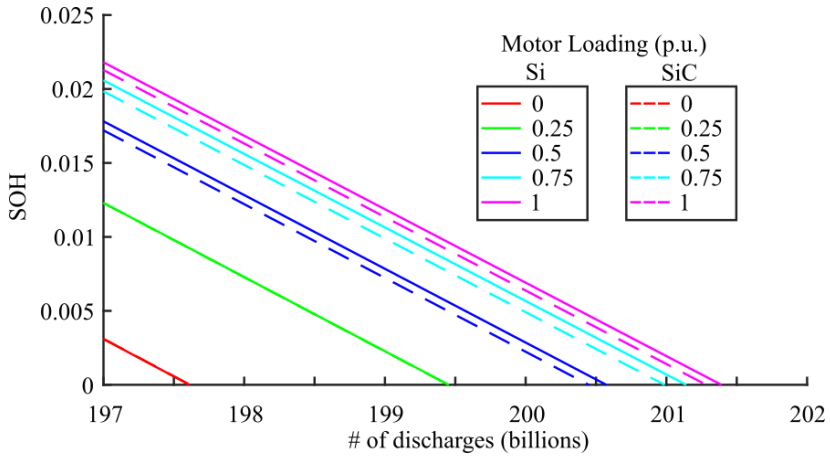

Figure. 6.8. Bearing SOH lifetime projections for the Si and SiC inverters.

The results from Fig. 6.8 indicate that no difference in bearing lifetime between Si and SiC inverters occurs for 0 p.u. and 0.25 p.u. of rated load motor operation, while the difference in lifetime increases with an increase in motor load, especially at loads $\geq$ 0.5 p.u. This is due to a high similarity between the Si and SiC shaft discharge voltage inverse Gaussian distributions for 0 p.u. and 0.25 p.u. of rated motor load operation, and large differences between the distributions occurring for motor loads $\geq$ 0.5 p.u.

Therefore, the slight differences in bearing lifetime between Si and SiC inverter operation can be attributed to pulsed dielectric theory.

From Fig. 6.7 and 6.8, it can be concluded that motor loading contributes to differences in bearing lifetime more than the semiconductor device used. However, this conclusion is obtained by comparing Si and SiC devices independent of inverter switching frequency, which will now be considered.

Time to Failure

To connect the bearing lifetime to a certain duration in the time domain, the switching frequency of the inverter is required. Given the number of discharges to bearing failure, the time to bearing failure can be calculated as follows:

$$t_{days} = \frac{n}{\alpha f_s} \cdot \frac{1}{24} \cdot \frac{1}{3600} \tag{6.6}$$

Here n is the number of discharges to failure, f_s is the inverter switching frequency, α is a temperature coefficient that alters the switching frequency value, and the remaining constants are for unit conversion. From Fig. 5.17, α ranges from 0.6-1.2, where α = 1.2 at no/light load conditions and α = 0.8 at full load conditions. Given this relationship, Table 6.5 gives lifetime projections for motor bearings at various switching frequencies for no load and full load conditions driven by the SiC inverter.

Table 6.5. Motor bearing lifetime projections for SiC inverter operation at various inverter switching frequencies.

f_s (kHz)	Motor Load (p.u.)	α	n_{SiC} (billions)	t_{days}	CI: ± t_{days}	t_{years}
2	0	1.2	197.60	953	191	2.61
2	1	0.8	201.25	1455	291	3.98
10	0	1.2	197.60	190	38	0.52
10	1	0.8	201.25	291	58	0.80
20	0	1.2	197.60	95	19	0.26
20	1	0.8	201.25	146	29	0.40
100	0	1.2	197.60	19	4	0.05
100	1	0.8	201.25	29	6	0.08

A confidence interval calculation is given in days to demonstrate the window for which the prediction is expected to be accurate. The time to failure is linearly proportional to the inverter switching frequency. Changing the load from 0 p.u. to 1 p.u. of rated power increases the lifetime by a factor of 1.53. Therefore, industrial motor operators can expect the longest lifetimes from their bearings when operated at or near full load and with a low switching frequency.

Conclusions

This chapter presented a lifetime projection model for motor bearings subject to EDM bearing currents. Experimental evidence demonstrated that the number of EDM discharges to bearing failure depends on the energy of each discharge that occurs. Bearing failure can be defined using ISO10816-1. Conducting experiments at high discharge energies enabled timely laboratory results. The obtained data was then extrapolated down into the discharge energy region that is typical for PWM inverter-driven motors using a line of best fit. Considering that extrapolation of data is generally less reliable than interpolation, a confidence interval statistic was integrated into the

model to give a sense of the certainty of its claims. From this a SOH metric was defined that gives a real time numerical value for the health of the bearing, where each discharge that occurs slightly degrades the bearing health. Using the inverse Gaussian distribution results from Chapter Five, SOH curves were computed for various conditions. The results indicate that bearing lifetime is positively correlated to motor loading, and that SiC inverters will cause bearing failure slightly faster than Si inverters at motor loads ≥ 0.5 p.u., given that all other system parameters are the same. Of course, SiC devices are typically operated at higher switching frequencies than Si devices, and when this is the case motor bearings will fail much faster, as was demonstrated in Table 6.5, where integration of the inverter switching frequency into the analysis enabled a calculation of the bearing lifetime in the time domain. The results demonstrated that the time to failure is linearly dependent on the inverter switching frequency and that changing the load from 0 p.u. to 1.0 p.u. increases the bearing lifetime by a factor of 1.53. In summary, three predominant motor drive variables were compared and the significance of each as they relate to bearing lifetime in order from greatest impact to smallest impact are: inverter switching frequency, motor loading level, and the semiconductor device type. The switching frequency's large impact is due to the number of discharges that it produces, while the motor loading level and semiconductor device type shift the inverse Gaussian distributions towards higher discharge energy amplitudes for lighter loads and SiC devices, respectively. The effects of motor speed as set by the PWM inverter on bearing lifetime were not included in this study. The reasons for this are demonstrated in Fig. 6.9, where bearing current measurements were made over various motor speeds and temperatures. The changes in bearing current for differences in temperature are clearly

much greater than the changes in bearing current for differences in motor speed, especially in the region of motor speeds greater than 1000 RPM (0.55 p.u.), where the motor rated speed is 1800 RPM. Since the changes in motor temperature for the same operational speed is due to motor loading, it can be concluded that motor loading will have a larger impact on bearing lifetime than motor speed. Additionally, industrial motors will typically be operated above 0.55 p.u., so the effects of motor speed on bearing lifetime will be negligible compared to motor loading. However, for applications such as electric vehicle motors where low speed operation is much more common, the effects motor speed has on bearing lifetime due to EDM discharges may be relevant, such as during city vs. highway driving. However, this remains outside the scope of this dissertation and will be a topic for future work.

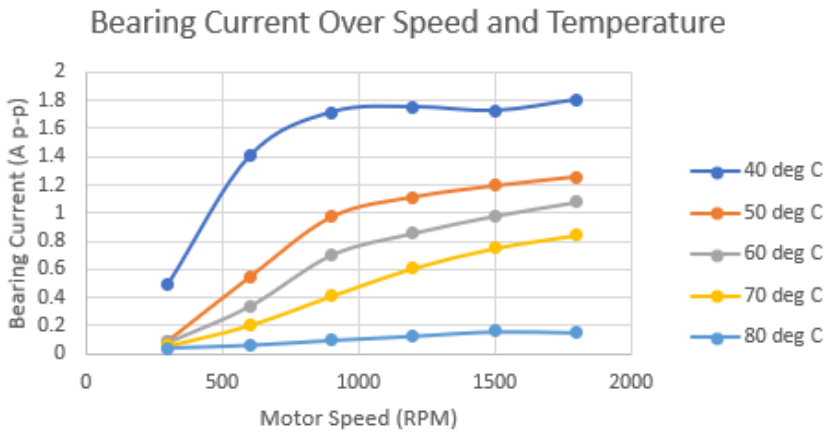

Figure. 6.9. Average bearing current for changes in motor speed and bearing temperature. One hundred samples were performed at each operating point indicated with a dot.

CHAPTER SEVEN

Conclusions

This dissertation explored the effects of both Si and SiC PWM inverters on motor bearing health through the development of intricate EDM discharge circuit models and a damage assessment FE model, characterized Si- and SiC-based EDM bearing currents, and analyzed bearing degradation trends due to EDM bearing currents through an experimental investigation. A summary of the dissertation's contributions as well as paths forward for future work will be given in this concluding chapter.

Key Contributions

This section highlights the key contributions of each chapter of this dissertation in a summarized form.

Chapter Two

In Chapter Two, a SiC-based TLSS inverter motor drive was developed in an RCP manner. RCP using HIL systems for power electronics are continually on the rise in the literature, and the work presented here contributes to the body of research demonstrating this prototyping method's timely and effective implementation.

Chapter Three

To the author's knowledge, Chapter Three provides the most detailed and in-depth circuit modeling analysis to date on EDM bearing currents using experimentally measured circuit parasitic component values obtained with a VNA. The modeling

approach taken exposes the key parasitics that have the largest effect on EDM activity and demonstrates the effects of the measurement wire inductance.

Chapter Four

Chapter Four presented an FE model that can accurately predict mechanical damage on a bearing ball or race given a specific discharge profile, where the discharge profiles from Chapter Three were employed. Various discharge amplitude experiments were conducted and upon the bearings being cut open, the FE model was validated through a statistical imaging process.

Chapter Five

In Chapter Five, an analysis was conducted connecting the rectifier and inverter CM voltage to the shaft discharge voltage and EDM bearing current. Then, a novel statistical approach was taken to characterize Si- and SiC- shaft voltages and bearing currents using inverse Gaussian probability density functions. By connecting the BVR theory with the pulsed dielectric theory, and explanation was given for the cause of larger shaft voltages and EDM bearing currents from SiC inverters.

Chapter Six

The most precise and in-depth experimental tests to date were performed linking the number of EDM discharges to failure with the EDM discharge energy. From this, lines of best fit were generated with confidence intervals to extrapolate down into discharge energy levels typically seen on motors driven by PWM inverters. A SOH metric was developed that degrades each time a discharge occurs, and from this the lifetime of the bearing can be projected. The time to bearing failure was predicted by

including the inverter switching frequency in the analysis. The methods presented here provide a valuable tool for industrial motor predictive maintenance. It was concluded that the three predominant motor drive variables that significantly impact bearing lifetime in order from greatest impact to smallest impact are: inverter switching frequency, motor loading level, and the semiconductor device type.

Future Work

Given the work presented here, the following is recommended for future research and exploration:

- Using the probability density function analysis as a tool, various types and power levels of motors can be compared to understand which types of motors are most susceptible to bearing failure from EDM bearing currents.
- The bearing grease is the most convenient component to modify to improve bearing performance by limiting the EDM discharge energy. Although many conducting greases exist on the market at the time of writing, further research is needed for their development, especially for motors driven by SiC inverters.
- FE modeling demonstrated that the measurement wire inductance can reduce the EDM damage on the races of a bearing. By optimizing this impedance, EDM damage can be minimized while still allowing the shaft to discharge. Further research into this area has the potential to produce valuable intellectual property.
- Given that journal bearings (10,000's+ of hp) and roller bearings (300's – 1000's of hp) are used in larger motors, where ball bearings are used in

applications in the 100’s of hp range, keeping the bearings operational is imperative to prevent economic loss. The methods presented in this dissertation can be applied to journal bearings and roller bearings, improving their reliability in critical applications.

APPENDICES

APPENDIX A

Script to Read Thermistor Temperature

This MATLAB script is the main looping script used to collect oscilloscope shaft voltage and bearing current data on the machine testbed. Starting with 30°C and increasing to 60°C, data is recorded at each degree increment. Thermistors are used for the temperature sensing, attached to the outer races of the motor's bearings. To convert the Arduino analog input reading into a temperature, the following relation is used:

$$T = \frac{1}{\frac{1}{T_0}+\frac{1}{B}\log\left(\frac{R_{th}}{R_{th0}}\right)} \quad \text{(A.1)}$$

In Eq. (A.1), T is the thermistor temperature in K, T_0 is room temperature in K, B is the thermistor's beta value, a constant that describes the thermistor's nonlinear relationship between temperature and resistance, R_{th} is the thermistor resistance of interest, and R_{th0} is the thermistor's resistance at room temperature. The thermistor resistance is calculated by using a voltage divider technique at the microcontroller's analog input.

```
clear;
clc;
close all

% setup digital inputs
heating_pad_1 = 'D2';
heating_pad_2 = 'D3';
thermistor_1 = 'D8';
thermistor_2 = 'D9';

% arduino variables
v_dig = 5;              % digital pin voltage
Rt_1 = 0;               % initialize var for thermistor_1 resistance
Rt_2 = 0;               % initialize var for thermistor_2 resistance
v_1 = 0;                % var to store thermistor voltage
v_2 = 0;                % var to store thermistor voltage
temperature_1 = 0;
temperature_2 = 0;
B = 3950;               % B value
T0 = 295;               % Room temp

R_1 = 99500;            % Resistance in series with thermistor_1
Rt_1_0 = 110000;        % Resistance of thermistor 1 at room temp
R_2 = 100000;           % Resistance in series with thermistor_2
```

```
Rt_2_0 = 110000;        % Resistance of thermistor 2 at room temp

% setup arduino object
port = 'COM4';
board = 'Uno';

a = arduino(port, board);
load gong
pause(1);
% set up matrices to collect shaft voltage and bearing current data at each temperature
vdata = zeros(31,10000000);
idata = zeros(31,10000000);
k = 30;  % start at 30 deg C and go to 60 deg C

while(1)

    % acquire the bearing temperatures and setpoint
    % turn on thermistor for measurement, wait for voltage to rise
    a.writeDigitalPin(thermistor_1, 1);
    pause(0.1);

    % read analog pin voltage and back out thermistor resistance
    v_1 = readVoltage(a,'A1');
    Rt_1 = (v_1/(v_dig-v_1))*R_1;

    % now use Rt_1 to find temp in deg C
    temperature_1 = 1/((1/T0)+(1/B)*log(Rt_1/Rt_1_0)); % in Kelvin
    temperature_1 = temperature_1 - 273.15;

    % turn off thermistor
    a.writeDigitalPin(thermistor_1, 0);

    % turn on thermistor for measurement, wait for voltage to rise
    a.writeDigitalPin(thermistor_2, 1);
    pause(0.1)

    % read analog pin voltage and back out thermistor resistance
    v_2 = readVoltage(a,'A2');
    Rt_2 = (v_2/(v_dig-v_2))*R_2;

    % now use Rt_2 to find temp in deg C
    temperature_2 = 1/((1/T0)+(1/B)*log(Rt_2/Rt_2_0)); % in Kelvin
    temperature_2 = temperature_2 - 273.15;

    % turn off thermistor
    a.writeDigitalPin(thermistor_2, 0);

    if(temperature_1 > k)
        a.writeDigitalPin(heating_pad_1, 0); % turn heater off
        a.writeDigitalPin(heating_pad_2, 0); % turn heaters off
    elseif(temperature_1 < k)
        a.writeDigitalPin(heating_pad_1, 1); % turn heater on
        a.writeDigitalPin(heating_pad_2, 1); % turn heater on
    else
         % do nothing
    end

    fprintf('Bearing 1 Temperature: %d\n', temperature_1);
    fprintf('Bearing 2 Temperature: %d\n', temperature_2);
    fprintf('Temperature Setpoint: %d\n', k);

    % check to see if data needs to be recorded
    if temperature_1 > k
        % record data
        [vdata((k-29),:), idata((k-29),:)] = getSVBCdata_twochannel();
        % go to next temperature iteration
        sound(y,Fs)
        k = k+1;
    end

    if (k > 60)
```

```
        % end the experiment
        break
    end

    pause(1);

end

fprintf('Experiment Complete!\n')
a.writeDigitalPin(heating_pad_1, 0); % turn heater 1 off
a.writeDigitalPin(heating_pad_2, 0); % turn heater 2 off
```

APPENDIX B

Shaft Voltage and Bearing Current Data Collection Script

In Appendix A, the function `getSVBCdata_twochannel()` was called to collect and transfer MDO3014 oscilloscope shaft voltage and bearing current waveform data to a connected PC. The script that makes up that function is shown here in Appendix B. The maximum record length of the oscilloscope was utilized at 10M data points per channel, and the horizontal scale of the oscilloscope was set to 20 ms/div. This gives a data sampling rate of 50 MHz, and considering that EDM discharge frequencies are as high as 10 MHz, this sampling rate satisfies the Nyquist sampling criterion:

$$2f_{EDM} < f_s \tag{B.1}$$

where f_{EDM} is the highest frequency EDM discharge and f_s is the oscilloscope sampling rate. The data is then saved in the MATLAB workspace for further processing and analysis.

```
function [v1, i1] = getSVBCdata_twochannel()

% notes about code operation
% commands modify oscilloscope settings or tell the scope to perform a
% specific action
% queries cause the scope to return data and status information

% most commands have a set form and a query form. the query form of the
% command has a question mark at the end. some commands have set only and
% some have query only

% Parameters to set
horizscale = 20e-3;         % 20 ms/div
record = 10e6;              % 10M data points
% CH1 settings
CH1_v_div = 10;             % CH1 V/div
CH1_pos = 0;                % CH1 position
trig_level = 10;            % trigger position
% CH2 settings
CH2_v_div = 500e-3;
CH2_pos = 0;

% user inputs
visa_vendor = 'ni';
```

```
visa_addr = 'USB0::0x0699::0x0408::B020704::INSTR';

scope = visa(visa_vendor, visa_addr); % create the scope object
scope.InputBufferSize = 10e6;   % total size of the input buffer, must be >= size of
vector to be collected
fopen(scope); % connects the object scope to the instrument

fprintf(scope, '*cls'); % clears the scope (ESR)
ID = query(scope, '*idn?'); % request and store the scope ID
fprintf('Connected to: %s', ID);

fprintf(scope, '*rst'); % reset scope
query(scope, '*opc?'); % synchronize the operation of the scope with application program.
Returns 1 when all commands are complete

% set up the horizontal time/div and record length
fprintf(scope, 'horizontal:scale %d', horizscale); % set the horizontal scale of the
scope
fprintf(scope, 'horizontal:recordlength %d', record); % set the record length

% set up Channel 1
fprintf(scope, 'CH1:scale %d', CH1_v_div); % set the CH1 volts/div
fprintf(scope, 'CH1:position %d', CH1_pos); % specifies the channel offset
fprintf(scope, 'fpanel:turn triglevel, %d', trig_level);

% set up Channel 2
fprintf(scope, 'fpanel:press CH2'); % turn on CH2
fprintf(scope, 'CH2:scale %d', CH2_v_div); % set the CH2 volts/div
fprintf(scope, 'CH2:position %d', CH2_pos); % specifies the channel offset
fprintf(scope, 'CH2:coupling AC'); % use AC coupling

%%%%%%%%%%%%%%%%%%%%%%%%%%%%%%%%%%%%%%%%%%%%%%%%%%%%%%%%%%%%%%%%%%%%%%%%%%%%%%%
% io config, configure the scope setting, set up to collect from CH1

fprintf(scope, 'data:source CH1'); % channel selection

fprintf(scope, 'header 0'); % turns off the header
fprintf(scope, 'data:encdg SRIBINARY'); % specifies the encoding format for outgoing
waveform data (in this case signed integer)
fprintf(scope, 'data:source CH1'); % channel selection
fprintf(scope, 'data:start 1'); % first sample
fprintf(scope, 'data:stop %d', record); % last sample
fprintf(scope, 'wfmoutpre:byt_nr 1'); % 1 byte per sample

% acq config
fprintf(scope, 'acquire:state 0'); % stop, make sure it is off
fprintf(scope, 'acquire:stopafter SEQUENCE'); % single sequence acquisition mode
fprintf(scope, 'acquire:state 1'); % acquire aquisition on screen
query(scope, '*opc?'); % allow things to sync

% retrieve scaling factors
vscale = str2double(query(scope, 'wfmoutpre:ymult?')); % volts / level
voff = str2double(query(scope, 'wfmoutpre:yoff?')); % vertical position of the source
waveform in digitizing units (digitizing levels per vertical division)

% get waveform data
fprintf(scope, 'curve?'); % transfers data from the oscilloscope
v1 = (vscale * (binblockread(scope, 'int8') - voff))'; % with 8 bit precision

% error checking
r = query(scope, '*esr?'); % returns the contents of the standard event status register
%fprintf('event status register: 0b%x\n', r);
r = query(scope, 'allev?'); % prompts the scope to return all events and their messages
%fprintf('all event messages: 0b%x\n', r);

% CH1 collection complete
%%%%%%%%%%%%%%%%%%%%%%%%%%%%%%%%%%%%%%%%%%%%%%%%%%%%%%%%%%%%%%%%%%%%%%%%%%%%%%%

% io config, configure the scope setting, set up to collect from CH2

fprintf(scope, 'data:source CH2'); % channel selection
```

```
% retrieve scaling factors
iscale = str2double(query(scope, 'wfmoutpre:ymult?')); % volts / level
ioff = str2double(query(scope, 'wfmoutpre:yoff?')); % vertical position of the source
waveform in digitizing units (digitizing levels per vertical division)

% get waveform data
fprintf(scope, 'curve?'); % transfers data from the oscilloscope
i1 = (iscale * (binblockread(scope, 'int8') - ioff))'; % with 8 bit precision

% error checking
r = query(scope, '*esr?'); % returns the contents of the standard event status register
%fprintf('event status register: 0b%x\n', r);
r = query(scope, 'allev?'); % prompts the scope to return all events and their messages
%fprintf('all event messages: 0b%x\n', r);

% CH2 collection complete
%%%%%%%%%%%%%%%%%%%%%%%%%%%%%%%%%%%%%%%%%%%%%%%%%%%%%%%%%%%%%%%%%%%%%%%%%%%%%%%

% gracefully close visa session
fclose(scope);
delete(scope);
clear scope;

end
```

APPENDIX C

Bearing Testbed Temperature Control Script

This script controls the temperature of the bearing in the Bearing Testbed. A similar approach is taken with a thermistor as was implemented on the Machine Testbed. An LCD display is used to display the current temperature as well as the temperature setpoint.

```
#include <LiquidCrystal_I2C.h>

int ThermistorPin = 1;
float temp_setpoint = 60;
float error, abs_error;
int sensorValue;
float Rt, TK, TC, v;
float B = 3950, T0 = 295, R1 = 100000;

LiquidCrystal_I2C lcd(0x27, 16, 2);

void setup() {
  pinMode(8, OUTPUT);
  pinMode(5, OUTPUT); // this controls the fan
  pinMode(6, OUTPUT); // this controls the heater
  digitalWrite(5, HIGH); // turn off the fan
  digitalWrite(6, HIGH); // turn off the heater
  lcd.init();
  lcd.backlight();
  lcd.setCursor(0,1);
  lcd.print("Setpoint = ");
  lcd.print(temp_setpoint);
  lcd.print(" C");
}

void loop() {

  // get bearing temperature
  digitalWrite(8, HIGH);
  delay(20);
  sensorValue = analogRead(ThermistorPin);
  digitalWrite(8, LOW);
  v = sensorValue * (5.0 / 1023.0);
  Rt = (v/(5 - v))*R1;
  TK = 1/((1/T0)+(1/B)*log(Rt/R1)); // in Kelvin
  TC = TK - 273.15;
  lcd.setCursor(0,0);
  lcd.print("Temp = ");
  lcd.print(TC);
  lcd.print(" C");

  error = temp_setpoint - TC;
  // positive error, temp to low.
  abs_error = abs(error);

  if (abs_error > 50)
```

```
 {
  // thermistor became disconnected deenergize
  digitalWrite(5, HIGH); // turn off the fan
  digitalWrite(6, HIGH); // turn off the heater
 }

 if ((error > 0) && (error < 50))
 {
  digitalWrite(5, LOW); // turn on the fan
  digitalWrite(6, LOW); // turn on the heater
 }

 if (error < -3)
 {
  // give the temp a 3 degree window
  digitalWrite(5, HIGH); // turn off the fan
  digitalWrite(6, HIGH); // turn off the heater
 }

 delay(3000);
}
```

APPENDIX D

Bearing Testbed Discharge Control Script

A state machine was developed to control the discharges to the bearing under test on the bearing testbed. In state 1, the script is waiting for a user input of a button press to begin executing discharges. During state 2, MOSFET Q1 of Fig. 2.17 is pulsed on to charge the capacitor, and then turned off. Then, Q2 is turned on and the state transitions forward to state 3. Here, the MCU waits for confirmation from the op-amp sensing circuitry that a discharge has occurred. When achieved, a discharge counter is incremented, and then the process returns to state 2. Occasionally, the value is printed to the serial monitor to notify the user of the number of discharges. An additional user button is used to terminate the experiment. Finally, an overflow counter is used to track overflow conditions on the discharge counter to ensure accurate results.

```
unsigned long counter = 0;
int counter_overflow = 0;
unsigned long display_counter = 0;
int state = 1;
int next_state = 1;
bool discharge = false;
int op_amp_pin = 5;
int switch_1 = 3;
int switch_2 = 4;
int buttonPin = 12;
bool button_val;

// Setup //
void setup()
{
  pinMode(buttonPin, INPUT_PULLUP); // Define pin #12 as input and activate the internal pull-up resistor
  pinMode(op_amp_pin, INPUT); // this pin will be high when discharge has occurred, low when voltage still present on cap
  pinMode(switch_1, OUTPUT); // switch 1 will charge the cap
  pinMode(switch_2, OUTPUT); // switch 2 will enable the cap to discharge through the bearing

    //Initialize serial and wait for port to open:
  Serial.begin(9600);
  while (!Serial)
  {
    ; // wait for serial port to connect. Needed for native USB
  }
  Serial.println("Press Button To Begin");
}
```

```
// Main Loop //
void loop()
{
  switch (state)
  {
    case 1:
      button_val = digitalRead(buttonPin);
      if (button_val == LOW)
      {
        next_state = 2;
        delay(1000);
      }
      break;

    case 2:
      // here a pulse will be sent to switch 1 to charge the capacitor
      digitalWrite(switch_1, HIGH);
      delayMicroseconds(2);
      digitalWrite(switch_1, LOW);
      // turn on switch 2, and wait for discharge to occur
      digitalWrite(switch_2, HIGH);
      next_state = 3;
      break;

    case 3:
      // op_amp_pin will be low once the discharge has occurred
      discharge = digitalRead(op_amp_pin);
      if (discharge == LOW)
      {
        counter++;
        if (counter > 4000000000)
        {
          counter = 0;
          counter_overflow++;
        }
        display_counter++;
        digitalWrite(switch_2, LOW); // turn off switch 2 in preparation for cap charge
        next_state = 4;
      }
      break;

    case 4:
      if (display_counter > 9999999)
      {
        display_counter = 0; // reset the variable
        // print the value of the discharges to the serial port
        Serial.print("Number of Discharges: ");
        Serial.println(counter);
        Serial.print("Number of Times Counter Overflowed: ");
        Serial.println(counter_overflow);
      }

      // go back to state 1, send the pulse, repeating the process
        next_state = 2;


      button_val = digitalRead(buttonPin);
      // check if button is pressed, this will end the experiment
      if (button_val == LOW)
      {
        next_state = 5; // end the experiment. print value to screen then go to while(1) loop
        Serial.print("Number of Discharges: ");
        Serial.println(counter);
        Serial.print("Number of Times Counter Overflowed: ");
        Serial.println(counter_overflow);
        Serial.println("Experiment Complete");
      }

      break;
```

```
    case 5:
    while(1)
    {
     ;
    }
    break;

  }

  state = next_state;

}
```

APPENDIX E

Algorithm to Extract Shaft Discharge Voltage and Peak Apparent Bearing Current

This MATLAB script processes the shaft voltage and bearing current waveform data from the oscilloscope, extracting the peak apparent bearing current and the shaft discharge voltage. The function looks for local maximums in the bearing current waveform, and then finds the shaft discharge voltage amplitude associated with that particular local maximum of the bearing current waveform.

```
function [peakt, peakv, peaki] = get_peaks(vwave, iwave)

kfinal = length(iwave);
k = 0:1:kfinal-1;
fsamp = 50e6;
tstep = 1/fsamp;
tfinal = tstep*kfinal;
t = 0:tstep:tfinal-tstep;

v = abs(vwave); % take the absolute value so we can find the local maximums
i = abs(iwave);

TF = islocalmax(i,'MinSeparation',80,'SamplePoints',k); % by trial and error it was found
that a % min separation of 80 between local maximums avoided recording of the follow on
oscillations but % didn't disregard the next discharge event.
maxt = k(TF); % this gives element number from the i vector where a local maximum was
found
maxi = i(TF); % this gives the peak apparent bearing current amplitude at each local max
peaki = zeros(kfinal,1);
peakt = zeros(1,kfinal);
n = 1;
for j=1:length(maxt)
    if maxi(j)>0.05 % collect only the current peaks that are > 50 mA, which is above %
noise/displacement current level.
        peaki(n)=maxi(j);
        peakt(n)=maxt(j);
        n=n+1;
    end
end
peaki = peaki(1:n-1); % trim off the remaining zeros from the vector
peakt = peakt(1:n-1);

% figure
% plot(k,i,peakt,peaki,'r*') % this line plots the waveform with the extracted values
overlain,  % providing a visual tool to verify the algorithm

peakv = zeros(kfinal,1); % now get the shaft voltage associated with the current local
max
n = 1;
for j=1:length(peakt)
    w = peakt(j);
    peakv(n)= max(v((w-20):w)); % the shaft discharge voltage is within 20 elements of
the       % current local max
    n = n+1;
end
```

```
peakv = peakv(1:n-1); % trim off the remaining zeros from the vector

end
```

REFERENCES

[1] A. Bonnett, "Root Cause Methodology for Induction Motors: A Step-by-Step Guide to Examining Failure," *IEEE Industry Applications Magazine,* vol. 18, no. 6, pp. 50-62, 2012, doi: 10.1109/mias.2012.2208487.

[2] S. Nandi, H. A. Toliyat, and X. Li, "Condition Monitoring and Fault Diagnosis of Electrical Motors—A Review," *IEEE Transactions on Energy Conversion,* vol. 20, no. 4, pp. 719-729, 2005, doi: 10.1109/tec.2005.847955.

[3] P. J. Zhang, Y. Du, T. G. Habetler, and B. Lu, "A Survey of Condition Monitoring and Protection Methods for Medium-Voltage Induction Motors," *Ieee Transactions on Industry Applications,* vol. 47, no. 1, pp. 34-46, Jan-Feb 2011, doi: 10.1109/tia.2010.2090839.

[4] R. Electric, "Avoiding Motor Shaft Voltage & Bearing Current Damage," [Online], 2018. [Online]. Available: https://www.magnetec.de/fileadmin/pdf/bearing-current-damage-guide.pdf

[5] P. L. Alger and H. W. Samson, "Shaft Currents in Electric Machines," *Transactions of the American Institute of Electrical Engineers,* vol. XLIII, pp. 235-245, 1924, doi: 10.1109/T-AIEE.1924.5060981.

[6] A. Muetze, "Bearing Currents in Inverter-Fed AC-Motors," PhD, Darmstadt University of Technology, Shaker Verlag, Aachen, 2004.

[7] J. M. Erdman, R. J. Kerkman, D. W. Schlegel, and G. L. Skibinski, "Effect of PWM inverters on AC motor bearing currents and shaft voltages," *IEEE Transactions on Industry Applications,* vol. 32, no. 2, pp. 250-259, 1996, doi: 10.1109/28.491472.

[8] H. Prashad, "Theoretical Analysis of Capacitive Effect of Roller Bearings on Repeated Starts and Stops of a Machine Operating Under the Influence of Shaft Voltages," *Journal of Tribology,* vol. 114, no. 4, pp. 818-822, 1992, doi: 10.1115/1.2920954.

[9] S. Ogasawara and H. Akagi, "Modeling and damping of high-frequency leakage currents in PWM inverter-fed AC motor drive systems," *IEEE Transactions on Industry Applications,* vol. 32, no. 5, pp. 1105-1114, 1996, doi: 10.1109/28.536872.

[10] A. Muetze and A. Binder, "Calculation of Motor Capacitances for Prediction of the Voltage Across the Bearings in Machines of Inverter-Based Drive Systems," vol. 43, no. 3, pp. 665-672, 2007, doi: 10.1109/tia.2007.895734.

[11] D. Busse, J. Erdman, R. J. Kerkman, D. Schlegel, and G. Skibinski, "System electrical parameters and their effects on bearing currents," *IEEE Transactions on Industry Applications,* vol. 33, no. 2, pp. 577-584, 1997, doi: 10.1109/28.568025.

[12] Z. Haoran, "Investigation and Mitigation of the Adverse Effects of PWM Adjustable Speed Drives," PhD, School of Electrical Engineering and Computer Science, Oregon State University, Corvallis, Oregon, 1998.

[13] S. Chen, T. A. Lipo, and D. Fitzgerald, "Source of induction motor bearing currents caused by PWM inverters," *IEEE Transactions on Energy Conversion,* vol. 11, no. 1, pp. 25-32, 1996, doi: 10.1109/60.486572.

[14] M. Jaritz, C. Jaeger, M. Bucher, J. Smajic, D. Vukovic, and S. Blume, "An Improved Model for Circulating Bearing Currents in Inverter-Fed AC Machines," in *2019 IEEE International Conference on Industrial Technology (ICIT),* 13-15 Feb. 2019 2019, pp. 225-230, doi: 10.1109/ICIT.2019.8755123.

[15] T. Plazenet, T. Boileau, C. Caironi, and B. Nahid-Mobarakeh, "An overview of shaft voltages and bearing currents in rotating machines," in *2016 IEEE Industry Applications Society Annual Meeting*, 2-6 Oct. 2016 2016, pp. 1-8, doi: 10.1109/IAS.2016.7731884.

[16] A. Muetze and A. Binder, "Calculation of Circulating Bearing Currents in Machines of Inverter-Based Drive Systems," *IEEE Transactions on Industrial Electronics,* vol. 54, no. 2, pp. 932-938, 2007, doi: 10.1109/TIE.2007.892001.

[17] J. A. Oliver, G. Guerrero, and J. Goldman, "Ceramic Bearings for Electric Motors: Eliminating Damage with New Materials," *IEEE Industry Applications Magazine,* vol. 23, no. 6, pp. 14-20, 2017, doi: 10.1109/mias.2016.2600692.

[18] A. Binder and A. Muetze, "Scaling Effects of Inverter-Induced Bearing Currents in AC Machines," *IEEE Transactions on Industry Applications,* vol. 44, no. 3, pp. 769-776, 2008, doi: 10.1109/tia.2008.921378.

[19] H. E. Boyanton and G. Hodges, "Bearing fluting [motors]," *IEEE Industry Applications Magazine,* vol. 8, no. 5, pp. 53-57, 2002, doi: 10.1109/MIA.2002.1028391.

[20] A. Muetze, A. Binder, H. Vogel, and J. Hering, "What can bearings bear?," vol. 12, no. 6, pp. 57-64, 2006, doi: 10.1109/ia-m.2006.248014.

[21] D. F. Busse, J. M. Erdman, R. J. Kerkman, D. W. Schlegel, and G. L. Skibinski, "The effects of PWM voltage source inverters on the mechanical performance of rolling bearings," *IEEE Transactions on Industry Applications,* vol. 33, no. 2, pp. 567-576, 1997, doi: 10.1109/28.568024.

[22] A. Muetze and A. Binder, "Practical Rules for Assessment of Inverter-Induced Bearing Currents in Inverter-Fed AC Motors up to 500 kW," *IEEE Transactions on Industrial Electronics,* vol. 54, no. 3, pp. 1614-1622, 2007, doi: 10.1109/TIE.2007.894698.

[23] M. Schuster, J. Springer, and A. Binder, "Comparison of a 1.1 kW-induction machine and a 1.5 kW-PMSM regarding common-mode bearing currents," 2018: IEEE, doi: 10.1109/speedam.2018.8445298. [Online]. Available: https://dx.doi.org/10.1109/speedam.2018.8445298

[24] A. Von Jouanne *et al.*, "Motor Bearing Current Characterization in SiC- based Variable Frequency Drive Applications," 2020: IEEE, doi: 10.1109/ecce44975.2020.9235925. [Online]. Available: https://dx.doi.org/10.1109/ecce44975.2020.9235925

[25] O. Magdun, Y. Gemeinder, and A. Binder, "Investigation of influence of bearing load and bearing temperature on EDM bearing currents," 2010: IEEE, doi: 10.1109/ecce.2010.5618061. [Online]. Available: https://dx.doi.org/10.1109/ecce.2010.5618061

[26] M. Schuster, D. Masendorf, and A. Binder, "Two PMSMs and the influence of their geometry on common-mode bearing currents," 2016: IEEE, doi: 10.1109/icelmach.2016.7732816. [Online]. Available: https://dx.doi.org/10.1109/icelmach.2016.7732816

[27] A. Bubert, J. Zhang, and R. W. De Doncker, "Modeling and measurement of capacitive and inductive bearing current in electrical machines," 2017: IEEE, doi: 10.1109/cobep.2017.8257251. [Online]. Available: https://dx.doi.org/10.1109/cobep.2017.8257251

[28] A. Harnoy, *Bearing design in machinery : engineering tribology and lubrication* (Mechanical engineering ; 147). New York: Marcel Dekker (in English), 2003.

[29] M. Kriese, E. Wittek, S. Gattermann, H. Tischmacher, G. Poll, and B. Ponick, "Influence of bearing currents on the bearing lifetime for converter driven machines," 2012: IEEE, doi: 10.1109/icelmach.2012.6350115. [Online]. Available: https://dx.doi.org/10.1109/icelmach.2012.6350115

[30] D. Busse, J. Erdman, R. J. Kerkman, D. Schlegel, and G. Skibinski, "Bearing currents and their relationship to PWM drives," *IEEE Transactions on Power Electronics,* vol. 12, no. 2, pp. 243-252, 1997, doi: 10.1109/63.558735.

[31] O. Magdun, Y. Gemeinder, and A. Binder, "Prevention of harmful EDM currents in inverter-fed AC machines by use of electrostatic shields in the stator winding overhang," 2010: IEEE, doi: 10.1109/iecon.2010.5675498. [Online]. Available: https://dx.doi.org/10.1109/iecon.2010.5675498

[32] V. Hausberg and H. O. Seinsch, "Kapazitive Lagerspannungen und -ströme bei umrichtergespeisten Induktionsmaschinen," *Electrical Engineering (Archiv fur Elektrotechnik),* vol. 82, no. 3-4, pp. 153-162, 2000, doi: 10.1007/s002020050006.

[33] L. L. Alston and G. United Kingdom Atomic Energy Authority. Research, *High-voltage technology* (Harwell post-graduate series). London: Oxford U.P. (in English), 1968.

[34] P. Wang, A. Cavallini, G. C. Montanari, and G. Wu, "Effect of rise time on PD pulse features under repetitive square wave voltages," *IEEE Transactions on Dielectrics and Electrical Insulation,* vol. 20, no. 1, pp. 245-254, 2013, doi: 10.1109/TDEI.2013.6451364.

[35] M. P. Wilson *et al.*, "Effect of applied field and rate of voltage rise on surface breakdown of oil-immersed polymers," *IEEE Transactions on Dielectrics and Electrical Insulation,* vol. 18, no. 4, pp. 1003-1010, 2011, doi: 10.1109/TDEI.2011.5976088.

[36] J. Jadidian, M. Zahn, N. Lavesson, O. Widlund, and K. Borg, "Effects of Impulse Voltage Polarity, Peak Amplitude, and Rise Time on Streamers Initiated From a Needle Electrode in Transformer Oil," *IEEE Transactions on Plasma Science,* vol. 40, no. 3, pp. 909-918, 2012, doi: 10.1109/tps.2011.2181961.

[37] S. Wu, H. Xu, X. Lu, and Y. Pan, "Effect of Pulse Rising Time of Pulse dc Voltage on Atmospheric Pressure Non-Equilibrium Plasma," *Plasma Processes and Polymers,* vol. 10, no. 2, pp. 136-140, 2013, doi: 10.1002/ppap.201200071.

[38] N. Y. Babaeva and G. V. Naidis, "Modeling of Streamer Dynamics in Atmospheric-Pressure Air: Influence of Rise Time of Applied Voltage Pulse on Streamer Parameters," *IEEE Transactions on Plasma Science,* vol. 44, no. 6, pp. 899-902, 2016, doi: 10.1109/tps.2016.2553081.

[39] D. Han, S. Li, W. Lee, W. Choi, and B. Sarlioglu, "Trade-off between switching loss and common mode EMI generation of GaN devices-analysis and solution," in *2017 IEEE Applied Power Electronics Conference and Exposition (APEC)*, 26-30 March 2017 2017, pp. 843-847, doi: 10.1109/APEC.2017.7930794.

[40] N. Tandon and A. Choudhury, "A review of vibration and acoustic measurement methods for the detection of defects in rolling element bearings," *Tribology International,* vol. 32, no. 8, pp. 469-480, 1999/08/01/ 1999, doi: https://doi.org/10.1016/S0301-679X(99)00077-8.

[41] S. Singh, C. Q. Howard, and C. H. Hansen, "An extensive review of vibration modelling of rolling element bearings with localised and extended defects," *Journal of Sound and Vibration,* vol. 357, pp. 300-330, 2015, doi: 10.1016/j.jsv.2015.04.037.

[42] J. R. Stack, T. G. Habetler, and R. G. Harley, "Fault-signature modeling and detection of inner-race bearing faults," *IEEE Transactions on Industry Applications,* vol. 42, no. 1, pp. 61-68, 2006, doi: 10.1109/tia.2005.861365.

[43] L. Zhen, H. Zhengjia, Z. Yanyang, and C. Xuefeng, "Bearing condition monitoring based on shock pulse method and improved redundant lifting scheme," *Mathematics and Computers in Simulation,* vol. 79, no. 3, pp. 318-338, 2008/12/01/ 2008, doi: https://doi.org/10.1016/j.matcom.2007.12.004.

[44] Y. He, M. Hu, K. Feng, and Z. Jiang, "Bearing condition evaluation based on the shock pulse method and principal resonance analysis," *IEEE Transactions on Instrumentation and Measurement,* pp. 1-1, 2021, doi: 10.1109/tim.2021.3050679.

[45] N. Tandon, G. S. Yadava, and K. M. Ramakrishna, "A comparison of some condition monitoring techniques for the detection of defect in induction motor ball bearings," *Mechanical Systems and Signal Processing,* vol. 21, no. 1, pp. 244-256, 2007/01/01/ 2007, doi: https://doi.org/10.1016/j.ymssp.2005.08.005.

[46] M. He and D. He, "Deep Learning Based Approach for Bearing Fault Diagnosis," *IEEE Transactions on Industry Applications,* vol. 53, no. 3, pp. 3057-3065, 2017, doi: 10.1109/tia.2017.2661250.

[47] O. Duque-Perez, C. Del Pozo-Gallego, D. Morinigo-Sotelo, and W. Fontes Godoy, "Condition Monitoring of Bearing Faults Using the Stator Current and Shrinkage Methods," *Energies,* vol. 12, no. 17, p. 3392, 2019. [Online]. Available: https://www.mdpi.com/1996-1073/12/17/3392.

[48] V. Leite *et al.*, "Detection of Localized Bearing Faults in Induction Machines by Spectral Kurtosis and Envelope Analysis of Stator Current," *Ieee Transactions on Industrial Electronics,* vol. 62, no. 3, pp. 1855-1865, Mar 2015, doi: 10.1109/tie.2014.2345330.

[49] I. Y. Önel and M. E. H. Benbouzid, "Induction Motor Bearing Failure Detection and Diagnosis: Park and Concordia Transform Approaches Comparative Study," *IEEE/ASME Transactions on Mechatronics,* vol. 13, no. 2, pp. 257-262, 2008, doi: 10.1109/tmech.2008.918535.

[50] M. E. H. Benbouzid and G. B. Kliman, "What stator current processing-based technique to use for induction motor rotor faults diagnosis?," *IEEE Transactions on Energy Conversion,* vol. 18, no. 2, pp. 238-244, 2003, doi: 10.1109/tec.2003.811741.

[51] L. Frosini, C. Harlisca, and L. Szabo, "Induction Machine Bearing Fault Detection by Means of Statistical Processing of the Stray Flux Measurement," *IEEE Transactions on Industrial Electronics,* vol. 62, no. 3, pp. 1846-1854, 2015, doi: 10.1109/tie.2014.2361115.

[52] A. Romanenko, J. Ahola, A. Muetze, and V. Niskanen, "Study of incipient bearing damage monitoring in variable-speed drive systems," 2014: IEEE, doi: 10.1109/epe.2014.6910992. [Online]. Available: https://dx.doi.org/10.1109/epe.2014.6910992

[53] R. K. Singleton, E. G. Strangas, and S. Aviyente, "The Use of Bearing Currents and Vibrations in Lifetime Estimation of Bearings," *IEEE Transactions on Industrial Informatics,* vol. 13, no. 3, pp. 1301-1309, 2017, doi: 10.1109/tii.2016.2643693.

[54] T. Zika, I. C. Gebeshuber, F. Buschbeck, G. Preisinger, and M. Groschl, "Surface analysis on rolling bearings after exposure to defined electric stress," (in English), *Proc. Inst. Mech. Eng. Part J.-J. Eng. Tribol.,* Article vol. 223, no. J5, pp. 787-797, Aug 2009, doi: 10.1243/13506501jet538.

[55] SKF, "Bearing Damage and Failure Analysis."

[56] E. Wittek, M. Kriese, H. Tischmacher, S. Gattermann, B. Ponick, and G. Poll, "Capacitance of bearings for electric motors at variable mechanical loads," 2012: IEEE, doi: 10.1109/icelmach.2012.6350093. [Online]. Available: https://dx.doi.org/10.1109/icelmach.2012.6350093

[57] V. Niskanen, A. Muetze, and J. Ahola, "Study on Bearing Impedance Properties at Several Hundred Kilohertz for Different Electric Machine Operating Parameters," *IEEE Transactions on Industry Applications,* vol. 50, no. 5, pp. 3438-3447, 2014, doi: 10.1109/tia.2014.2308392.

[58] "IEEE Standard for Transitions, Pulses, and Related Waveforms," doi: 10.1109/ieeestd.2011.6016198.

[59] "CRD200DA09E: High Performance Three Phase Evaluation Unit," ed: Cree, January 2018.

[60] "HT-3291-R-VB," ed: Cree, November 2018.

[61] R. Collin, M. Stephens, and A. Von Jouanne, "Development of SiC-Based Motor Drive Using Typhoon HIL 402 as System-Level Controller," 2020: IEEE, doi: 10.1109/ecce44975.2020.9236201. [Online]. Available: https://dx.doi.org/10.1109/ecce44975.2020.9236201

[62] "Typhoon HIL 402 Brochure," ed: Typhoon HIL.

[63] ABB, "ACS800 Hardware Manual ", ed, 2013.

[64] E. Wittek, M. Kriese, H. Tischmacher, S. Gattermann, B. Ponick, and G. Poll, "Capacitances and lubricant film thicknesses of motor bearings under different operating conditions," in *The XIX International Conference on Electrical Machines - ICEM 2010*, 6-8 Sept. 2010 2010, pp. 1-6, doi: 10.1109/ICELMACH.2010.5608142.

[65] A. v. Jouanne *et al.*, "Development of Inverter Duty Motor Bearings for Si and SiC-Based Variable Frequency Drive Applications Including Advanced 4D Finite Element Modeling," in *2021 IEEE Energy Conversion Congress and Exposition (ECCE)*, 10-14 Oct. 2021 2021, pp. 5154-5161, doi: 10.1109/ECCE47101.2021.9595862.

[66] H. Cen and P. M. Lugt, "Film thickness in a grease lubricated ball bearing," *Tribology International*, vol. 134, pp. 26-35, 2019/06/01/ 2019, doi: https://doi.org/10.1016/j.triboint.2019.01.032.

[67] W. Kaminsky and I.-J. Zorriqueta, "Catalytical and thermal pyrolysis of polyolefins," *Journal of Analytical and Applied Pyrolysis*, vol. 79, pp. 368-374, 05/01 2007, doi: 10.1016/j.jaap.2006.11.005.

[68] N. Muradov, "Emission-free fuel reformers for mobile and portable fuel cell applications," *Journal of Power Sources*, vol. 118, no. 1, pp. 320-324, 2003/05/25/ 2003, doi: https://doi.org/10.1016/S0378-7753(03)00078-8.

[69] N. Zhu, "Common-Mode Voltage Mitigation by Novel Integrated Chokes and Modulation Techniques in Power Converter Systems," PhD, Electrical and Computer Engineering, Ryerson University, Toronto, Ontario, Canada, 2013.

[70] *Shapiro-Wilk and Shapiro-Francia Normality Tests*. (2021). MATLAB Central File Exchange. Accessed: September 10, 2021. [Online]. Available: https://www.mathworks.com/matlabcentral/fileexchange/13964-shapiro-wilk-and-shapiro-francia-normality-tests

[71] *ISO 20816-1: Mechanical vibration — Measurement and evaluation of machine vibration* I. O. f. Standardization, 2016.

[72] T. A. Harris, *Rolling Bearing Analysis*. New York: John Wiley & Sons, Inc. [US] (in English), 2001.

[73] I. New Hampshire Ball Bearings. "Internal Geometry of Ball Bearings." https://www.nhbb.com/knowledge-center/engineering-reference/ball-roller-bearings/internal-geometry-ball-bearings#:~:text=The%20contact%20angle%20is%20the,inner%20and%20outer%20track%20curvatures. (accessed January 20, 2022).